学位論文

Search for proton decay
into a muon and a neutral kaon
in the Super-Kamiokande water Cherenkov detector
（スーパーカミオカンデ水チェレンコフ検出器によるミューオンと中性K中間子への陽子崩壊探索）

2023年3月

松本　遼

Abstract

A grand unified theory (GUT) is an extension of the standard model (SM) of particle physics that unifies leptons, baryons and gauge bosons. The GUT is considered a strong candidate for new physics beyond the SM as it provides an explanation to some fundamental questions in our universe with a natural extension of the SM although it has not been confirmed by any experiments. For this reason, verification of the GUT is one of the most important subjects in particle physics today. Whereas protons are considered stable particles in the SM, GUT models predict proton decay through interactions in which the baryon number is not conserved. Therefore, the measurement of proton decay is direct evidence of the GUT.

In this thesis, a search for proton decay via $p \rightarrow \mu^+ + K^0$ is described with 0.37 Mton·years of data collected between 1996 and 2018 from the Super-Kamiokande detector. The Super-Kamiokande detector is a large water Cherenkov detector located 1000 m underground in the Kamioka mine in Hida City, Gifu Prefecture. It contains 50 kton of ultrapure water in a cylindrical tank with 39.3 m in diameter and 41.4 m in height. The Cherenkov light emitted from charged particles in the water is detected by approximately 11000 optical sensors (photomultiplier tubes) installed on the wall. The analysis method was updated for the data taken between 2008 and 2018 (referred to as SK-IV) with upgraded electronics that allows for the detection of neutron capture on hydrogen. In addition to neutron tagging, the analysis was performed with an improved event reconstruction algorithm, and event selection criteria optimized to select proton decay signals against the atmospheric neutrino background events. The efficiency of the proton decay signals and the expected background events were estimated based on the simulation. As K^0 exists as superpositions of K^0_S and K^0_L, the selection criteria were defined separately for K^0_S and K^0_L channels.

Observations of atmospheric neutrinos are themselves important physics targets of the Super-Kamiokande detector to measure the transition of neutrino flavor (neutrino oscillation) and reveal their properties including as yet unknown neutrino mass ordering and CP phase. This thesis also describes a new neutrino event classification method using machine learning. The performance of the identification of neutrino flavor was improved with the machine learning technique by accounting for the correlations of the observable kinematic parameters.

As a result of the proton decay search, no significant event excess has been observed over the

expected background rates. According to the observation, the lower limit of the lifetime of proton decay to a muon and a neutral kaon was set as 4.5×10^{33} years from the SK-IV data. Furthermore, this result was statistically combined with the result of the previous analysis [1] using the data during 1996 and 2008, and the lower limit was set as 3.6×10^{33} years. This is the most stringent limit in the world, updating the lifetime limit from the previous analysis more than factor two. This study achieved giving additional constraints to the GUT models with the lower limit on the lifetime.

Contents

Chapter 1

Physics background

1.1 Standard model

The standard model (SM) is the most fundamental framework of particle physics (Table 1.1). In the SM, matter consists of Dirac particles and they are classified into two categories, that are quarks and leptons. These quarks and leptons interact with each other via gauge particles. There are three types of gauge particles: gluon, photon and weak boson which mediate interactions corresponding to the fundamental forces in nature, i.e. strong, electromagnetic and weak forces, respectively. These particles have a pair of antiparticles with opposite electric charges and equal masses. In addition to these particles, there is a Higgs boson, whose vacuum expectation spontaneously breaks the symmetry and gives mass to particles.

Table 1.1: Elementary particles in the SM.

	1st generation	2nd generation	3rd generation
Quarks	up (u), down (d)	charm (c), strange (s)	top (t), bottom (b)
Leptons	electron (e), e-neutrino (ν_e)	muon (μ), μ-neutrino (ν_μ)	tauon (τ), τ-neutrino (ν_τ)
Gauge fields	photon (γ), weak-boson $(Z^0, W^\pm)$, gluon (g)		
Scalar fields	Higgs (H^0)		

Quarks and leptons have pairs of different charges and form doublets for weak interactions. The examples are up quark u (charge $+2/3$ in the unit of elementary charge) and down quark d (charge $-1/3$) for quarks, and electron e (charge -1) and electron neutrino ν_e (charge 0) for leptons. They can change into each other forming doublets via weak bosons. Figure 1.1 shows examples of the charge-exchange process via weak interactions. The states of quarks and leptons can be divided by the helicity, which is defined as the projection of the spin onto the direction of momentum, into those in which the spin direction is the same as the direction of momentum (right-handed) or opposite (left-handed) as shown in Figure 1.2. The weak interaction works only on the left-handed component of particles.

Quarks have three degrees of freedom called colors (red, blue and green) for strong interactions.

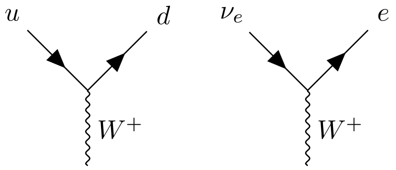

Figure 1.1: Diagram of the charge-exchange process via weak interactions.

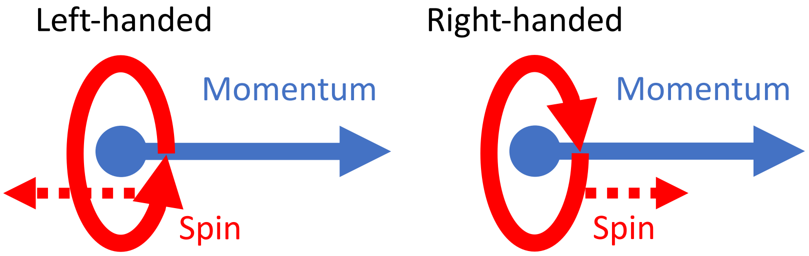

Figure 1.2: Schematic diagram of helicity. When spin, the angular momentum intrinsic to the particle, and momentum are in the same (opposite) direction, it is right-handed (left-handed).

A color becomes stable with its anti-color (e.g. red and antired), and an antiparticle has an anticolor. Also, a set of two colors becomes an anticolor of a remaining color, so the combinations of red-blue-green and red-antired are stable combinations for example. Therefore, unlike leptons, quarks cannot be observed as a single state and appear in nature as composite particles, called hadrons, in which quarks are bound by strong interactions. Among the hadrons, those composed of three quarks of antiquarks are called baryons, and those composed of one quark and one antiquark are called mesons (Figure 1.3). For example, a proton and neutron consist of three quarks as uud and udd, respectively. A pion and kaon are examples of mesons which are composed of u, d, s quarks and their antiquarks as π^+: $u\bar{d}$, π^0: $u\bar{u}$ or $d\bar{d}$, π^-: $d\bar{u}$, K^+: $u\bar{s}$, K^0: $d\bar{s}$ or K^0: $s\bar{d}$, and K^-: $s\bar{u}$. Each quark (antiquark) has a conserved additive quantum number $1/3$ ($-1/3$) called baryon number B. Proton is the lightest baryon with $B = 1$ and therefore stable in the SM due to the baryon number conservation.

Furthermore, it is known that there is a hierarchy (called generation) of quarks and leptons: three types of particles with equal electric charge but different masses. In total, six types (called flavors) of quarks and leptons exist.

All particles in the SM were confirmed by the experiments, among those Higgs boson was discovered in 2012 using the Large Hadron Collider (LHC) accelerator of CERN. The SM has been tested up to the TeV energy scale by various experiments and the observed data are precisely reproduced by the prediction from the SM. On the other hand, various fundamental problems remain in the theory such as the reason why positrons (antiparticles of electrons) and protons have exactly equal charges and the origin of the matter in the universe.

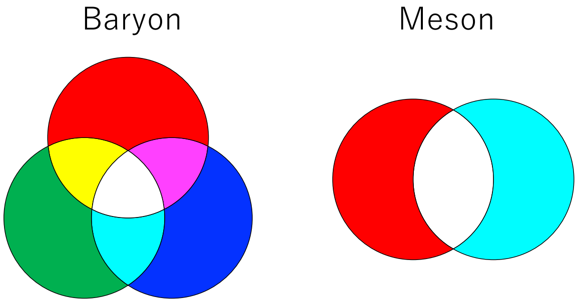

Figure 1.3: Schematic diagram of color combination for baryons (left) and mesons (right). Baryons consist of red, green and blue, and mesons consist of red and antired (cyan). Other combinations, i.e. blue and antiblue (yellow), and green and antigreen (magenta), are also possible for mesons. Colorless combinations are stable.

1.2 Unification of gauge interactions

The SM contains a gauge symmetry of SU(3)×SU(2)×U(1), and among the gauge interactions the electromagnetic and weak interactions are unified as electroweak interactions SU(2)×U(1) at high-energy regions. Since the symmetry of the left-handed and right-handed is broken, the left-handed fermions and right-handed fermion form SU(2) doublet and U(1) singlet, respectively.

$$\begin{bmatrix} \nu_{eL} \\ e_L \end{bmatrix}, \quad e_R \tag{1.1}$$

The electroweak interaction has SU(2)×U(1) gauge symmetry, which is spontaneously broken to $\mathrm{U}(1)_{\mathrm{EM}}$ symmetry of the electromagnetic interaction due to the Higgs mechanism with a vacuum expectation value of the Higgs field. On the other hand, the strong interaction is described by SU(3) group and forms triplets for quarks with different colors.

The coupling constants between the gauge fields and fermions show different dependencies on the energy scale. Electromagnetic interactions tend to be more strongly coupled at higher energies, whereas strong interactions tend to have weaker coupling constants at higher energies with a small distance and large momentum transfer. Figure 1.4 shows the energy dependence of the U(1), SU(2) and SU(3) coupling constants. These coupling constants approach the same value around 10^{14-16} GeV. It indicates a unified model of these gauge interactions beyond the SM at high energies.

1.3 Grand unified theories

A grand unified theory (GUT) is an extension of the SM that unifies leptons, baryons and gauge bosons [3]. In the GUT, strong, electromagnetic and weak forces are unified at high energy, typically above 10^{14} GeV, which is much higher than the energy scale achieved by the current particle

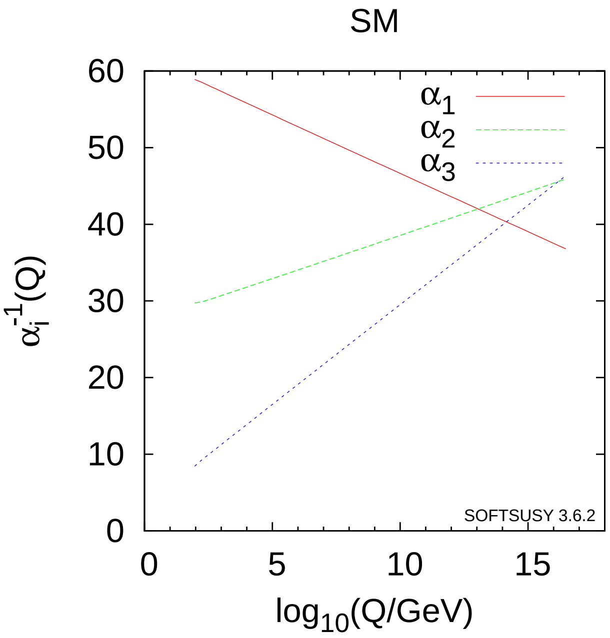

Figure 1.4: Running couplings of U(1) (red, α_1), SU(2) (green, α_2) and SU(3) (blue, α_3) for the energy scale Q in the SM using two-loop RG evolution [2].

accelerators. The three forces are described by a single coupling constant in the GUT. Various GUT models based on different gauge groups have been theoretically proposed, while there is no evidence for the GUT given by the experiments so far. and their verification is one of the most important subjects in particle physics today.

In the SM, quarks and leptons are not unified and there are no interactions that convert into each other, unlike electrons and neutrinos which are unified and transformed into each other through the exchange of weak bosons. Baryon number is conserved as a consequence of the absence of such interactions which convert quarks into leptons. Therefore, protons do not decay in the SM as they are the lightest baryon. In contrast, many of the GUTs predict proton decay into particles including leptons through interactions in which the baryon number is not conserved. The dominant proton decay channel depends on the assumptions of the framework and parameters of the theoretical models.

The existence of baryon number violation is one of the Sakharov conditions for the development of the universe after the Big Bang to break the symmetry between matter and antimatter and to establish a matter-dominated universe [4]:

1. Baryon number violation
2. C and CP symmetry breaking
3. Interactions out of thermal equilibrium

The GUTs accommodate interactions to violate the baryon number in the theory of particle physics which satisfies one of the conditions for explaining the origin of matter.

1.3.1 Minimal SU(5)

The minimal SU(5) model [5] is the simplest model of the GUT, which contains SU(3), SU(2) and U(1) gauge groups to unify the strong, weak and electromagnetic interactions.

The particles correspond to the representation of the SU(5) group. The gauge fields are assigned to the adjoint representation (24 components), and the upper left 3×3 of the 5×5 matrix corresponds to the SU(3) gauge and the lower right 2×2 corresponds to the SU(2) gauge.

$$\begin{bmatrix} g_{11} - \frac{2B}{\sqrt{30}} & g_{12} & g_{13} & \bar{X}^1 & \bar{Y}^1 \\ g_{21} & g_{22} - \frac{2B}{\sqrt{30}} & g_{23} & \bar{X}^2 & \bar{Y}^2 \\ g_{31} & g_{32} & g_{33} - \frac{2B}{\sqrt{30}} & \bar{X}^3 & \bar{Y}^3 \\ X^1 & X^2 & X^3 & \frac{W^3}{\sqrt{2}} + \frac{3B}{\sqrt{30}} & W^+ \\ Y^1 & Y^2 & Y^3 & W^- & -\frac{W^3}{\sqrt{2}} + \frac{3B}{\sqrt{30}} \end{bmatrix} \tag{1.2}$$

where g are gluons, and B and W are gauge bosons in the electroweak theory. The X and Y bosons are not included in the SM and have the charge of 4/3 and 1/3, respectively. It can be explained that X and Y bosons have not been observed yet due to the extremely heavy mass compared to the other gauge bosons. To avoid introducing new particles, quarks and leptons are assigned to basic and antisymmetric representation. The sum of the number of components ($15 = 5$ (basic) + 10 (antisymmetric)) is consistent with the number of fermions in the SM ($15 = 2$ (u, d) × 3 (color) × 2 (left, right) + $2(e_L^-, e_R^-)$ + $1(\nu_L)$, where L and R represent the left-handed and right-handed fermions). The 5^* representation (complex conjugate representation of 5 representation) is

$$\begin{bmatrix} d^c_{rR} \\ d^c_{gR} \\ d^c_{bR} \\ -e_L \\ \nu_L \end{bmatrix} \tag{1.3}$$

to be the total charge is zero since SU(5) is traceless. Here r, g and b represent the colors, and c represents the charge conjugation of particles (it means antiparticles). Since the charge of the basic representation is $[-1/3, -1/3, -1/3, 1, 0]$, the charge for antisymmetric representation should be assigned as

$$\begin{bmatrix} -2/3 & -2/3 & -2/3 & 2/3 & -1/3 \\ -2/3 & -2/3 & -2/3 & 2/3 & -1/3 \\ -2/3 & -2/3 & -2/3 & 2/3 & -1/3 \\ 2/3 & 2/3 & 2/3 & 2 & 1 \\ -1/3 & -1/3 & -1/3 & 1 & 0 \end{bmatrix}. \tag{1.4}$$

The remaining fermions are assigned to these components with attention to the colors:

$$\begin{bmatrix} 0 & u^c_{bR} & -u^c_{gR} & u_{rL} & d_{rL} \\ & 0 & u^c_{rR} & u_{gL} & d_{gL} \\ & & 0 & u_{bL} & d_{bL} \\ & & & 0 & e^c_R \\ & & & & 0 \end{bmatrix}, \tag{1.5}$$

where the opposite components are omitted since it is an antisymmetric matrix. Although the mass of X and Y bosons are much higher than the mass of protons, the exchange of these bosons occurs in protons with an extremely small probability. This model predicts proton decay with the dominant mode as $p \to e^+ + \pi^0$ via the exchange of X boson (Figure 1.5) with an extremely long lifetime.

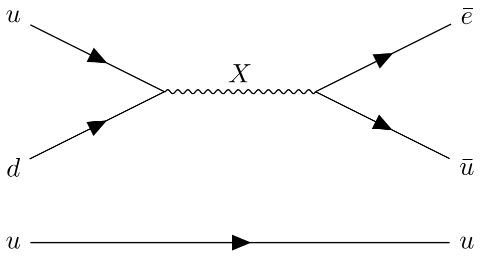

Figure 1.5: Feynman diagram of proton decay $p \to e^+ + \pi^0$ via the exchange of X boson. uud quarks in the left-hand side form a proton and $\bar{u}u$ in the right-hand side form a neutral pion (π^0).

The expected lifetime of protons is approximately 10^{30} years in this model assuming the mass of X and Y are an order of $10^{14}\,\mathrm{GeV}/c^2$ from the unification of the coupling constants (Section 1.2). Although this lifetime is longer than the time scale of the universe, which started about 10^8 years ago from the Big Bang, it is still possible to search for the proton decay and test the GUT by observing a large number of protons in the detector. For example, if the proton lifetime is 10^{30} years, 10 protons out of 10^{31} protons decay on average in one year. This minimal SU(5) model has already been rejected by the Kamiokande, IMB-3 and Super-Kamiokande experiments in the searches for $p \to e^+ + \pi^0$ [6][7][8].

1.3.2 Other GUT models

Supersymmetric SU(5) is an extension of the simplest SU(5) model. Supersymmetry (SUSY) is a framework beyond the SM based on symmetry between a boson and a fermion, which requires the existence of partner fermions (bosons) in the bosons (fermions) appearing in the theory. The theory is motivated by resolving fine-tuning of parameters to explain the Higgs mass that are experimentally determined in the SM. The contributions from the SUSY particles make the energy scale of the GUT higher and extend the lifetime of the simple decay via X bosons. As a consequence, the SU(5) gauge model still survives depending on the parameters in SUSY, such as the coupling of the SUSY particles with the SM particles and the flavor mixing of the SUSY bosons. Minimal

SUSY SU(5) model [9] predicts proton decay with the dominant mode as $p \to \bar{\nu} + K^+$ and the lifetime $\leq 1.1 \times 10^{35}$ years when the SUSY scalar masses are required to be $\leq 30\,\mathrm{TeV}$, so that they are within reach of collider experiments.

In addition to SU(5), SO(10) is also a group including SU(3)×SU(2)×U(1). Before breaking into SU(3)×SU(2)×U(1) of the SM, SO(10) breaks into intermediate symmetries such as SU(5)×U(1) and SU(4)×SU(2)×SU(2). In the former case, the right-handed lepton and quark assignments are flipped compared to the standard SU(5) and it is called the flipped SU(5) model [10]. As an example of the latter case, minimal non-supersymmetric SO(10) model [11] predicts the proton lifetime as $\mathcal{O}(10^{35})$ years and the dominant decay channels are $p \to e^+ + \pi^0$ (branching ratio BR=47%), $p \to \mu^+ + \pi^0$ (branching ratio BR=1.0%), $p \to \bar{\nu} + \pi^+$ (branching ratio BR=48%) and $p \to \mu^+ + K^0$ (branching ratio BR=3.6%).

Supersymmetric GUT models often predict $p \to \bar{\nu} + K^+$ and $p \to \mu^+ + K^0$ as the dominant channel due to the contribution of the color triplet Higgs which are predicted in typical SUSY models as an extension of the Higgs mechanism to introduce symmetry breaking at different energy scales [12]. Some models [12] predict the partial lifetime of the $p \to \mu^+ + K^0$ channel can be comparable to $p \to \bar{\nu} + K^+$ or shorter and in a range that slightly exceeds the current experimental limit of 1.6×10^{33} years [1]. These models have a prediction of the proton lifetime as $\mathcal{O}(10^{34})$ years and the fraction is accounted for by $p \to \mu^+ + K^0$ channel. $p \to e^+ + \pi^0$, $p \to \mu^+ + \pi^0$, $p \to \bar{\nu} + K^+$ and $p \to e^+ + K^0$ appear as the other dominant decay channels.

Also, there is a R-symmetric flipped SU(5) model [13] which predicts protons do not decay via $p \to \bar{\nu} + K^+$ because the color triplet Higgs does not couple to the left-handed neutrino, and $p \to \mu^+ + K^0$ becomes the dominant decay channel. This model predicts the proton lifetime as $\tau(p \to e^+ + \pi^0) \sim 10^{35}$ years, $\tau(p \to \mu^+ + \pi^0) \sim 10^{35}$ years, $\tau(p \to e^+ + K^0) \sim 10^{37}$ years and $\tau(p \to \mu^+ + K^0) \sim 10^{34}$ years if the color triplet Higgs mass is $\sim 10^{12}\,\mathrm{GeV}$ and $\tan\beta = 3$, where β is a Higgs vacuum expectation ratio.

These models generally prefer shorter lifetimes which are accessible by the search with the Super-Kamiokande detector, or the next-generation projects such as Hyper-Kamiokande. Several decay channels of proton decay have been searched in Super-Kamiokande as shown in Table 1.2.

1.4 Proton decay via $p \to \mu^+ + K^0$

The study described in this thesis focuses on a search for the $p \to \mu^+ + K^0$ decay mode in the Super-Kamiokande (SK) detector. This two-body decay generates a muon and a neutral kaon with monochromatic momentum of $326.5\,\mathrm{MeV}/c$. The K^0 is a composite state of K^0_S and K^0_L. K^0_S decays into $\pi^+\pi^-$ (69.2%) and $2\pi^0$ (30.7%) with a lifetime of 90 ps while K^0_L decays into $\pi^\pm e^\mp \nu$ (40.6%), $\pi^\pm \mu^\mp \nu$ (27.0%), $3\pi^0$ (19.5%) and $\pi^+\pi^-\pi^0$ (12.5%) with the lifetime of 51 ns. Proton decay searches

Table 1.2: List of proton decay channels which have been searched in Super-Kamiokande.

Channel	Lifetime limit (years)	Reference
$p \to e^+ + \pi^0$	2.4×10^{34}	[8]
$p \to \mu^+ + \pi^0$	1.6×10^{34}	[8]
$p \to \bar{\nu} + K^+$	8.2×10^{33}	[14]
$p \to e^+ + e^+ + e^-$	3.4×10^{34}	[15]
$p \to \mu^+ + e^+ + e^-$	2.3×10^{34}	[15]
$p \to \mu^- + e^+ + e^+$	1.9×10^{34}	[15]
$p \to e^+ + \mu^+ + \mu^-$	9.2×10^{33}	[15]
$p \to e^- + \mu^+ + \mu^+$	1.1×10^{34}	[15]
$p \to \mu^+ + \mu^+ + \mu^-$	1.0×10^{34}	[15]
$p \to \bar{\nu} + \pi^+$	3.9×10^{32}	[16]
$p \to \mu^+ + K^0$	1.6×10^{33}	[1]
$p \to e^+ + \eta$	1.0×10^{34}	[17]
$p \to \mu^+ + \eta$	4.7×10^{33}	[17]
$p \to e^+ + \rho^0$	7.2×10^{32}	[17]
$p \to \mu^+ + \rho^0$	5.7×10^{32}	[17]
$p \to e^+ + \omega$	1.6×10^{33}	[17]
$p \to \mu^+ + \omega$	2.8×10^{33}	[17]
$p \to e^+ + X$	7.9×10^{32}	[18]
$p \to \mu^+ + X$	4.1×10^{32}	[18]
$p \to e^+ + \nu + \nu$	1.7×10^{32}	[19]
$p \to \mu^+ + \nu + \nu$	2.2×10^{32}	[19]

for the $p \to \mu^+ + K^0$ mode have been performed in SK using the data collected in the SK-I, SK-II, and SK-III phases (0.17 Mton·years of exposure [1] from 1996 to 2008) and no significant signal of $p \to \mu^+ + K^0$ was observed [20][1]. A lower limit on the partial proton lifetime $p \to \mu^+ + K^0$ of 1.6×10^{33} years was set at the 90% confidence level (C.L.). In this thesis, the search was extended with the data collected in the SK-IV phase from 2008 to 2018 which corresponds to 0.20 Mton·years of exposure with the improved analysis method.

---

[1] In proton decay search, megaton·years, a product of the detector mass and observed time, is used as the unit of the observed quantity because the sensitivity depends on the number of observed protons and observed time.

Chapter 2

Motivation

As described in Chapter 1, the grand unified theory (GUT) is a framework beyond the standard model (SM) of particle physics. The GUT provides explanations for some of the fundamental questions as yet unresolved in the SM and therefore the verification of the GUT is one of the most important subjects in particle physics. The energy scale of the GUT is predicted as the region around 10^{14-16} GeV, while this energy scale is too high to test by the current accelerators. On the other hand, the GUT predicts proton decay which is forbidden in the SM due to the baryon number conservation. Therefore, observation of proton decay provides direct evidence for the GUT although it has not yet been observed. The Super-Kamiokande (SK) experiment has been exploring various proton decay channels. The SK experiment limits the lifetime of the proton decay via $p \to e^+ + \pi^0$ as 2.4×10^{34} years [8] which is predicted as a major decay channel in the nominal SU(5) model. The proton decay via $p \to \bar{\nu} + K^+$ is also predicted as a major decay channel in SUSY GUT models, and the lifetime of this channel is limited by SK as 8.2×10^{33} years [14]. In this thesis, the proton decay via $p \to \mu^+ + K^0$ has been searched for the data collected from the SK detector. While some SUSY GUT models predict $p \to \mu^+ + K^0$ as another major channel, the search of this channel has not been updated in SK since 2012 although approximately twice of the data has been accumulated with respect to the previous publication [1]. Furthermore, the analysis method can be improved with a new reconstruction algorithm, neutron tagging (Chapter 7) and optimized selection criteria (Chapter 8). These improvements make it possible to expand the lifetime limit by a factor more than two from the previous result of 1.6×10^{33} years on the lifetime of $p \to \mu^+ + K^0$ [1]. For these reasons, there is a possibility to make a discovery of proton decay in this channel and this is the motivation of this thesis. Since this decay channel has K^0, the simulation of the kaon interaction is important to search the events. The simulation was updated for this study by referring to the experimental data of K-N scattering (Chapter 4 and 10). Combining the results in the previous search [1], proton decay via $p \to \mu^+ + K^0$ have been searched with the largest exposure in SK (Chapter 9). These studies are reported in [21].

In addition to the proton decay search, this thesis describes a new classification method for atmospheric neutrino interactions using machine learning (Section 5.4). Atmospheric neutrinos are the dominant background in the proton decay search. In addition, the study of neutrino oscillations is also being conducted using the data from atmospheric neutrino observations. The new method improves the classification and could be used for future studies of the neutrino oscillation parameters such as the CP phase and mass ordering. These studies are reported in [22].

Chapter 3

Super-Kamiokande detector

3.1 Overview

Super-Kamiokande (SK) is a large water Cherenkov detector that contains 50 kton of ultrapure water in a cylindrical tank (Figure 3.1). It is designed to search for proton decay and reveal the properties of neutrinos. The Super-Kamiokande detector is located 1000 m underground (2700 m.w.e.) in Gifu Prefecture, Japan. The detector is located underground to reduce the cosmic-ray muons to 1/100000 of the ground surface by the rock overburden.

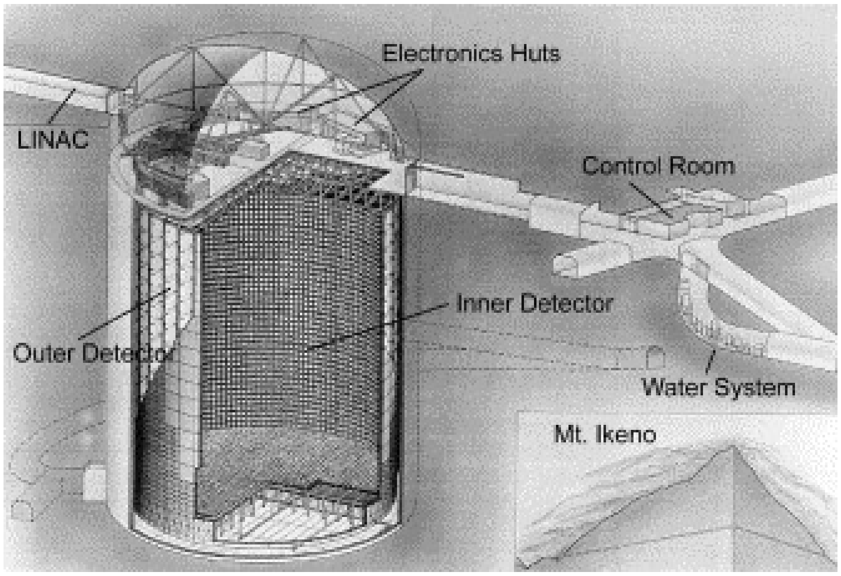

Figure 3.1: Schematic view of the SK detector [23].

The detector has two regions, the inner detector and the outer detector surrounding it, and both regions have photosensors. The inner region works as a target of proton decay search and neutrino interactions while the outer detector is necessary to reject the backgrounds. When protons in the water decay or neutrinos enter the SK detector and interact with electrons or nuclei in the water tank, charged particles are produced. As explained in Section 3.3, Cherenkov light is emitted when charged particles travel in water with a velocity larger than the propagation of light. These Cherenkov photons are detected by photomultiplier tubes (PMTs), which are photo sensors installed on the wall of the water tank, and the particles are observed if the Cherenkov ring is recognized from the PMT signals. Figure 3.2 shows examples of Cherenkov rings by an electron and muon. Electrons and gammas generate showering rings called *e*-like rings because they produce electromagnetic showers and generate diffuse Cherenkov rings. In contrast, muons and charged pions do not produce showers and generate Cherenkov rings with clear edges called μ-like rings. Using the event reconstruction algorithm, we estimate basic event properties such as vertex (generated position), direction, particle type and momentum based on the PMT hit information.

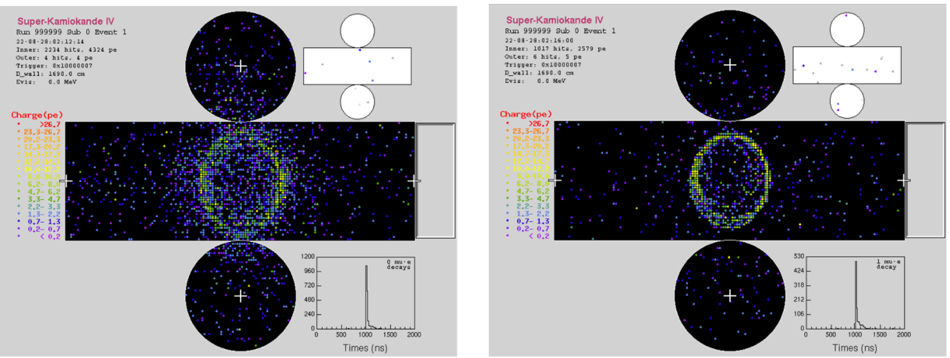

Figure 3.2: Examples of the *e*-like ring by an electron (left) and μ-like ring by a muon (right) in the simulation. Points correspond to the PMTs on the inside wall, and the colors correspond to the observed electric charge of PMTs.

The data used in this analysis are divided into four periods as shown in Table 3.1 by the configuration of the detector. The first period has started as SK-I in 1996 with 11146 PMTs. During maintenance after SK-I in 2001, one of the PMTs ruptured while being refilled with water, which triggered a chain reaction of shock waves and destroyed more than half of the PMTs. The SK-II period has started in 2002 with half of the PMTs for SK-I. The locations of the remaining PMTs are arranged to be uniform in the detector. Since SK-II, all PMTs are protected by cases to prevent the chain reactions of PMT destruction. After the production of PMTs, SK-III has started in 2006 with almost the same number of PMTs as SK-I. After the upgrade of the electronics from ATM to QBEE [24], SK-IV period has started. By the upgrade of the electronics, neutron tagging was realized even with pure water, as described in Section 7.5. The details of QBEE will be explained in Section 3.6. After 2018 (the end of SK-IV), the SK detector was further upgraded with gadolinium loading in water to enhance the detector. In this study, data collected in SK-IV (3244.39 live days) were newly analyzed and the result was combined with the previous result using SK-I to SK-III (2805.9 live days in total) [1]. The details of the SK detector are described below.

Table 3.1: Detector configuration for each period.

Phase	Period	Inner PMTs	Outer PMTs	PMT cover	Electronics
SK-I	1996–2001	11146	1885	no	ATM
SK-II	2002–2005	5182	1885	no	ATM
SK-III	2006–2008	11129	1885	yes	ATM
SK-IV	2008–2018	11129	1885	yes	QBEE

3.2 Detector structure

The detector is a cylindrical water tank with a 39.4 m diameter and 41.4 m height filled with 50 kton of ultra-pure water. The water tank is divided into two concentric volumes that are optically separated (Figure 3.3). The inner detector (ID) is a cylindrical volume with a 33.8 m diameter and 36.2 m height. It contains 32 kton of water. There are 11129 inward-facing PMTs with 50 cm diameter on the wall to detect the Cherenkov light from charged particles. The ID is surrounded by a 2 m thickness layer called the outer detector (OD). The 2 m thick layer of water attenuates γ and neutron radiation from the surrounding rock and suppresses the background contamination. The OD is composed of 1885 outward-facing PMTs with 20 cm diameter. To increase the light collection efficiency, the walls of the OD are covered with a reflective sheet made of a material called Tyvek and wavelength shifting plates which convert ultraviolet light to the wavelength in the effective sensitivity region of the PMTs (Figure 3.4). The PMTs in the OD are mainly used to identify incoming cosmic ray muons and particles exiting the ID. For example, if charged particles are generated in the ID due to proton decay or neutrino reactions and lose all kinetic energy inside

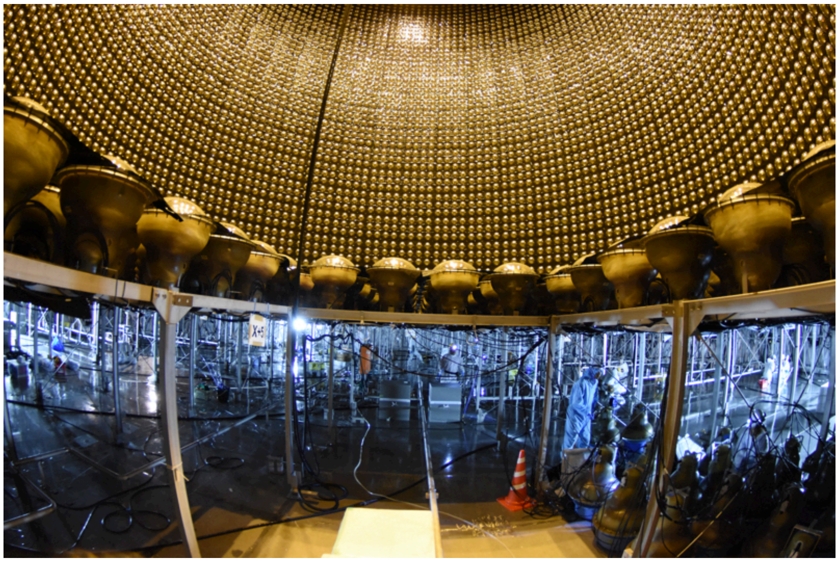

Figure 3.3: A photo from the bottom during the tank renovation in 2018 [25]. The upper part of the tank is the inner region and the lower part is the outer region, bordered by the center of the photo.

Figure 3.4: A photo from the bottom of the outer region. The PMTs with 20 cm diameter are mounted with wavelength shifting plates on the wall on the side of the ID, and the OD is surrounded by a white Tyvek sheet [25].

it, Cherenkov light is emitted only in the ID and there is no response in the OD. In contrast, when cosmic ray muons enter the SK detector, Cherenkov light is detected in both the ID and OD. Therefore, cosmic ray muons can be identified by observing the reaction in the OD. As explained in Section 3.3, energy deposit is measured from the amount of the observed Cherenkov light in the ID. Since the main purpose of the OD is not to measure the energy deposit but to identify particles penetrating the OD, only the minimum necessary PMTs are installed. A dead zone exists with 55 cm thickness between the ID and OD, where the frame supporting the PMT, signal cables, and high-voltage cables are stored. The wall on the ID side is covered with a black sheet made of polyethylene terephthalate to suppress reflection to clarify the Cherenkov ring and prevent light from passing between the ID and OD (Figure 3.5).

3.3 Cherenkov light

Cherenkov light is emitted by charged particles moving faster than light in a medium. The Cherenkov light spreads in a conical shape along the trajectory of the charged particle as shown in Figure 3.6. The angle θ between the charged particle and the cone is expressed using the ratio β of the charged particle velocity v to the light velocity c in a vacuum as

$$\cos\theta = \frac{1}{n\beta}, \tag{3.1}$$

where n is the refractive index of the medium. Since the refractive index in pure water is about 1.34, a particle moving with a speed close to light ($\beta \simeq 1$) in water emits Cherenkov light in the direction of about 42 degrees. Since the velocity of a charged particle must be greater than the speed of light in water to emit Cherenkov light, there is a threshold for the momentum of a particle

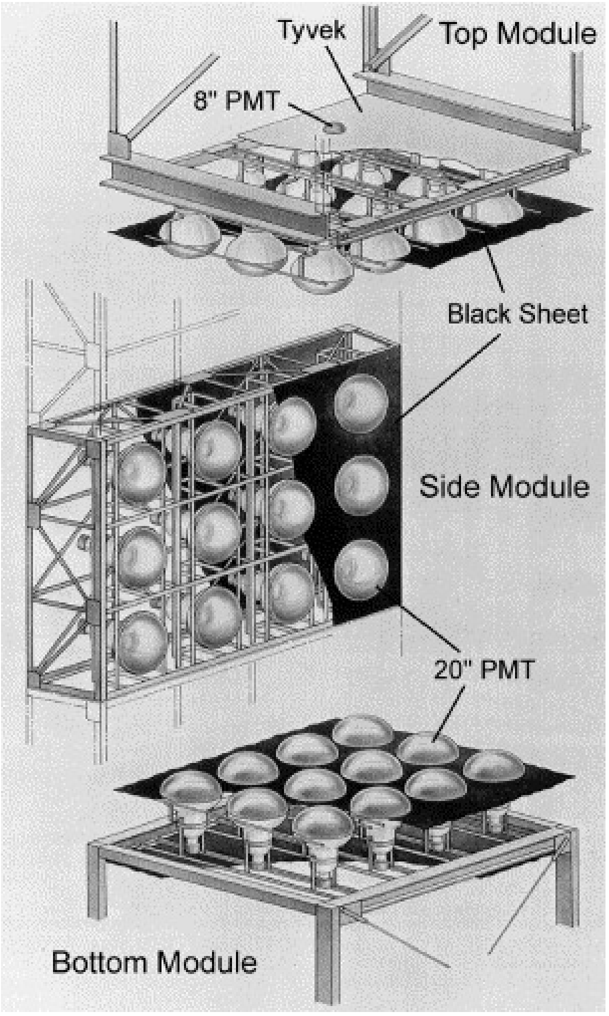

Figure 3.5: The frame supporting the PMT [23].

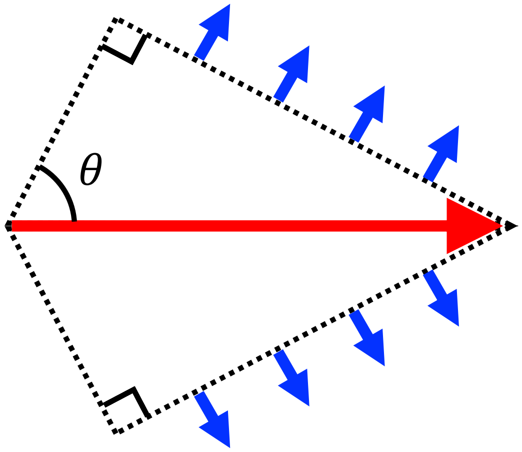

Figure 3.6: Diagram of Cherenkov light emission (blue arrow) from a charged particle (red arrow).

emitting Cherenkov light, as expressed in

$$p \geq \frac{1}{\sqrt{1 - 1/n^2}} mc/n. \tag{3.2}$$

The threshold of Cherenkov light emission depends on the mass m of a charged particle (Table 3.2).

Table 3.2: Momentum thresholds to emit Cherenkov light.

Particle	Mass (MeV/c^2)	Momentum threshold (MeV/c)
Electron	0.511	0.57
Muon	105.6	118
Pion	140	156
Kaon	494	554
Proton	938	1051

The number of emitted photons N per wavelength λ per unit travel distance x of a charged particle is described as follows.

$$\frac{d^2N}{dxd\lambda} = \frac{2\pi\alpha}{\lambda^2}\left(1 - \frac{1}{n^2\beta^2}\right), \tag{3.3}$$

where α is the fine structure constant. This equation shows that Cherenkov light in pure water typically peaks in 300–600 nm and emits about 340 photons per 1 cm particle trajectory. The energy of the particle can be estimated by the number of observed photons once the particle type is identified. If the energy is relatively low and β is sufficiently smaller than 1, the energy can also be obtained from θ given by the Cherenkov radiation angle as Equation 3.1. Therefore, the accuracy of the measurement of the energy is improved by the calibration of the observed number of photons and the opening angle of the Cherenkov ring.

3.4 Photomultiplier tube

A photomultiplier tube (PMT) is a photo sensor that detects signals by amplifying electrons (photoelectrons) emitted by the photoelectric effect. Incident photons are converted to signals by the following steps (Figure 3.7):

1. A photoelectron is emitted from the photocathode by the photoelectric effect.
2. A photoelectron is accelerated by the electric field and collides with the first dynode.
3. Secondary electrons produced by the collision are accelerated by the electric field and collide with the second dynode, producing further electrons.
4. Electrons are multiplied by repeated collisions at the dynodes and extracted from the anode as an electric current.

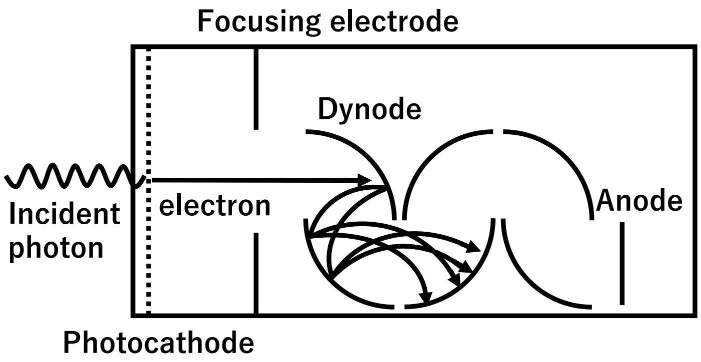

Figure 3.7: Diagram of γ detection by PMT.

Since the amount of electric charge obtained by integrating the output current is proportional to the number of photoelectrons, the incident light intensity can be obtained by conversion from the PMT signal with a relation determined by the calibration. Since the amount of charge generated from a single photoelectron is not always constant but statistically varies, the number of photoelectrons estimated from the amount of charge is not an integer but a real number. Figure 3.8 shows a pulse height distribution for single photoelectron signals.

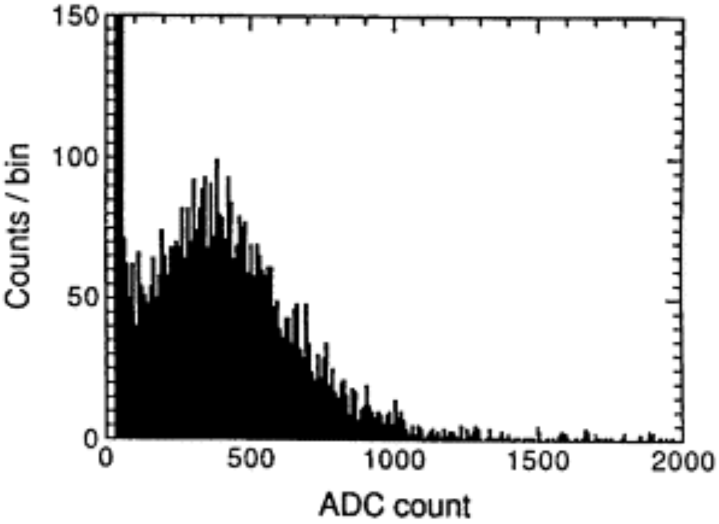

Figure 3.8: Pulse height distribution by single photoelectron electric signals [28].

Super-Kamiokande detects Cherenkov light by PMTs on the wall (Figure 3.9). Large PMTs with a photocathode diameter of 50 cm (20 inches) are installed in the ID (Figure 3.10), which was developed by Hamamatsu Photonics by a cooperation with the Kamiokande collaborators [27][28]. The characteristics of this PMT are summarized in Table 3.3. The photocathode area is covered by Bialkali (Sc-K-Cs) which has high spectral sensitivity for Cherenkov light and low thermionic

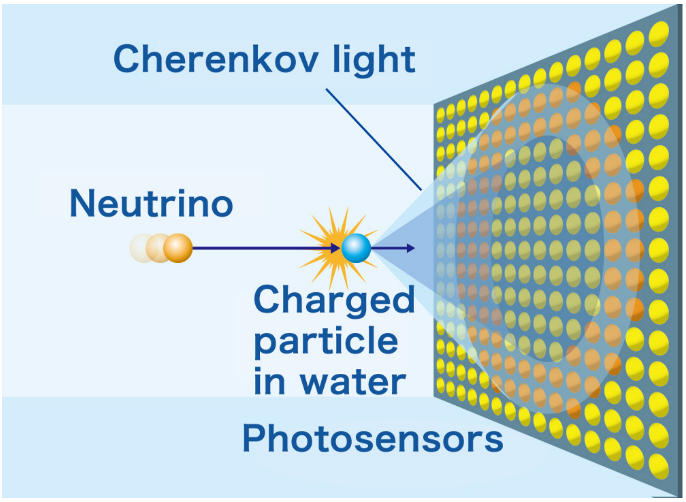

Figure 3.9: Schematic view of Cherenkov light detection [26].

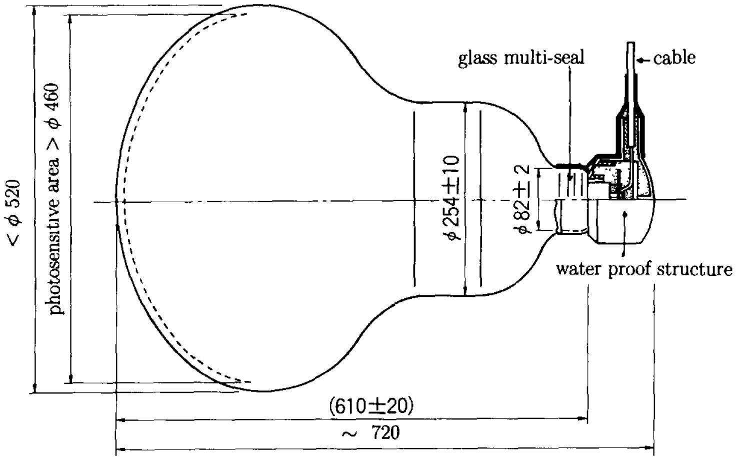

Figure 3.10: Schematic view of the 20-inch PMT [28].

Table 3.3: Characteristics of the 20-inch PMT

Photocathode area	50 cm in diameter
Photocathode material	Bialkali (Sb-K-Cs)
Quantum efficiency	22% at λ =390 nm
Dynode	Venetian blind type, 11 stages
Gain	10^7 at ~ 2000 V
Dark current	200 nA at 10^7 gain
Dart noise rate	3 kHz at 10^7 gain
Transit time	90 ns at 10^7 gain
Transit time spread	2.2 ns (1σ)
Weight	13 kg
Pressure tolerance	6 kg/cm^2

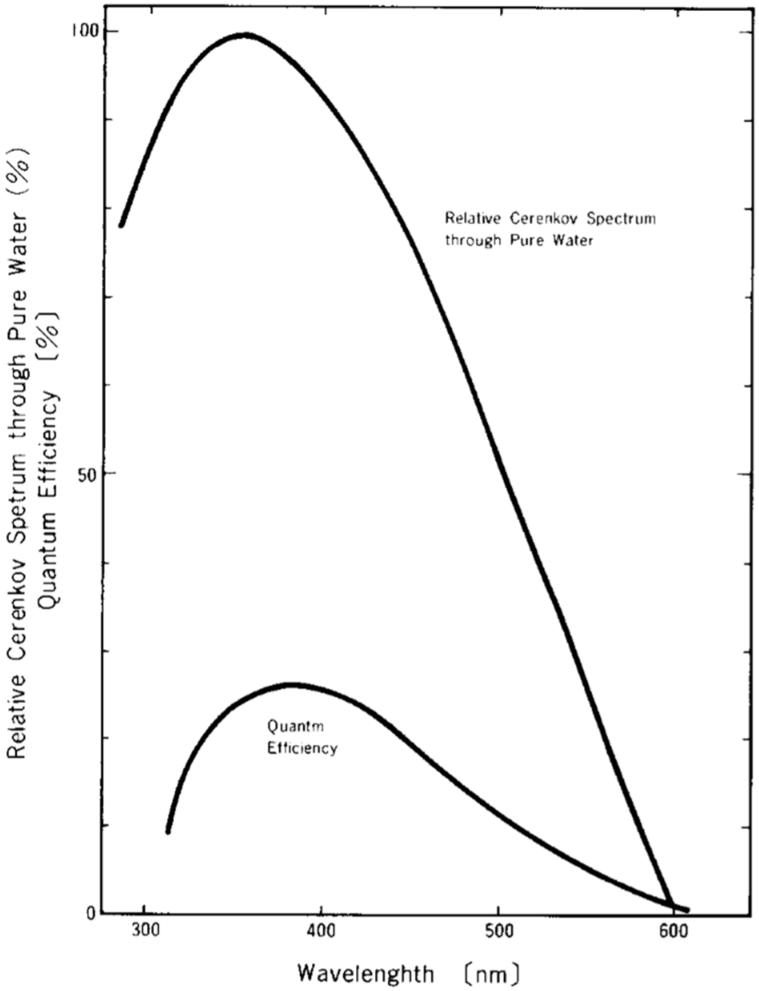

Figure 3.11: Quantum efficiency distribution of 20-inch PMT and relative Cherenkov light distribution as it passes through pure water of 15 m [27].

emission. The quantum efficiency peaks in the region between 300–600 nm which corresponds to the peak of the spectrum of Cherenkov light in water (Figure 3.11). At the wavelength of 390 nm, the quantum efficiency is 22%. Magnetic fields over 100 mG affect trajectories of photoelectrons in PMT and lead to inefficiency and degradation of the time resolution. The geomagnetism of about 450 mG at the location of Super-Kamiokande is reduced to 50 mG by 26 sets of Helmholtz coils which cover the horizontal direction and vertical direction of the tank [29].

After the PMT chain destruction in 2001, PMTs are covered with cases made of fiber-reinforced plastics (FRPs) and acrylic (Figure 3.12). There are holes on the slide of the cases to allow water to enter and exit the case. The transparency to photons vertically incident in the water of acrylic cover is 96% at a wavelength of 350 nm and does not significantly affect the detection of the Cherenkov light.

Figure 3.12: Photo of the case of the 20-inch PMT [25].

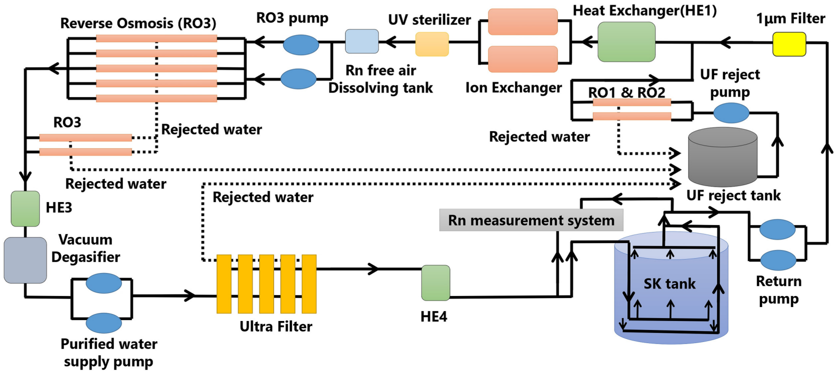

Figure 3.13: Schematic diagram of the SK-IV water system [30].

3.5 Water and air purification system

Spring water from the Kamioka mine is used for Super-Kamiokande. It is circulated in a water purification system with 60 ton/hour flow rate to get a long attenuation length of water (Figure 3.14). Dust and radioactive materials such as radon are removed from water in this system. Radon is the main source of radioactive materials in water and the background of low-energy events such as neutron capture and solar neutrino. The heat exchangers keep the water temperature at 13°C to prevent bacterial growth and keep water transparency, reduce the dark current in PMT, and suppress convection in the tank. Surviving bacteria are killed in the UV sterilizer.

To prevent radon in the air from dissolving into the water in the tank, radon-free air produced by a purification system is supplied to the top of the tank. Figure 3.14 shows the schematic diagram of the air purification system.

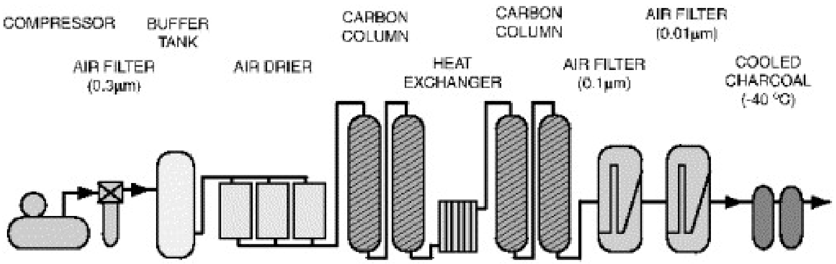

Figure 3.14: Schematic diagram of the air purification system [23].

3.6 Data acquisition system

Analog signals from PMTs are sent to electronics huts located on the top of the tank by coaxial cables. Lengths of all cables are set to 70 m to make the signal smearing effect and the propagation time of the signals uniform for all PMTs. In the electronics huts, signals are digitized by front-end modules, and the integrated charges (corresponding to the number of detected photons) and hit timings are sent to data acquisition computers. After they are sorted by time, events are selected by software trigger and recorded (Figure 3.15).

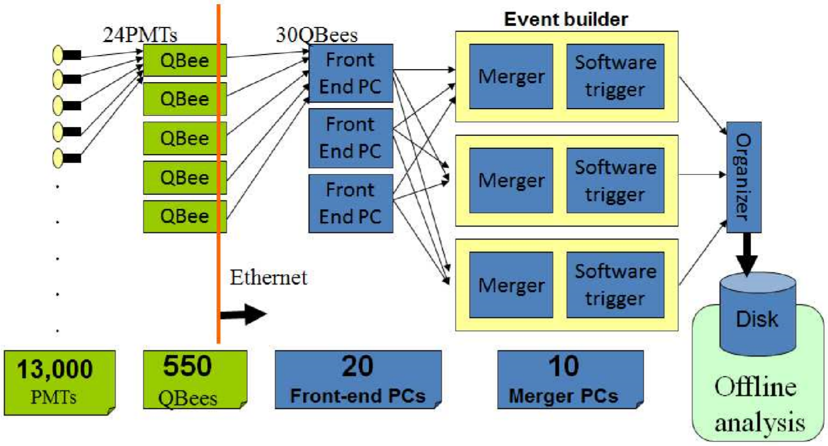

Figure 3.15: Schematic diagram of the data acquisition system for SK-IV [31].

From the SK-IV running period, a new front-end electronics module, QBEE (QTC-Based Electronics with Ethernet), has been used in the data acquisition system (Figure 3.16). In QBEE, QTC converts analog signals from PMTs to rectangular pulses whose leading edge represents the signal timing and width represents the integrated charge. The rectangular pulses are then digitized by TDC and read by FPGA for each 17 μs and recorded after the data compression. About 560 QBEE boards each with 24 input channels are operating synchronously at 60 MHz in SK.

If the number of hit PMTs in a sliding 200 ns time window exceeds the trigger threshold, a software trigger is issued and hits around the trigger timing are recorded. There are four trigger

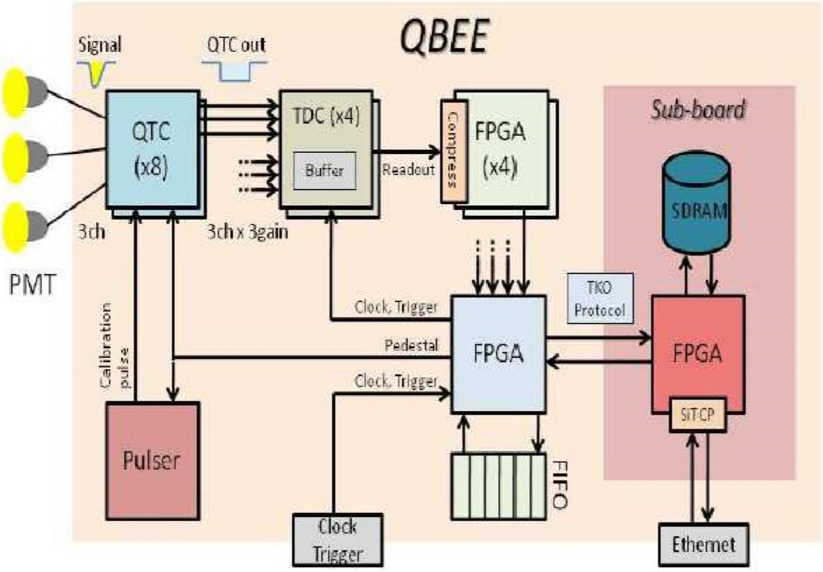

Figure 3.16: Schematic diagram of QBEE [31].

types for the ID in SK-IV as shown in Table 3.4. If the SHE trigger is issued without the OD trigger (which corresponds to ≥ 7 MeV energy deposit in the ID without response in the OD), a special trigger called AFT trigger is issued, and all PMT hits are recorded up to 535 μs after the SHE trigger timing. The AFT trigger information is used for a search to 2.2 MeV γ emitted from neutron capture on hydrogen as described in Section 7.5.

Table 3.4: Thresholds and time widths of the triggers. The trigger thresholds for SHE and SLE were changed during SK-IV, and only the initial and last values are shown.

Name	Threshold	Time width
SHE	$70 \rightarrow 58$	$[-5\,\mu\text{s}, +35\,\mu\text{s}]$
HE	50	$[-5\,\mu\text{s}, +35\,\mu\text{s}]$
LE	47	$[-5\,\mu\text{s}, +35\,\mu\text{s}]$
SLE	$34 \rightarrow 31$	$[-0.5\,\mu\text{s}, +1.0\,\mu\text{s}]$
OD	22	$[-5\,\mu\text{s}, +35\,\mu\text{s}]$

3.7 Scattering and absorption in water

Light is scattered and absorbed in water, affecting the hit pattern of the Cherenkov ring and the number of observed photoelectrons. In SK, lasers of four different wavelengths are injected from the top to the bottom of the detector to calibrate the coefficients of photon scattering and absorption.

The coefficients of photon scattering and absorption are parametrized as

$$\begin{aligned}
I(\lambda, l) &= I_0(\lambda) \exp\left(-\frac{l}{L(\lambda)}\right), && (3.4)\\
L(\lambda) &= \frac{1}{a_{\mathrm{abs}}(\lambda) + a_{\mathrm{sym}}(\lambda) + a_{\mathrm{asy}}(\lambda)}, && (3.5)\\
a_{\mathrm{abs}}(\lambda) &= P_0 \frac{P_1}{\lambda^4} + C, && (3.6)\\
a_{\mathrm{sym}}(\lambda) &= \frac{P_4}{\lambda^4}\left(1.0 + \frac{P_5}{\lambda^2}\right), && (3.7)\\
a_{\mathrm{asy}}(\lambda) &= P_6\left(1.0 + \frac{P_7}{\lambda^4}(\lambda - P_8)^2\right), && (3.8)\\
& && (3.9)
\end{aligned}$$

where l is the travel length of the light, $I_0(\lambda)$ is the initial light intensity, $I(\lambda, l)$ is the light intensity at l, $a_{\mathrm{abs}}(\lambda)$ is the absorption coefficient, $a_{\mathrm{sym}}(\lambda)$ is the symmetric scattering coefficient, $a_{\mathrm{asy}}(\lambda)$ is the asymmetric scattering coefficient, and $P_{0,\ldots,8}$ is the constant coefficient. Rayleigh scattering and the symmetric component of Mie scattering contribute to the symmetric scattering, and the asymmetric component of Mie scattering corresponds to the asymmetric scattering. Figure 3.17 shows the observed water parameters [29].

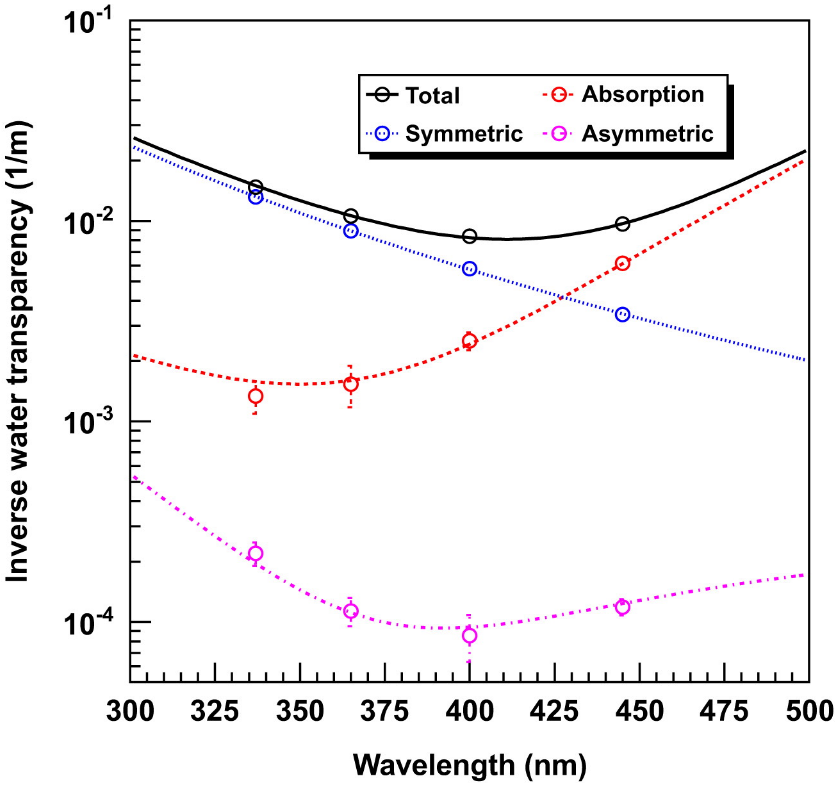

Figure 3.17: Water parameters in the measurements (points) and fitted functions (lines) [29]. The total of coefficients (black) consists of the absorption (red), symmetric (blue) and asymmetric (magenta) coefficients.

3.8 Energy scale calibration

As explained in Section 3.3, the energy of charged particles can be estimated from the number of observed photoelectrons. Calibration of the energy scale for the event reconstruction algorithm, fiTQun (details are described in Chapter 7), is performed using independent control samples with known energies.

1. Comparison of the number of photoelectrons and track length for cosmic ray muons (1–10 GeV/c)
2. Comparison of the number of photoelectrons and Cherenkov angle for cosmic ray muons (200–500 MeV/c)
3. Invariant mass of π^0 produced by neutrino interactions ($\sim$130 MeV/c for the total energy of two γ's)
4. Momentum distribution of electrons from muon decay (called as Michel electron) ($<$50 MeV/c)

Figure 3.18 shows the results of the absolute energy scale measurements [32]. The total absolute energy scale error is 2.09%.

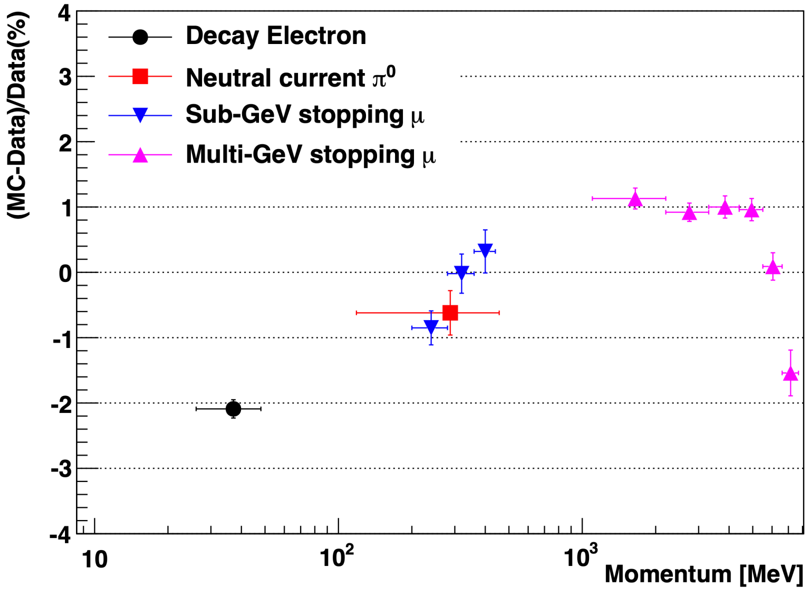

Figure 3.18: Deviations of the absolute energy scale between the data and simulation for events with the distance from the ID wall larger than 2 m [32]. The statistical uncertainty is denoted by the vertical error bars. The momentum range of each sample is shown by the horizontal error bar.

Chapter 4

Simulation

Although the proton decay events have not been observed yet, their detection efficiency is estimated by the Monte Carlo (MC) simulations. The proton decay simulation with 10^5 events was used to estimate the signal efficiency. Details of the simulations are described in this chapter.

The simulations consist of two steps, the primary interaction in the nucleus and the propagation of the particles in the detector. The interaction simulation determines the number of particles and the particle types, positions and momenta. Then, their trajectories in the detector, emission of Cherenkov light, propagation of photons in water, and the detection of photons are calculated by the detector simulation.

After the simulation, data reduction (Chapter 6), event reconstruction (Chapter 7) and selection of proton decay signals (Chapter 8) are applied to the output of the detector simulation as well as the observed data.

4.1 Proton decay

In the proton decay simulation, particles were generated from nuclei of hydrogen and oxygen in water within the inner detector (ID) of Super-Kamiokande (SK). Protons in a hydrogen atom are called free protons and the momenta are negligible to the momenta of outgoing particles from the proton decay. In this case, the momenta of μ^+ and K^0 from the proton decay of the $p \to \mu^+ + K^0$ channel are the same ($326.5\,\mathrm{MeV/c}$) and their directions are back-to-back due to the two-body decay. In contrast, protons in oxygen interact with other nucleons and are called bound protons. These bound protons experience Fermi motion. Due to Fermi motion, momentum distributions of μ^+ and K^0 from the decays of bound protons are different than those from free protons. Figure 4.1 shows momentum distribution for each proton state. The Fermi momentum distribution in the simulation is implemented using the measurement of electron-^{12}C scattering [33]. The effective mass of the bound proton is smaller than that of free protons due to interactions with the surrounding nucleons. The effective proton mass m'_p is calculated by subtracting the binding energy E_b from the proton rest mass m_p, where E_b is simulated for each nuclear state as a Gaussian random variable with a mean and a standard deviation of 39.0 MeV and 10.2 MeV for the s-state and 15.5 MeV and 3.82 MeV for the p-state, respectively. The ratio of protons in the s-state and p-state is taken to be 1:3 based on the nuclear shell model [34].

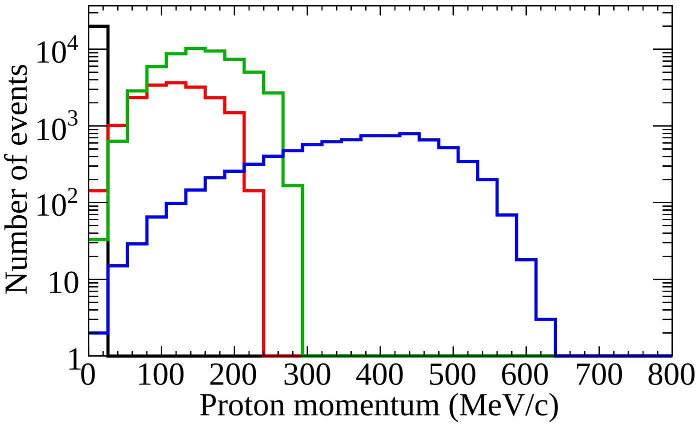

Figure 4.1: Proton momentum distributions of free (black), s-state (red), p-state (green) and correlated decay protons (blue).

Protons in an oxygen nucleus often decay as a pair with a nearby nucleon with an estimated probability of 10% for each proton decay, referred to as correlated decay [35].

4.2 Final state interaction

After the proton decay or neutrino interaction (described in Chapter 5), generated hadrons interact with surrounding nucleons. A custom semi-classical intranuclear cascade model is used for the simulation of hadron interactions in the nucleus. The scattering probability is calculated from the mean free path for every 0.2 fm step in the nucleus assuming the nucleon density of oxygen [36]. Pion scattering cross section in the low momentum region is based on the model by Salcedo *et al.* [37]. Fits to pion-nucleon scattering data are used at high momentum (more than 500 MeV/c) to estimate the mean free path. The kaon interaction model was updated since the previous analysis [1] as explained below.

In the nucleus, neutral kaon scattering is simulated assuming an eigenstate of K^0. Since K^+ and K^0 form an isospin doublet, the eigenstates of isospin can be represented by the superpositions of the scattering amplitudes of kaon and nucleon:

$$|1,1\rangle = \left|K^+,p\right\rangle, \tag{4.1}$$

$$|1,0\rangle = (\left|K^+,n\right\rangle + \left|K^0,p\right\rangle)/\sqrt{2}, \tag{4.2}$$

$$|1,-1\rangle = \left|K^0,n\right\rangle, \tag{4.3}$$

$$|0,0\rangle = (\left|K^+,n\right\rangle - \left|K^0,p\right\rangle)/\sqrt{2}. \tag{4.4}$$

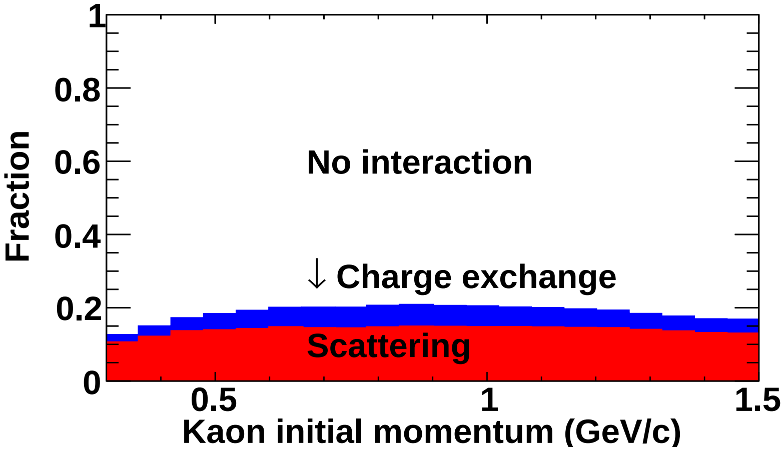

Figure 4.2: Fraction of K^0 interactions in the ^{16}O nucleus as a function of K^0 momentum. Elastic scattering (red) and charge exchange (blue) are simulated in the nucleus.

Therefore, kaon-nucleon scattering amplitudes can be represented as follows:

$$\left|K^+, p\right\rangle = \left|1, 1\right\rangle, \tag{4.5}$$

$$\left|K^+, n\right\rangle = (\left|1, 0\right\rangle + \left|0, 0\right\rangle)/\sqrt{2}, \tag{4.6}$$

$$\left|K^0, n\right\rangle = \left|1, -1\right\rangle, \tag{4.7}$$

$$\left|K^0, p\right\rangle = (\left|1, 0\right\rangle - \left|0, 0\right\rangle)/\sqrt{2}. \tag{4.8}$$

The scattering amplitudes of K^0 and a nucleon in the simulation were evaluated using (4.7) and (4.8) in which the eigenstates of isospin were obtained by the measurements of K^+ scattering [38] corresponding to (4.5) and (4.6). Only elastic scattering $K^0 + N \to K^0 + N$, where N is a nucleon (proton p or neutron n), and charge exchange $K^0 + p \to K^+ + n$ are simulated in the nucleus as they are relevant for K^0N interactions at the proton decay energy scale. If the momentum of the scattered nucleon is below the Fermi surface momentum, scattering is suppressed by the Pauli exclusion principle. The cross section of K^0 and ^{16}O scattering is calculated by scaling the cross section of the K^0 and nucleon scattering assuming they are proportional to the number of nucleons, referring to the experimental results [39]. Figure 4.2 shows the fraction of K^0 interactions in the nucleus as a function of K^0 momentum.

4.3 Detector simulation

After the hadrons leave the nucleus, the detector simulation determines how the generated charged particles are observed by the detector. The simulation is performed by a program called SKDETSIM. It is composed of a Fortran-based toolkit called Geant3 [40].

Since it is known that the Geant model for π meson scattering does not reproduce the data correctly, pion scattering is calculated by NEUT program [41]. The kaon interactions in water are

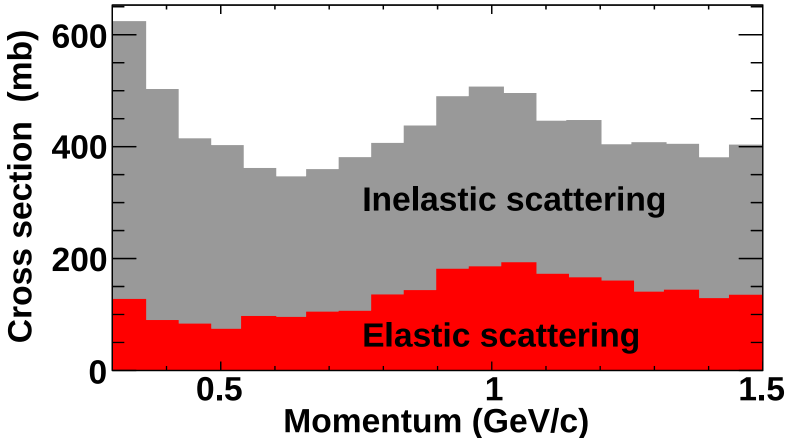

Figure 4.3: Cross section of K_L^0 in water. In the simulation of K_L^0 interactions, inelastic scattering (gray) and elastic scattering (red) are implemented.

simulated as the eigenstates of K_L^0 and K_S^0. The K^0 leaving the nucleus is randomly assigned to K_L^0 or K_S^0. Figure 4.3 shows the cross section of K_L^0 in the simulation. K_L^0 and K_S^0 cross sections are calculated from the K^0 and $\bar{K}^0$ scattering amplitudes.

$$|K_L, p\rangle = (|K^0, p\rangle + |\bar{K^0}, p\rangle)/\sqrt{2}, \tag{4.9}$$

$$|K_S, p\rangle = (|\bar{K^0}, p\rangle - |K^0, p\rangle)/\sqrt{2}. \tag{4.10}$$

The K^0N scattering amplitude is derived from the K^+N cross section [38] as written above while the $\bar{K}^0N$ scattering amplitude is calculated from the K^-N cross section [42]. Figure 4.4 shows the distance between the positions of proton decay and the end point of K_L^0 track, either by the decay or inelastic scattering. The mean free path calculated from the cross section is about 1 m in the water while the average travel length of K_L^0 with 326.5 MeV/c momentum is 13 m if it is in a vacuum. This means K_L^0 from proton decay scatters in water before it decays in most cases. The flight length becomes shorter than that in a vacuum if hadronic inelastic scattering occurs before K_L^0 decays.

In contrast, K_S^0 immediately decays in water with a lifetime of 90 ps. Coherent regeneration from K_L^0 to K_S^0 is also implemented both in the oxygen nucleus and in water. The regeneration probability in water is evaluated based on the results of a kaon scattering experiment using a carbon target [43]. In the oxygen nucleus, the regeneration probability is assumed to be proportional to its density relative to water. The fraction with regeneration is about 0.1% of the total $p \to \mu^+ + K_L^0$ events in the simulation.

The Cherenkov light generation and propagation in water and the PMT response are calculated by a custom program developed by the SK collaboration. When a charged particle moves in water with a velocity larger than the propagation of light, photons are produced by Cherenkov radiation (Section 3.3) along the particle's trajectory. These photons are propagated in water in which

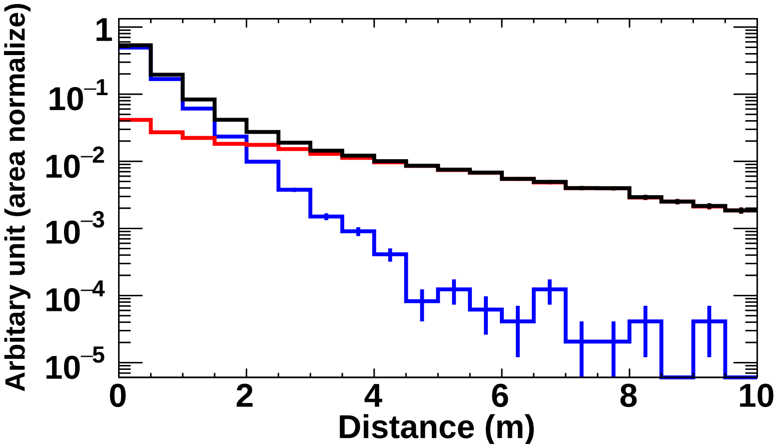

Figure 4.4: Distance between vertices of primary proton decay and the end point of K_L^0 track. Total $p \to \mu^+ K_L^0$ events (black) and the breakdown of K_L^0 decay events (red) and hadronic inelastic scattering events (blue) are shown.

Rayleigh scattering, Mie scattering, and absorption with water molecules are accounted for based on the parameters measured by the calibration of the detector (Section 3.7). The detection of photons by PMTs is simulated using quantum efficiency and collection efficiency based on measurements. Once the photons are detected by the PMTs, each of them is converted to a single photoelectron signal and accumulated as the output signal. The fluctuation of the single photoelectron signal and the timing resolution are also simulated based on the measurements.

Chapter 5

Atmospheric neutrino

As explained in Chapter 6, atmospheric neutrino events are the only possible background to the search for proton decay. The expected background rate in the proton decay search is also estimated using the atmospheric neutrino simulations as well as the proton decay simulation in Chapter 4.

Although the live time of SK used for this analysis is about 10 years, atmospheric neutrino MC samples equivalent to 500 years of operation are produced for this analysis to reduce statistical uncertainty in the background estimation. The number of the remaining background events in the MC simulation is then normalized by the live time to estimate the expected number of background events in the observed data.

Furthermore, atmospheric neutrino events are not only background events for proton decay but also important physics targets. Section 5.4 describes a new atmospheric neutrino event classification method using machine learning. The sensitivity of the neutrino oscillation measurements is improved by this method.

5.1 Neutrino flux

Cosmic rays are continuously raining down on the earth from space. Among various particles, the primary cosmic rays above several hundred MeV energy mainly consist of protons with a small fraction (about 9%) of helium nuclei. Most of the primary cosmic ray particles collide with nuclei in the atmosphere and produce secondary hadrons, mainly pions and kaons. The neutrinos produced from their decay are called atmospheric neutrinos (Figure 5.1). Atmospheric neutrinos are the dominant source of background in the proton decay search.

Atmospheric neutrino flux is calculated by independent groups such as Honda [46][47][48], Fluka [49] and Bartol [50]. Super-Kamiokande mainly employs Honda flux for analyses, and it is compared with the other models to evaluate the systematic uncertainty caused by the theoretical calculation.

As is clear from the production process, atmospheric neutrino flux depends on the amount of primary cosmic rays. The atmospheric neutrino flux calculation uses the data observed above the

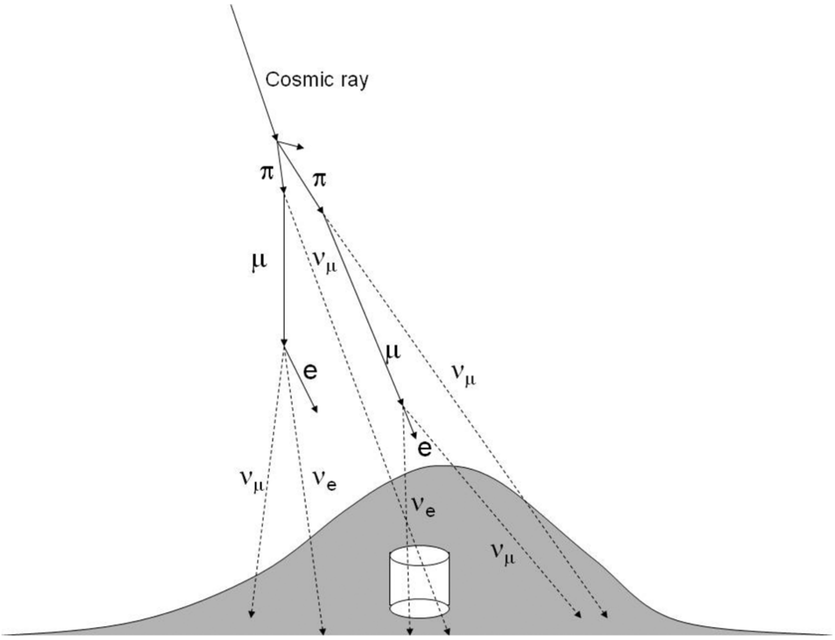

Figure 5.1: Schematic diagram of collisions between cosmic rays and nuclei in the atmosphere [44].

atmosphere to determine the primary cosmic ray flux as the input. The primary cosmic ray flux decreases rapidly with increasing energy as shown in Figure 5.2, and the atmospheric neutrino flux also decreases. Figure 5.3 shows the simulation of the atmospheric neutrino flux and the flux ratios at the Super-Kamiokande site. Collisions between primary cosmic rays and nuclei in the atmosphere generate mainly π mesons and K mesons. Charged pions decay in flight as follows:

$$\pi^+ \to \mu^+ + \nu_\mu \to e^+ + \nu_e + \bar{\nu}_\mu + \nu_\mu \tag{5.1}$$

$$\pi^- \to \mu^- + \bar{\nu}_\mu \to e^- + \bar{\nu}_e + \nu_\mu + \bar{\nu}_\mu \tag{5.2}$$

The right-hand plot in Figure 5.3 shows the ratios of atmospheric neutrino flux $(\nu_\mu + \bar{\nu}_\mu)/(\nu_e + \bar{\nu}_e)$ in the simulation. The ratio is close to two below the neutrino energy of 1 GeV as expected from Equation 5.1 and 5.2. At high energies, the ratio is greater than two and increases with the energy because the effective lifetime of the muon is longer for higher energy due to relativistic effects and such high-energy muons reach the ground before they decay.

5.2 Neutrino oscillation

Flavor eigenstates of neutrinos $(\nu_e, \nu_\mu, \nu_\tau)$ are superpositions of mass eigenstates (ν_1, ν_2, ν_3). Neutrinos are produced in the flavor eigenstates in the atmosphere, and the flavor compositions change before the observation in SK (known as neutrino oscillations). For example, the oscillation probability of two-generation oscillation is

$$P(\nu_\alpha \to \nu_\beta) = \sin^2 2\theta \sin^2 \left[\frac{1.27\Delta m^2[\mathrm{eV}^2]L[\mathrm{km}]}{E[\mathrm{GeV}]}\right], \tag{5.3}$$

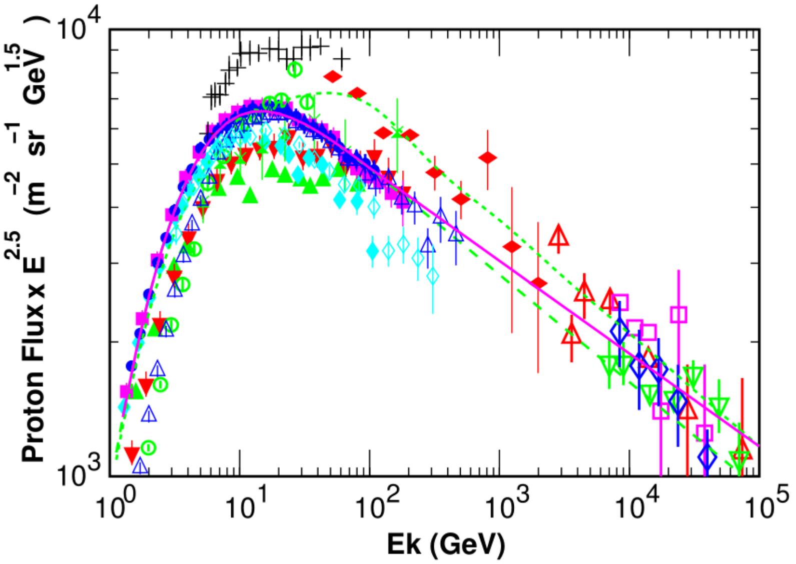

Figure 5.2: Primary cosmic ray flux of Honda model (solid line) and observations by several experiments (points) [46]. Calculations in a different way discussed in the paper (dashed line) and the previous model they used (dotted line) [45] are also shown.

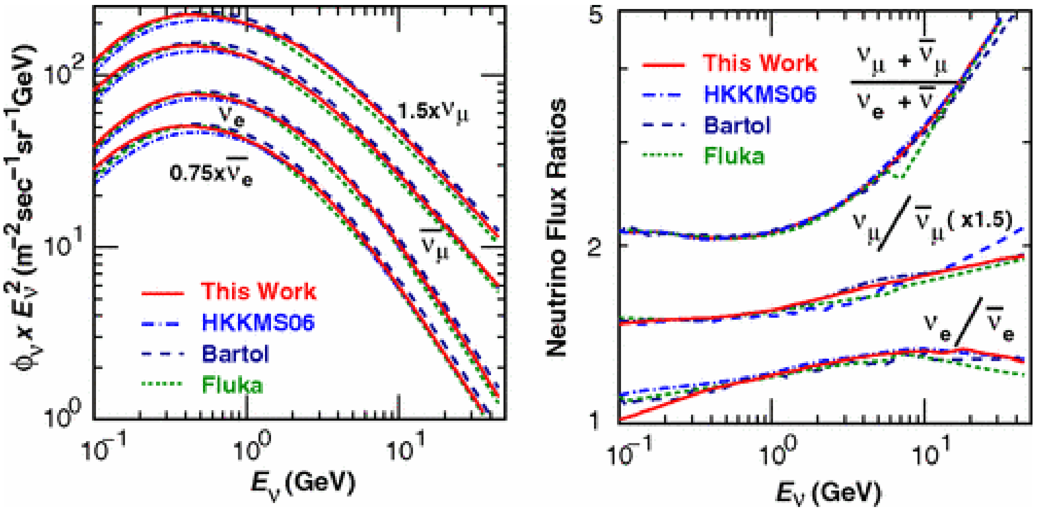

Figure 5.3: The atmospheric neutrino flux at Kamioka averaged over all directions (left) and the flux ratio (right) compared with other flux models, HKKM06 (previous calculation of this model), model by Bartol group [50] and model by FLUCA group [49]. Taken from [48].

where ν_α and ν_β are flavor eigenstates, θ is the mixing angle of mass eigenstates, Δm^2 is the mass-squared difference of the neutrino mass eigenvalues ($\Delta m^2 := m_2^2 - m_1^2$, where m_1 and m_2 are neutrino masses of ν_1 and ν_2). L and E are flight length and the energy of the neutrino. $P(\nu_\alpha \to \nu_\beta)$ can be nonzero if neutrinos have finite mass. Although neutrinos have three generations ν_e, ν_μ and ν_τ, if L/E is sufficiently smaller than the mass-squared difference, oscillations between specific generations become negligible. In this case, the oscillation probability is approximated by two-generation oscillation as expressed by Equation 5.3. This approximation is valid for atmospheric neutrino oscillation. The contribution from $\nu_\mu \to \nu_\tau$ oscillation is dominant for atmospheric neutrino observation in SK, and therefore the effect to the background estimation of the proton decay search is accounted for assuming two-flavor neutrino oscillation with parameters of $\sin^2 2\theta = 1.0$ and $\Delta m^2 = 2.5 \times 10^{-3}\,\mathrm{eV}^2$. Figure 5.4 shows the survival probability $P(\nu_\mu \to \nu_\mu)$ of neutrino predicted from ν_μ and ν_τ two-generation neutrino oscillation with parameters of $\sin^2 2\theta = 1.0$ and $\Delta m^2 = 2.5 \times 10^{-3}\,\mathrm{eV}^2$. Down-going muon neutrinos coming from the atmosphere above the detector rarely oscillate around 1 GeV energy due to the short flight length of 10–100 km. In contrast, the up-going muon neutrinos coming through the earth appears as a mixture with tau neutrinos and only half of them are observed as muon neutrinos on average around 1 GeV energy. As the energy threshold of the tau neutrino interactions is 3.5 GeV, which is higher than the typical energy of atmospheric neutrinos, they are rarely observed by the detector.

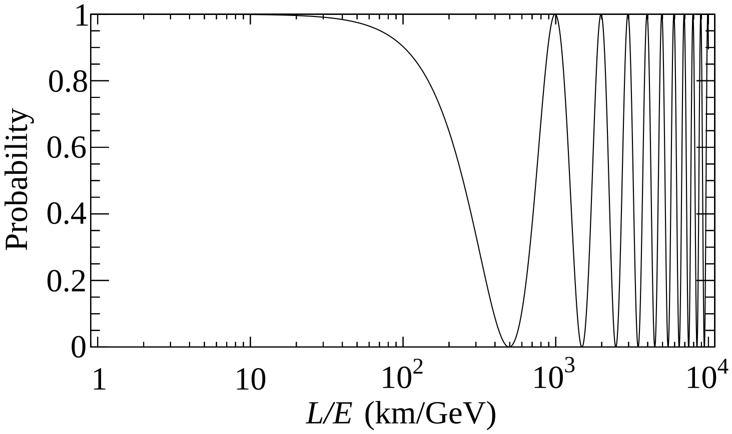

Figure 5.4: The survival probability $P(\nu_\mu \to \nu_\mu)$ of neutrino predicted from two-generation neutrino oscillation with parameters of $\sin^2 2\theta = 1.0$ and $\Delta m^2 = 2.5 \times 10^{-3}\,\mathrm{eV}^2$.

5.3 Neutrino interaction

Neutrino interactions are simulated by the NEUT program [41]. The neutrino interactions in the detector can be divided into two categories: charged current (CC) and neutral current (NC). In the case of the (quasi) elastic scattering, these interactions are expressed as:

- Charged current quasi-elastic (CCQE) scattering: $\nu_l + n \to l + p$
- Neutral current elastic (NCE) scattering: $\nu_l + N \to \nu_l + N$

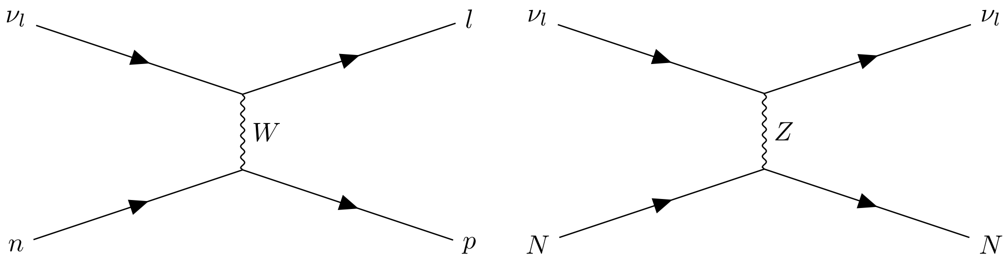

Figure 5.5: Feynman diagrams of $\nu_l + n \to l + p$ (left) and $\nu_l + N \to \nu_l + N$ (right).

Here, n is a neutron, p is a proton, and l is a charged lepton (e, μ, τ). Figure 5.5 shows the Feynman diagrams for these interactions. In the CC interaction, a neutrino is converted to a charged lepton via the exchange of a W boson. In contrast, the charge is invariant in the NC interaction via the exchange of a Z boson. Although neutrinos are not directly observed by the detector, it is possible to identify the flavor of the incident neutrino if the flavor (e, μ, τ) of the outgoing lepton is identified in the case of the CC interaction. As described in Section 3.1, Cherenkov rings made by electrons and muons can be distinguished in SK by their shapes, which are called e-like and μ-like, respectively. In contrast, particles with different charges, such as e^- and e^+, cannot be distinguished from the ring shape. Since the NC reaction is flavor-independent and the outgoing neutrinos cannot be observed, the original neutrino flavor cannot be identified. The cross section of CCQE scattering was formalized by the Llewellyn Smith model [52] and implemented in the simulation. As well as proton decay simulation, the scattering with hydrogen nucleus can be treated as a scattering with a free particle. In contrast, the effects of Fermi momentum and Pauli blocking are considered in the scattering with oxygen nuclei. A nucleus model is based on the local Fermi-gas model by Nieves *et al.* [53] and includes updates by Bourguille *et al.* [54].

In addition to the (quasi) elastic scattering, multi-nucleon scattering is implemented in the simulation:

$$\nu + n + N \to l + p + N. \tag{5.4}$$

This scattering is accompanied by several nucleons. Accelerator-based neutrino oscillation experiments such as K2K, MINOS and MiniBooNE found that the number of the observed CCQE-like events was larger than predicted by the models [55][56][57]. It indicates the existence of multi-nucleon interaction, and it is implemented as the Valencia model by Nieves *et al.* [53] in NEUT.

Elastic and quasi-elastic scatterings are dominant below 1 GeV (Figure 5.6). Above 1 GeV,

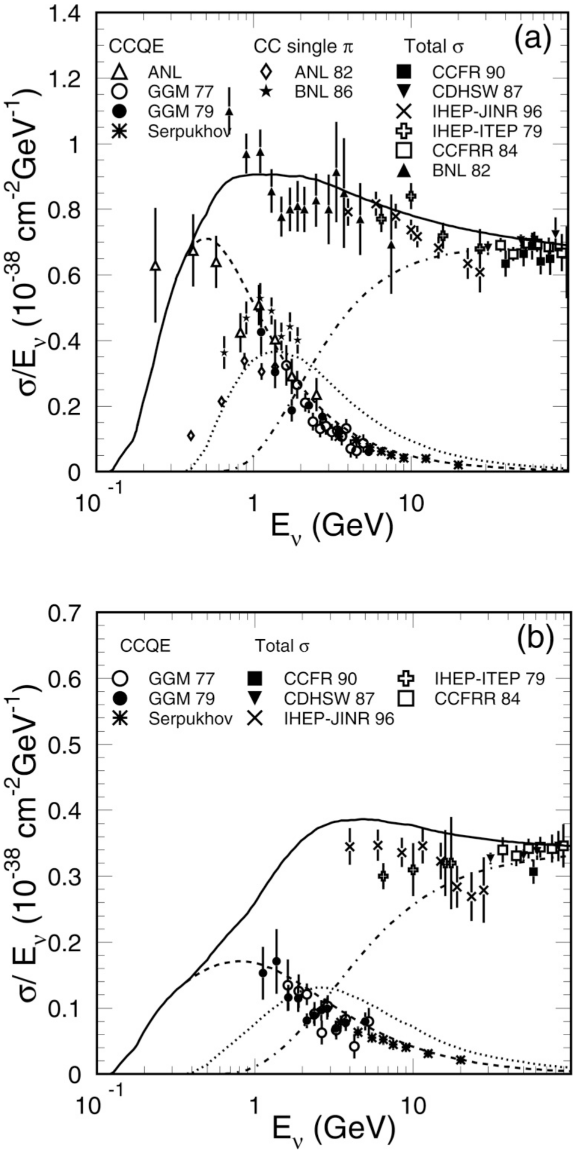

Figure 5.6: CC cross section of neutrino (a) and antineutrino (b) [51]. Total cross section (solid), quasi-elastic scattering (dotted), single meson production (dashed), DIS (chain) and observations (points) are shown.

hadrons are generated in addition to the outgoing leptons. Single meson production

$$\nu + N \to l + N' + \text{meson}\,(\pi, K, \rho, \dots), \tag{5.5}$$

$$\nu + N \to \nu + N' + \text{meson}\,(\pi, K, \rho, \dots) \tag{5.6}$$

and single gamma production

$$\nu + n \to l + p + \gamma, \tag{5.7}$$

$$\nu + N \to \nu + N + \gamma \tag{5.8}$$

are implemented in NEUT, and the pion production is the main reaction around 1 GeV. N and N' are the initial and final states of the nucleon. Single pion production is based on the Berger and Sehgal model [58]. The model consists of two steps. First, an intermediate baryon resonance state (N^*) is produced from hadronic current ($\nu + N \to l + N^*$). Second, it decays into a pion and a baryon ($N^* \to \pi + N'$). Since the reaction is divided into two stages, cross sections for single kaon, eta and gamma production also can be calculated by changing parameters such as the decay probability.

Pion production is the major interaction among meson productions. Coherent pion production

$$\nu + {}^{16}\mathrm{O} \to l + {}^{16}\mathrm{O} + \pi^+, \tag{5.9}$$

$$\nu + {}^{16}\mathrm{O} \to \nu + {}^{16}\mathrm{O} + \pi^0 \tag{5.10}$$

and diffractive pion production

$$\nu + p \to l + p + \pi^+, \tag{5.11}$$

$$\nu + p \to \nu + p + \pi^0 \tag{5.12}$$

are implemented in addition to the single pion production from baryon resonance decay. Coherent pion production is a pion production without breaking the target nucleus. The model is based on Berger and Sehgal [59]. Diffractive pion production is also a pion production with a proton implemented by Rein [60].

In the high energy region of more than several GeV, deep inelastic scattering (DIS) is a dominant interaction:

$$\nu + N \to l + N' + \text{hadrons}, \tag{5.13}$$

$$\nu + N \to \nu + N' + \text{hadrons}. \tag{5.14}$$

The interaction can be described as the scattering between a neutrino and a quark. When the invariant mass of the hadronic system (W) is below $2\,\mathrm{GeV/c^2}$, only multiple meson productions are considered to avoid double counting of single meson production events with the cross section as a function of the pion multiplicity which depends on W. The mean multiplicity of charged hadrons is estimated from the results of bubble chamber experiments [61][62]. Interactions with W larger than $2\,\mathrm{GeV/c^2}$ are simulated by PYTHIA [63].

5.4 Event classification of atmospheric neutrino

The discovery of neutrino oscillations revealed the existence of neutrino mass. However, it is not determined yet whether the order of mass (called mass ordering or mass hierarchy) is normal ($m_1 < m_2 \ll m_3$) or inverted ($m_3 \ll m_1 < m_2$) although the normal ordering is indicated at 91.9%–94.5% confidence level by SK-T2K combined analysis [64]. Observation of atmospheric neutrinos has a sensitivity to the mass ordering as the oscillation probability depends on it. Upward-going atmospheric neutrinos come from the opposite side of the earth and are observed in the detector. Figure 5.7 shows the atmospheric neutrino oscillation probabilities for each mass ordering. The oscillation probabilities depend on the neutrino energy and zenith angle θ (Figure 5.8). If it is a normal ordering, the neutrino oscillation probability $P(\nu_\mu \rightarrow \nu_e)$ is enhanced for upward-going events in a few GeV energy due to the neutrino interaction with the earth (matter effects). On the other hand, $P(\bar{\nu}_\mu \rightarrow \bar{\nu}_e)$ is enhanced if it is an inverted mass ordering. Therefore, observation of ν_e and $\bar{\nu}_e$ events in a few GeV leads to the understanding of the neutrino mass ordering.

In a few GeV energy, multi-ring events are observed as DIS is a dominant interaction. The identification of the neutrino flavor for multi-ring events is more difficult than that for single-ring events mainly from CCQE scattering below 1 GeV. The neutrino flavor can be estimated from the particle type of the lepton in CCQE scattering (single-ring event), while Cherenkov rings from hadrons are observed in addition to the ring from the charged lepton. Currently, atmospheric neutrino events are classified by the log-likelihood (LL) method based on the variables reconstructed from the PMT hits. To improve the event classification efficiencies, an alternative method based on the neural network (NN) has been developed for multi-GeV multi-ring event samples (multi-GeV events have E_{vis} above 1.33 GeV, where E_{vis} is electron equivalent total energy deposit in the detector) in the SK-IV period.

Events are classified by the NN from the input variables based on the knowledge accumulated from the training samples. We employed input variables listed in Table 5.1, following the current analysis based on the LL method [64]. Figure 5.9 shows the distributions of these variables. The atmospheric neutrino simulation is compared with the data of downward-going neutrino events ($\cos\theta > 0.4$, θ is a zenith angle) to avoid bias in the resonance region.

Multi-GeV multi-ring events are classified into 4 types.

- ν_e-like: ν_e charged current (CC) interaction as a correct class
- $\bar{\nu}_e$-like: $\bar{\nu}_e$ CC interaction as a correct class

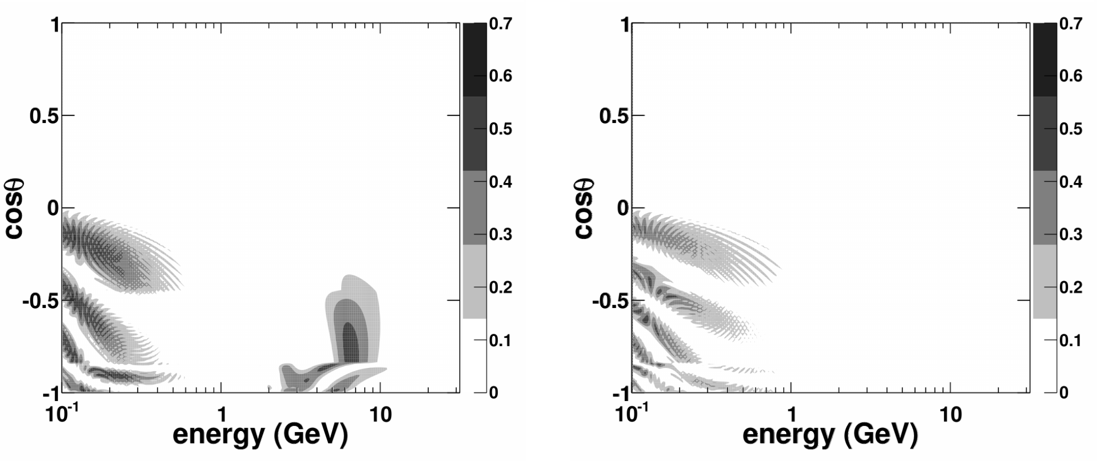

$P(\nu_\mu \to \nu_e)$, normal ordering $P(\bar{\nu}_\mu \to \bar{\nu}_e)$, normal ordering

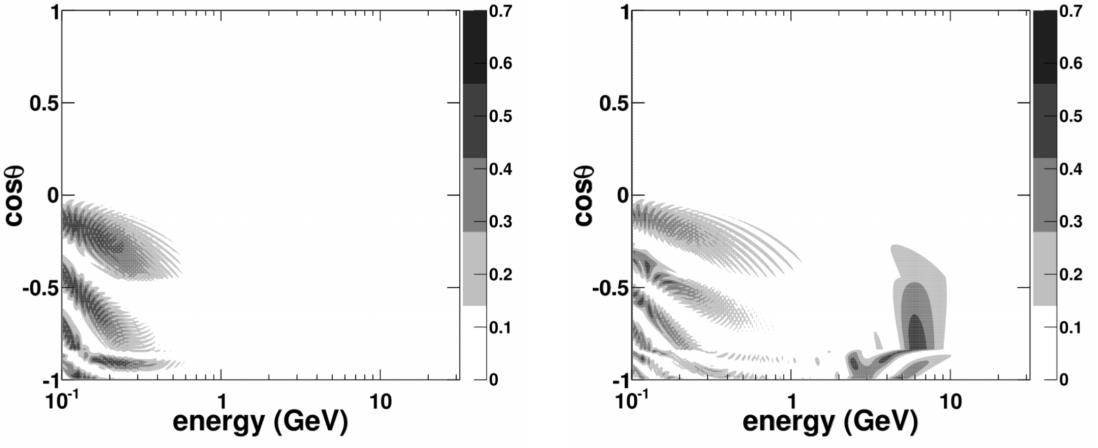

$P(\nu_\mu \to \nu_e)$, inverted ordering $P(\bar{\nu}_\mu \to \bar{\nu}_e)$ inverted ordering

Figure 5.7: Atmospheric neutrino oscillation probability $P(\nu_\mu \to \nu_e)$ and $P(\bar{\nu}_\mu \to \bar{\nu}_e)$ assuming normal (top) and inverted (bottom) mass ordering. The horizontal axis shows the neutrino energy, the vertical axis shows the zenith angle to the entering neutrino in the detector, and the color scale shows the oscillation probability assuming $|\Delta m^2_{32}| = 2.5 \times 10^{-3}$ eV, $\sin^2\theta_{23} = 0.5$, $\sin^2\theta_{13} = 0.021$, $\delta_{CP} = 0$.

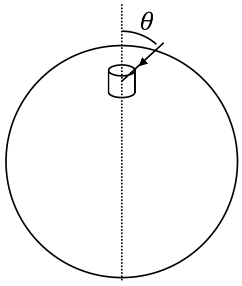

Figure 5.8: Schematic diagram of the definition of the zenith angle θ for the atmospheric neutrino. The large circle is the earth, the cylinder is the SK detector, and the arrow is the atmospheric neutrino.

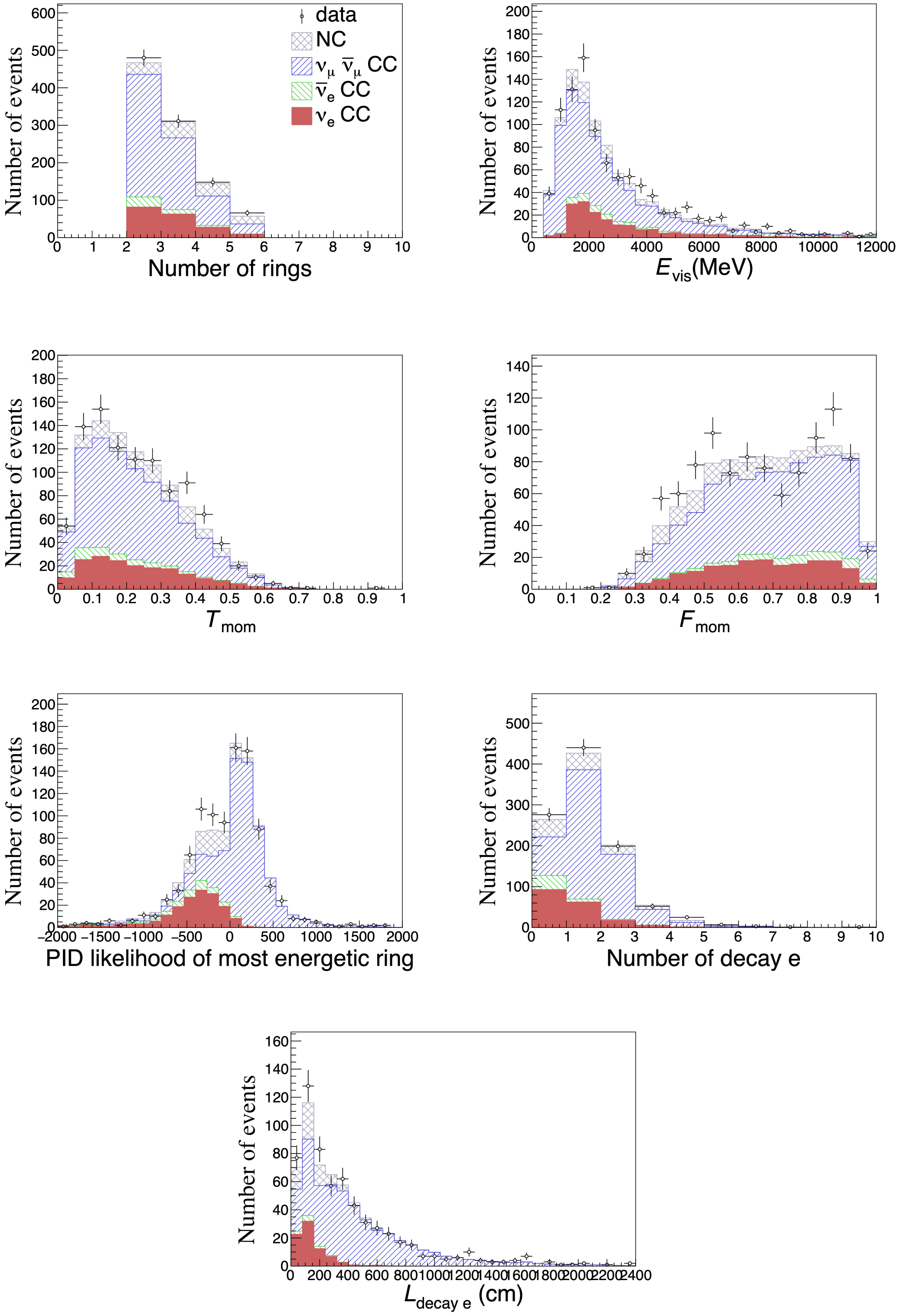

Figure 5.9: Distributions of the number of rings, $E_{\rm vis}$, $T_{\rm mom}$, $F_{\rm mom}$, PID, the number of Michel electrons and $L_{\text{decay } e}$ in the SK-IV period. The data (points) with statistical error bar are compared with the atmospheric neutrino simulation of ν_e CC (red), $\bar{\nu}_e$ CC (green), ν_μ and $\bar{\nu}_\mu$ CC (blue) and NC (gray) events. Downward-going events ($\cos\theta > 0.4$, θ is a zenith angle) after FCFV selection (described in Section 6.6) are shown. The atmospheric neutrino simulation is normalized by the live time.

Table 5.1: Input variables used in NN

Name	Definition
N_{ring}	Number of rings
E_{vis}	Electron equivalent total energy deposit
T_{mom}	Fraction of transverse momentum to the total visible energy
F_{mom}	Fraction of the momentum of the most energic ring to the total visible energy
$N_{\mathrm{decay}\,e}$	Number of Michel electron
$L_{\mathrm{decay}\,e}$	Distance between Michel e vertex and primary vertex
PID	Likelihood of particle type identification of the most energic ring

- μ-like: ν_μ and $\bar{\nu}_\mu$ CC interaction as a correct class
- Others: Neutral current (NC) interaction and ν_τ and $\bar{\nu}_\tau$ CC interaction as a correct class

The neural network consists of three layers. The activation function is ReLU, and the batch normalization [65] is adopted before each activation. The neural network is trained by 300 years of atmospheric neutrino simulation. The performance is evaluated with respect to the efficiency and contamination by using 100 years of atmospheric neutrino simulation which is independent of the training samples. The efficiency is defined as the fraction of correctly identified events in each interaction (ν_e CC, $\bar{\nu}_e$ CC, ν_μ or $\bar{\nu}_\mu$ CC, NC or tau neutrino events). The contamination is defined as the fraction of misidentified events in each category (ν_e-like, $\bar{\nu}_e$-like, μ-like, others).

Results of the classification are shown in Table 5.2. Compared to the LL method, ν_e efficiency is increased by a factor of 1.3 by the NN method with the comparable contamination.

Table 5.2: Results of the selection by NN

	Efficiency(%)		Contamination(%)	
	LL	NN	LL	NN
ν_e-like	34.4	46.7	54.0	52.8
$\bar{\nu}_e$-like	60.4	63.1	76.1	76.1
μ-like	77.0	85.9	7.6	8.9
others	55.6	47.4	56.7	39.6

Figure 5.10 shows ν_e event distributions of transverse momentum T_{mom} and fraction of most energic ring momentum F_{mom}. These show that the NN selected additional ν_e events in high T_{mom} and low F_{mom} region with respect to the LL method. This indicates that the NN is optimized to identify events with energetic hadrons and improves ν_e selection efficiency.

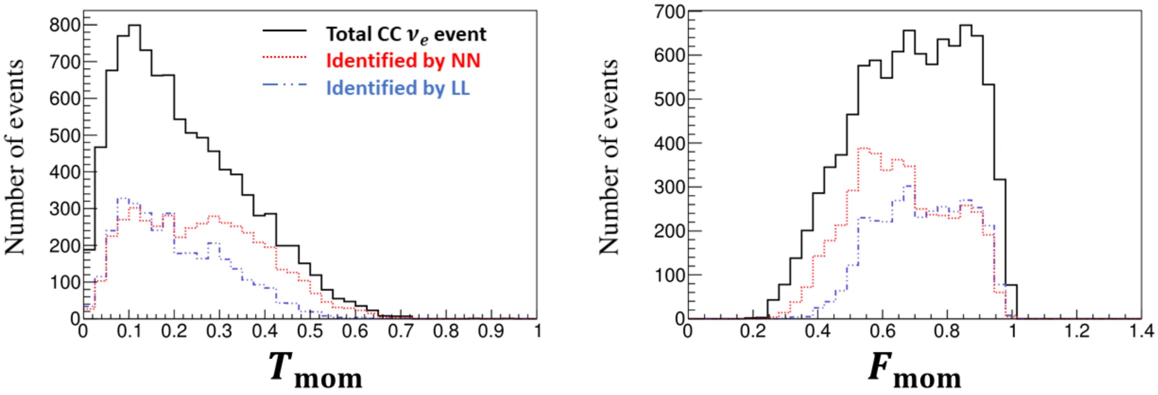

Figure 5.10: Distributions of the fraction of the transverse momentum (left) and the most energic ring momentum (right). From total ν_e CC events (black), the NN method (red) and LL method (blue) classified ν_e-like events.

Chapter 6

Data reduction

As described in Section 3.2, if a proton in water decays and the generated charged particles deposit all energy in the ID, Cherenkov light is observed only in the inner detector (ID) and no response should be observed in the outer detector (OD). These events are called fully contained events (FC events), and they are selected for the proton decay analysis. Similarly, if a neutrino interacts with a nucleus or electron in water and generated charged particles that deposit all of their energy in the ID, they are also selected as the FC events and used for the study of neutrino oscillation and other physics. The FC atmospheric neutrino event can be the background of the proton decay search. The number of FC atmospheric neutrino events observed in SK is about ten events per day. In addition to neutrinos, cosmic ray muons are observed by the SK detector. Two cosmic ray muons per $10\,\mathrm{cm}^2$ per second are poured on the Earth, but since SK is located 1000 m underground (which is equivalent to 3000 m of water), the muon rate is suppressed by a factor 10^5 and two muons per second are observed in the SK detector with a diameter of about 40 m. The emission of light due to radioactive isotopes in the detector and discharges in the circuit of PMTs (called flasher events) is also observed as background events. These events must be removed to search for proton decay events. The FC reduction in the SK-IV period consists of several steps as described in this chapter. To efficiently remove backgrounds, simple conditions are applied first, and in later steps, the remaining backgrounds are removed by the conditions optimized for the characteristics of each type of background. In the SK-II running period, some cut thresholds were different because the number of photomultiplier tubes (PMTs) was about half of the other periods. The FC reduction is applied not only for the data but also for the simulation which is used for the estimation of the signal efficiency and expected backgrounds in Chapter 8.

Figure 6.1 shows examples of FC atmospheric neutrino, cosmic ray muon, flasher and low-energy events.

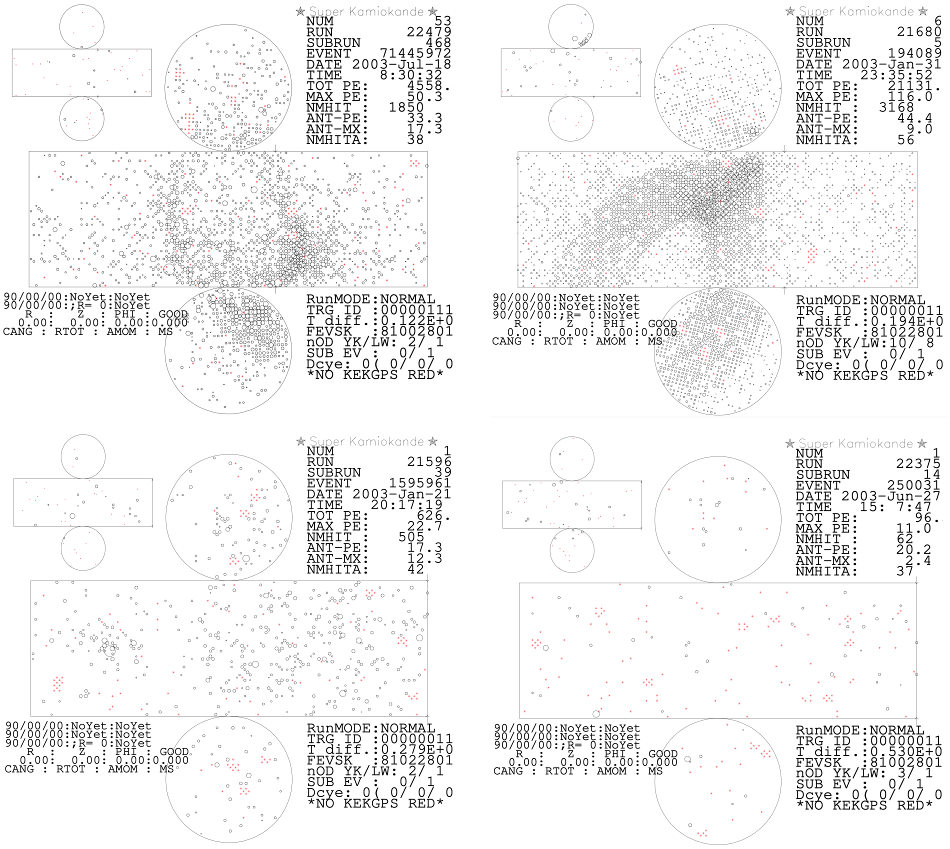

```
Super Kamiokande
NUM            53
RUN         22479
SUBRUN        468
EVENT    71445972
DATE  2003-Jul-18
TIME      8:30:32
TOT PE:     4558.
MAX PE:      50.3
NMHIT :   1850
ANT-PE:      33.3
ANT-MX:      17.3
NMHITA:     38
90/00/00:NoYet:NoYet
90/00/00:;R= 0:NoYet
  R   :   Z   : PHI  : GOOD
 0.00:   0.00: 0.00:0.000
CANG : RTOT : AMOM : MS
RunMODE:NORMAL
TRG ID :00000111
T diff.:0.122E+0
FEVSK  :81002801
nOD YK/LW: 2/ 1
SUB EV :   0/ 1
Dcye: 0( 0/ 0/ 0
*NO KEKGPS RED*
```

```
Super Kamiokande
NUM             6
RUN         21680
SUBRUN          5
EVENT      194089
DATE  2003-Jan-31
TIME     23:35:52
TOT PE:    21131.
MAX PE:     116.0
NMHIT :   3168
ANT-PE:      44.4
ANT-MX:       9.0
NMHITA:     56
90/00/00:NoYet:NoYet
90/00/00:NoYet:NoYet
90/00/00:;R= 0:NoYet
  R   :   Z   : PHI  : GOOD
 0.00:   0.00: 0.00:0.000
CANG : RTOT : AMOM : MS
RunMODE:NORMAL
TRG ID :00000011
T diff.:0.194E+0
FEVSK  :81022801
nOD YK/LW:10/ 8
SUB EV :   0/ 1
Dcye: 0( 0/ 0/ 0
*NO KEKGPS RED*
```

```
Super Kamiokande
NUM             1
RUN         21596
SUBRUN         39
EVENT     1595961
DATE  2003-Jan-21
TIME     20:17:19
TOT PE:      626.
MAX PE:      22.7
NMHIT :    505
ANT-PE:      17.3
ANT-MX:      12.3
NMHITA:     42
90/00/00:NoYet:NoYet
90/00/00:NoYet:NoYet
90/00/00:;R= 0:NoYet
  R   :   Z   : PHI  : GOOD
 0.00:   0.00: 0.00:0.000
CANG : RTOT : AMOM : MS
RunMODE:NORMAL
TRG ID :00000011
T diff.:0.279E+0
FEVSK  :81022801
nOD YK/LW: 2/ 1
SUB EV :   0/ 1
Dcye: 0( 0/ 0/ 0
*NO KEKGPS RED*
```

```
Super Kamiokande
NUM             1
RUN         22375
SUBRUN         14
EVENT      250031
DATE  2003-Jun-27
TIME     15: 7:47
TOT PE:       96.
MAX PE:      11.0
NMHIT :     62
ANT-PE:      20.2
ANT-MX:       2.4
NMHITA:     37
90/00/00:NoYet:NoYet
90/00/00:NoYet:NoYet
90/00/00:;R= 0:NoYet
  R   :   Z   : PHI  : GOOD
 0.00:   0.00: 0.00:0.000
CANG : RTOT : AMOM : MS
RunMODE:NORMAL
TRG ID :00000011
T diff.:0.530E+0
FEVSK  :81002801
nOD YK/LW: 3/ 1
SUB EV :   0/ 1
Dcye: 0( 0/ 0/ 0
*NO KEKGPS RED*
```

Figure 6.1: Typical event displays of FC atmospheric neutrino (left top), cosmic ray muon (right top), flasher (left bottom) and low-energy (right bottom) events. The points show the position of PMTs in the ID, and the size of the circles corresponds to the observed charge. The small plot in the top left side for each figure is the OD hit PMT distribution.

6.1 First reduction

About 10^6 events are recorded in a day and most of them are due to cosmic ray muons or low-energy radioactive backgrounds. The following conditions are applied as the first step in the FC reduction to remove such backgrounds.

1. $PE_{300} > 200$ photoelectrons (p.e.'s)

   The total number of p.e.'s observed in the ID within 300 ns (PE_{300}) is more than 200 p.e.'s.

2. $NHITA_{800} \leq 55$

   The number of hit PMTs in the OD in ±400 ns around the event trigger time ($NHITA_{800}$) is below 55.

The threshold of the first condition corresponds to a momentum of 22 MeV/c for an electron. Most of the low-energy events such as radioactive backgrounds (several MeV energy scale) are rejected by this cut. The second condition is intended to cut cosmic ray muons passing through the OD. The event rate in SK is reduced from 10^6 events/day to about 3000 events/day by these cuts.

6.2 Second reduction

In the second step of the FC reduction, events satisfy the following conditions are selected.

1. $PE_{max}/PE_{300} < 0.5$

   The ratio of the highest number of p.e.'s in all hits of the ID PMTs (PE_{max}) and the total number of photoelectrons (PE_{300}) should be below 0.5.

   Figure 6.2 shows the PE_{max}/PE_{300} distribution.

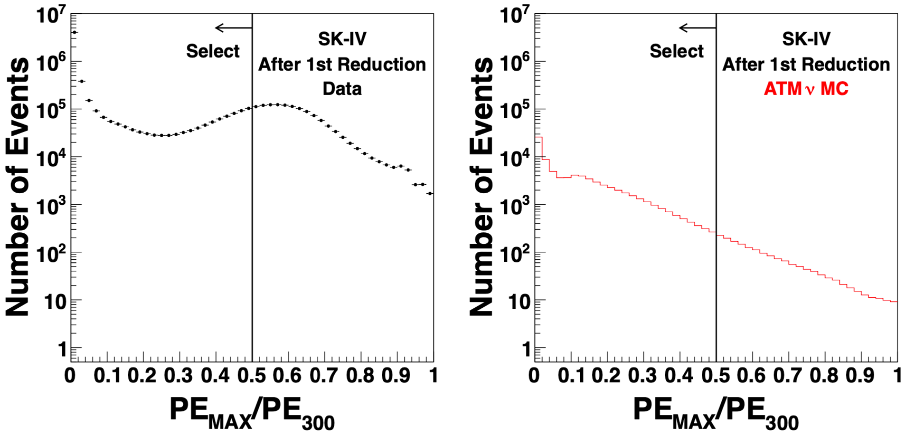

Figure 6.2: PE_{max}/PE_{300} distribution of data (left) and atmospheric neutrino simulation (right) after the first reduction in SK-IV [67]. The atmospheric neutrino events are normalized by SK-IV live time.

2. $\mathrm{NHITA}_{800} \leq 30$ or $\mathrm{PE}_{\mathrm{tot}} \geq 100000$ p.e.'s

   The number of hits in the OD (NHITA_{800}) should be below 25, or the total number of p.e.'s in the ID ($\mathrm{PE}_{\mathrm{tot}}$) should be more than 100000. Figure 6.3 shows the NHITA_{800} distribution.

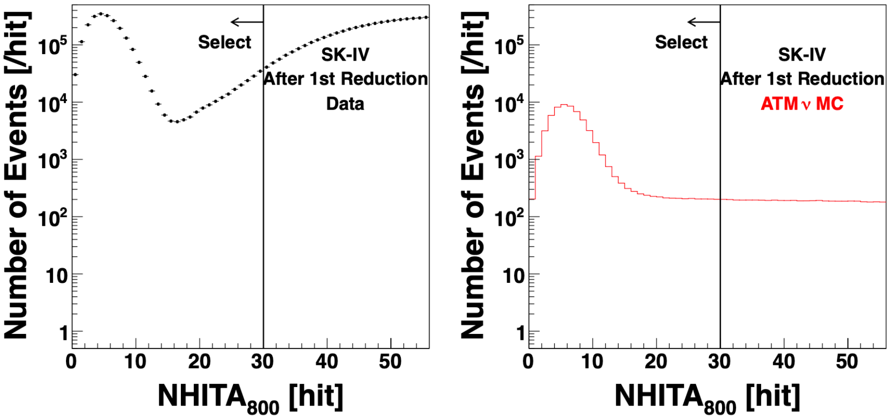

Figure 6.3: NHITA_{800} distribution of data (left) and atmospheric neutrino simulation (right) after the first reduction in SK-IV [67]. The atmospheric neutrino events are normalized by SK-IV live time.

The first condition rejects events that have one PMT with significantly larger signals than other PMTs such as due to the electric noise of PMTs. The second condition rejects cosmic ray events left from the first FC reduction with a tighter cut while very high energy FC events with light leakage into the OD side are accepted. The event rate is reduced to about 600 events/day by these cuts.

6.3 Third reduction

The third reduction was designed to reduce specific backgrounds.

- Hard muon cut

  Cosmic ray muons which have energy more than 1 TeV, hard muon, are rejected by $\mathrm{NHITA}_{500} \geq 40$. Here NHITA_{500} is the number of p.e.'s within the OD sliding 500 ns time window set at a time to maximize it.

- Through-going muon cut

  Through-going muon fitter is applied to events that have more than 1000 ID PMT hits with $\mathrm{PE}_{\mathrm{max}} > 230$ p.e.'s. The fitter finds the entering and exiting points of the through-going muon in the ID and returns goodness which represents the consistency of the observed PMT signals and the prediction from muons based on the time information. Using this fitter, the rejection criteria are defined as follows:

  - Goodness > 0.75
  - $\text{NHITA}_{\text{in800}} \geq 10$ or $\text{NHITA}_{\text{out800}} \geq 10$

  $\text{NHITA}_{\text{in800}}$ and $\text{NHITA}_{\text{out800}}$ are the number of hit PMTs located within 8 m from entering and exit points, respectively. These criteria reject events with responses in the OD at the entering and exiting points of the muon.

- Stopping muon cut

  As well as through going muon cut, the following cuts are applied using the fitter to find the entering point.

  - Goodness ≥ 0
  - $\text{NHITA}_{\text{in800}}$ in ≥ 10

  It rejects cosmic ray muons that enter from outside the detector and stop in the ID. In this case, the OD shows a response only near the entering point. Figure 6.4 shows examples of through-going muon and stopping muon events.

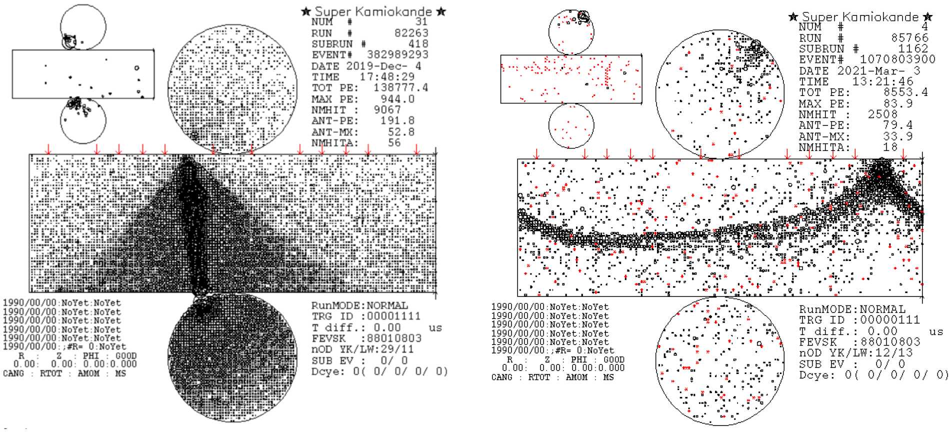

```
★ Super Kamiokande ★
NUM   #          31
RUN   #       82263
SUBRUN #        418
EVENT#  382989293
DATE 2019-Dec- 4
TIME   17:48:29
TOT PE:  138777.4
MAX PE:    944.0
NMHIT :  9067
ANT-PE:    191.8
ANT-MX:     52.8
NMHITA:     56

1990/00/00:NoYet:NoYet
1990/00/00:NoYet:NoYet
1990/00/00:NoYet:NoYet
1990/00/00:NoYet:NoYet
1990/00/00:NoYet:NoYet
1990/00/00:;#R= 0:NoYet
   R  :   Z  : PHI : GOOD
  0.00:  0.00: 0.00:0.000
CANG : RTOT : AMOM : MS

RunMODE:NORMAL
TRG ID :00001111
T diff.: 0.00     us
FEVSK  :88010803
nOD YK/LW:29/11
SUB EV :   0/ 0
Dcye: 0( 0/ 0/ 0/ 0)
```

```
★ Super Kamiokande ★
NUM   #           4
RUN   #       85766
SUBRUN #       1162
EVENT#  1070803900
DATE 2021-Mar- 3
TIME   13:21:46
TOT PE:     8553.4
MAX PE:       83.9
NMHIT :   2508
ANT-PE:       79.4
ANT-MX:       33.9
NMHITA:       18

1990/00/00:NoYet:NoYet
1990/00/00:NoYet:NoYet
1990/00/00:NoYet:NoYet
1990/00/00:NoYet:NoYet
1990/00/00:NoYet:NoYet
1990/00/00:;#R= 0:NoYet
   R  :   Z  : PHI : GOOD
  0.00:  0.00: 0.00:0.000
CANG : RTOT : AMOM : MS

RunMODE:NORMAL
TRG ID :00000111
T diff.: 0.00     us
FEVSK  :88010803
nOD YK/LW:12/13
SUB EV :   0/ 0
Dcye: 0( 0/ 0/ 0/ 0)
```

Figure 6.4: Typical event display of through-going muon (left) and stopping muon (right) events.

- Cable hole muon cut

  The high voltage and signal cables from the PMTs are bundled into twelve and pulled out through four holes in the top of the tank (Figure 6.5). If a cosmic ray muon passes through this cable bundle, it will enter the ID without leaving PMT hits in the OD. In that case, it cannot be removed by the first and second reductions. To reject these events, plastic scintillators with 2 m×2.5 m are installed on the cable holes as VETO counters. Events are rejected if the following criteria are satisfied.

  - There is a signal from one of the plastic scintillators

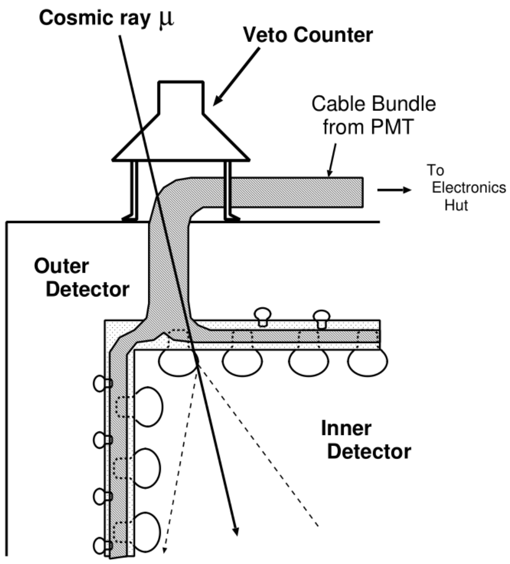

Figure 6.5: Schematic diagram of cable hole muon events and a VETO counter [66].

  - A distance from a reconstructed vertex (position where the charged particle is generated) in the ID to the cable hole is within 4 m.

- Coincidencce muon cut

  If a cosmic ray muon event happens to coincide with a low energy event, the timing of the OD signals is shifted and the muon is not removed by the former cuts. These events are rejected by the following rejection criteria.

  - $\mathrm{NHITA_{off}} \geq 20$

    The number of OD hits within the time window of 400–900 ns from the event trigger (called off-time window), $\mathrm{NHITA_{off}}$, is more than 20.

  - $\mathrm{PE_{off}} > 5000$ p.e.'s

    The number of p.e.'s in the ID within the off-time window, $\mathrm{PE_{off}}$, is more than 5000.

  Figure 6.6 shows an example of coincidence muon events.

- Flasher event cut

  The spontaneous discharge from PMTs causes events called flasher events. Flasher events often have a broad timing distribution compared to events produced by charged particles. Events are rejected if they satisfy the following condition.

  - $\mathrm{NMIN_{100}} \geq 20$

    The minimum number of ID hits in a sliding 100 ns time window from +300 ns to +800 ns after the trigger, $\mathrm{NMIN_{100}}$, is more than 20.

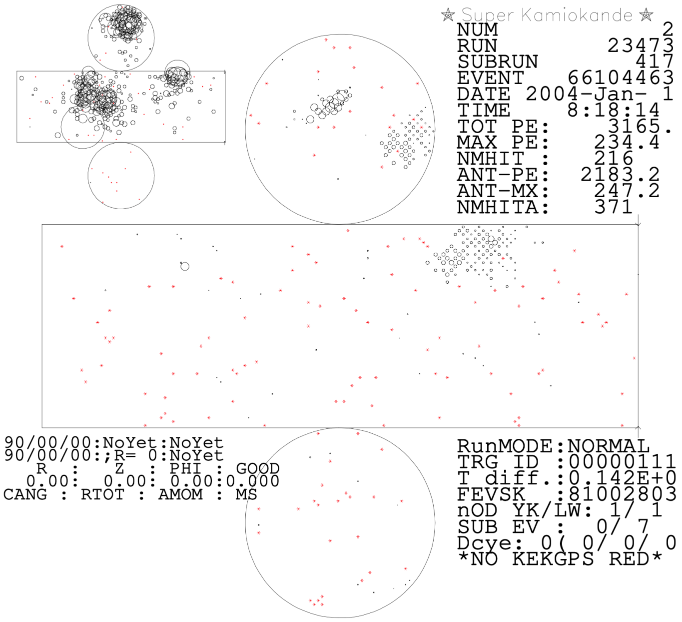

Figure 6.6: Typical event display of coincidence muon events.

- Low energy event cut

  The remaining low-energy backgrounds are rejected if the events satisfy the following criteria.

  - The number of ID hits is less than 500
  - $N_{50} \leq 50$ (25 for SK-II),

    N_{50} is the maximum number of ID PMT hits in a sliding 50 ns window after subtracting the photon time-of-flight. The threshold of these cuts corresponds to roughly 10 MeV for an electron, which is sufficiently lower than the energy expected from proton decay.

The event rate in SK is reduced to about 50 events/day by these cuts.

6.4 Fourth reduction

The fourth reduction is performed to remove flasher events that could not be removed by the third reduction. Since flasher events often have similar hit patterns (Figure 6.7), the remaining events are compared with the other events. The ID is divided into 1450 regions of 2 m×2 m squares, and the correlation r between events is evaluated using the following equation.

$$r = \frac{1}{N} \sum_{i=0}^{N} \frac{(Q_{A,i} - \langle Q_A \rangle)(Q_{B,i} - \langle Q_B \rangle)}{\sigma_A \sigma_B}, \tag{6.1}$$

where $Q_{A,i}(Q_{B,i})$ is the number of p.e.'s of event A (B), $\langle Q_A \rangle$ ($\langle Q_B \rangle$) is the mean of them, and σ_A (σ_B) is the standard deviation. If the correlation between two events exceeds a threshold, the

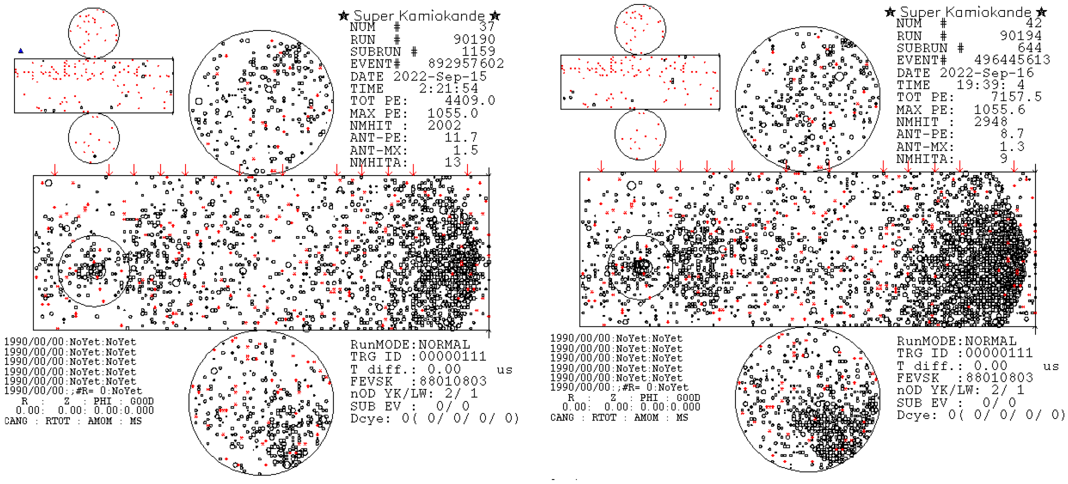

Figure 6.7: Typical event displays of flasher events. The same ID PMT causes the flasher events.

hit patterns are determined to be similar. The Kolmogorov-Smirnov test statistic dks is also used for the reduction. It is performed for the accumulated charge distribution normalized by the total observed charge. The cut parameter of the fourth reduction is introduced by the likelihood method. The likelihood value is calculated from probability density functions for these two parameters using the atmospheric neutrino simulation.

$$\begin{aligned}
\mathrm{Prob} &= \frac{1}{2}(\mathrm{Prob_r} + \mathrm{Prob_{dks}}), && (6.2)\\
\mathrm{Prob_r} &= \frac{1}{10}\left(-2\sum_{i}^{\text{top }10} \ln Pr(r_i, Q_i) + 2\sum_{i=1}^{10} \ln\left[\frac{i}{N^{\alpha}}\right]\right) + C_r, && (6.3)\\
\mathrm{Prob_{dks}} &= \frac{1}{10}\left(-2\sum_{i}^{\text{top }10} \ln Pr(dks_i, Q_i) + 2\sum_{i=1}^{10} \ln\left[\frac{i}{N^{\beta}}\right]\right) + C_{dks}, && (6.4)
\end{aligned}$$

where Pr is a probability function, Q_i is the average total charge of two compared events, N is the number of compared events, and α, β, C_r and C_{dks} are tuning parameters with the values of 0.909, 0.674, -0.31 and -3.39, respectively. Only 10 combinations with the largest correlations are used for the likelihood calculation. Events with a likelihood value of more than 3.0 are rejected.

6.5 Fifth reduction

The remaining backgrounds are rejected by the fifth reduction.

- Stopping muon cut

  Events satisfying either of the following conditions are rejected as remaining stopping muon events.

  - Stopping muon fit goodness ≥ 0.5 and $\mathrm{NHITA_{in800}} \geq 5$

  - $\mathrm{NHITA}_{\mathrm{in200}} \geq 5$

    $\mathrm{NHITA}_{\mathrm{in200}}$ is the maximum number of OD hits located within 8 m from the entering point and in a sliding 200 ns time window.

  - The vertex reconstruction goodness is below 0.77, the number of ID hits is more than 7000 with more than 70000 p.e.s deposited therein, and $\mathrm{NHITA}_{\mathrm{in800}} \geq 6$

  The second criterion rejects events with the OD PMT hits localized in terms of time and location. The third criterion rejects high-energy cosmic-ray muons which are incorrectly reconstructed in the fiducial mass region by the event reconstruction algorithm.

- Cable hole muon cut

  Events satisfying the following conditions are rejected as the events near the cable hole without signals from VETO counters.

  - Stopping muon fit goodness ≥ 0.4
  - $\mathrm{PE}_{\mathrm{tot}} > 4000$ p.e.'s
  - $\cos\theta_z > 0.6$

    $\cos\theta_z$ is the reconstructed muon direction, and $\cos\theta_z = 1$ is vertically downward-going.

  - $d_{\mathrm{hole}} < 250$ cm

    where d_{hole} is the distance between the reconstructed entering point and the closest cable hole position.

- Coincidence muon cut

  Events satisfying the following criteria are rejected as accidental coincidence of muon and other events:

  - $\mathrm{PE}_{500} < 300$ p.e.'s

    PE_{500} is the total number of p.e.s in a fixed 500 ns time window from -200 ns to $+300$ ns after the trigger.

  - $\mathrm{NHITA}_{\mathrm{LATE200}} \geq 16$

    $\mathrm{NHITA}_{\mathrm{LATE200}}$ is the maximum number of the OD hits in a 200 ns sliding time window from $+300$ ns to $+1500$ ns after the trigger.

- Invisible muon cut

  Invisible muons are cosmic ray muons that have momentum below the Cherenkov threshold in the ID. They reach the inner water tank and decay into electrons after 2.2 μs on average. Cherenkov light emitted from Michel electron is observed in the ID, while the OD PMT hits are produced earlier than the ID trigger timing. Therefore, the ID hits from Michel electron are misidentified as an FC event. These events are rejected by requiring either of the following conditions to identify the visible muons:

  - $\mathrm{PE_{tot}} \leq 1000$ p.e.s (500 p.e.s for SK-II) and $\mathrm{NHITA_{early200}} \geq 5$ and $\mathrm{NHITA_{sum}} \geq 10$.

    $\mathrm{NHITA_{early200}}$ is the maximum number of OD hits in a sliding 200 ns time window from −9000 ns to −200 ns after the trigger. $\mathrm{NHITA_{sum}}$ is defined as

    $$\mathrm{NHITA_{sum}} = \begin{cases} \mathrm{NHITA_{early200}} + \mathrm{NHITA_{500}} & (d_{\mathrm{OD}} < 500\,\mathrm{cm}) \\ \mathrm{NHITA_{early200}} & (\text{otherwise}) \end{cases} \tag{6.5}$$

    where $\mathrm{NHITA_{500}}$ is the number of OD hits in a fixed 500 ns time window from −200 ns to +300 ns after the trigger, and d_{OD} is the distance between the position of the OD PMT hit cluster in $\mathrm{NHITA_{early200}}$ and the position of the OD PMT hit cluster in $\mathrm{NHITA_{500}}$.

  - $\mathrm{NHITA_{early200}} \geq 55$

- Long tail flasher cut.

  The vertex position of the charged particle is reconstructed by the hit pattern of PMTs assuming the light is emitted from a certain point in the ID (Point-fit). While the goodness of the Point-fit tends to be small for flasher events due to broad timing distribution by the discharge of the PMT. The remaining flasher events are rejected using this characteristic. Events satisfying one of the following conditions are rejected.

  - Point-fit goodness < 0.3
  - Point-fit goodness < 0.4 and $\mathrm{NHIT_{min100}} \geq 6$

The event rate in SK is reduced to about 30 events/day by these cuts.

6.6 Final fully contained dataset

After the data reduction, quality cuts are applied to select events for the proton decay search: the events should be fully contained (FC) with the vertex position in the fiducial volume (FV) defined as a region more than 2 m away from the ID wall as shown in Figure 6.8 (FCFV selection). The fully contained events are selected by the condition that the number of hit PMTs in the largest OD hit cluster should be less than 16 hits. In addition, we require that the total visible energy (electron equivalent total energy deposit in the detector) should be greater than 30 MeV (E_{vis} selection). Events away from the ID wall are selected as the analysis sample because events close to the ID wall have fewer hit PMTs, resulting in the degradation of the event reconstruction performance. Also, these events often contain flasher events and radioactive backgrounds from the wall that could not be removed by the reduction. Figure 6.9 shows the distribution of the vertex position of the data

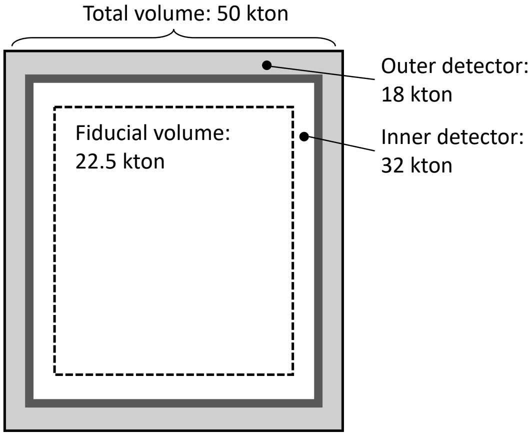

Figure 6.8: Schematic diagram of the ID, OD, and fiducial volume in SK.

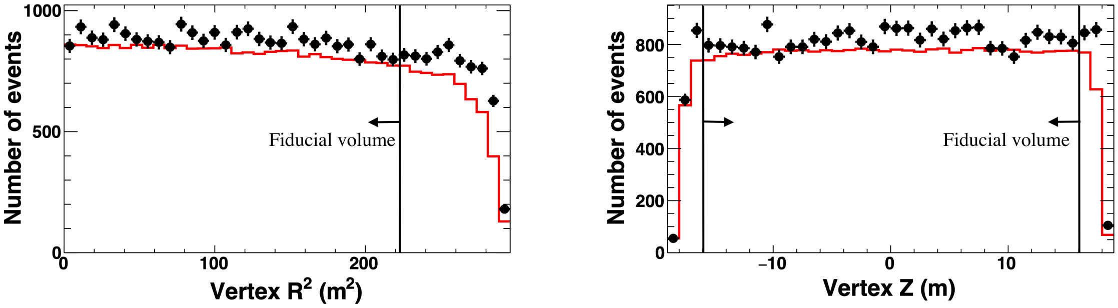

Figure 6.9: Distributions of the radial (left) and central axial (right) positions (R and Z) of the data after the fifth reduction in SK-IV. The FC and E_{vis} selection are applied for the data (black) and atmospheric neutrino simulation (red). For the R^2 (Z) distribution, events are rejected if the distance from the ID wall along the Z (R) direction is within 2 m. The atmospheric neutrino simulation is normalized by the live time.

after the FCFV selection in SK-IV. The energy and positions are reconstructed from the observed PMT signals by the fiTQun algorithm as explained in Chapter 7. In the FV region, the positions are uniformly distributed as expected from the atmospheric neutrino events, and the background contamination from the events near the ID wall is rejected. After the all FC reduction, the event rate is about 10 event/day. Signal efficiency after FCFV selection is estimated to be 97% from the simulation. In the recent $p \to e^+ + \pi^0$ and $p \to \mu^+ + \pi^0$ searches [8], an enlarged fiducial volume cut (vertex more than 1 m away from the ID wall) was used for the proton decay search. It was not employed in this analysis because the K_L^0 decays a few meters away from the point of the proton decay as discussed in Section 4.1, and the K_L^0 decay point could be close to the ID wall or outside the ID if the proton decays within 2 m of the ID wall.

Chapter 7

Event reconstruction

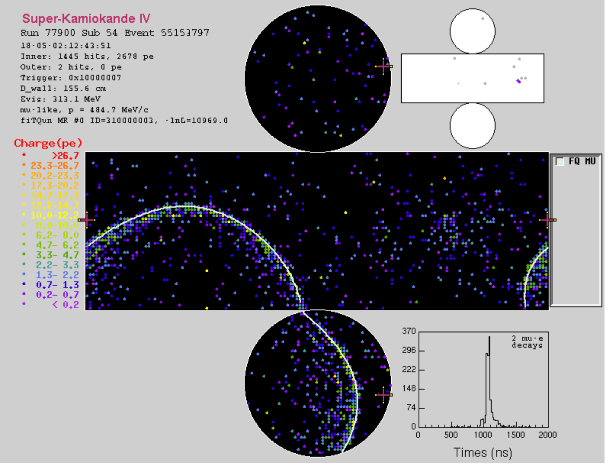

Figure 7.1: Event display of a typical neutrino event candidate. The solid line shows the reconstructed Cherenkov ring.

7.1 Reconstruction algorithm

Figure 7.1 shows an event display of a typical neutrino event candidate selected by the FC reduction. As explained in Section 3.1, hit patterns of PMTs are different for particle properties. The event reconstruction algorithm estimates basic event properties such as vertex (generated position), direction, particle type and momentum based on the PMT hit information. As an example, the event shown in Figure 7.1 was reconstructed as a muon with 484.7 MeV/c momentum. In the previously published SK-I to SK-III search [1], these properties are reconstructed by several steps (APFit algorithm). For example, the vertex position is reconstructed first by the timing information. Then, the number of rings, the particle type and momentum are reconstructed from the observed photoelectrons (p.e.'s) and the pattern of PMT hits in separate steps. In this study, the improved event reconstruction algorithm fiTQun [68] is used. It is based on the maximum likelihood method for both hit PMTs and unhit PMTs (PMTs with no signal). The vertex, momentum and particle type of the ring are simultaneously determined from the time and hit information based on several hit patterns created from the prior simulations. The performance of reconstruction is significantly improved with fiTQun [69].

7.1.1 Likelihood function

The event reconstruction maximizes the following likelihood function to determine the parameters.

$$L(\mathbf{x}) = \prod_{j}^{\text{unhit}} P_j(\text{unhit}|\mathbf{x}) \prod_{i}^{\text{hit}} (1 - P_i(\text{unhit}|\mathbf{x})) f_q(q_i|\mathbf{x}) f_t(t_i|\mathbf{x}), \tag{7.1}$$

where x is a set of reconstruction parameters (three parameters for vertex position, one parameter for time, two parameters for zenith angle and azimuth angle, and one parameter for the absolute value of the momentum). $P_j(\text{unhit}|x)$ is an unhit probability for each PMTs. $f_q(q_i|x)$ and $f_t(q_i|x)$ are the probability density function of the observed number of p.e.'s and time, respectively.

$P_j(\text{unhit}|x)$ is evaluated based on the predicted number of p.e.'s μ at parameter x. Since the observed number of p.e.'s should follow a Poisson distribution with the predicted number of p.e.'s μ, the unhit probability $P_j(\text{unhit}|x)$ follows $\exp(-\mu)$. In addition, the probability is corrected up to the third order to take into account the inefficiency due to the threshold of each PMT:

$$P_j(\text{unhit}|x) = (1 + a_1\mu + a_2\mu^2 + a_3\mu^3) \exp(-\mu). \tag{7.2}$$

The coefficients (a_1, a_2, a_3) are determined from the detector simulation.

The predicted number of p.e.'s for each PMT μ_i is estimated from the sum of expectations from the direct light μ_i^{dir}, indirect light μ_i^{sct} (which arrives PMT photocathode after scattering or reflection) and dark rate μ^{dark}. The dark rate is due to the PMT noise and the average rate for each PMT was evaluated as 5.7195 kHz for SK-IV based on the measurements and implemented in the simulation.

The prediction by the direct light from Cherenkov light emission is given as an integral along the particle track length s:

$$\mu_i^{\text{dir}} = \Phi(p) \int ds g(p, s, \cos\theta) \Omega(R) T(R) \epsilon(\eta), \tag{7.3}$$

where $\Phi(p)$ is a normalization factor proportional to the average total number of photons as a function of initial momentum p. $g(p, s, \cos\theta)$ is the distribution function of the number of emitted photons which depends on the momentum p, track length s and angle to PMT θ. $\Omega(R)$, $T(R)$ and $\epsilon(\eta)$ are correction factors which depends on the distance to PMT R and the angle from PMT η. Each factor will be explained below. Figure 7.2 shows the geometrical relations between the particle and PMT.

$g(p, s, \cos\theta)$ is called Cherenkov emission profile and normalized as

$$\int g(p, s, \cos\theta) ds d\Omega = 1, \tag{7.4}$$

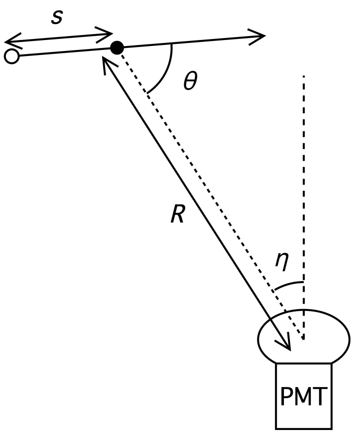

Figure 7.2: Schematic diagram describing the variables relevant to calculate the predicted number of p.e.'s. The white dot is the initial position of the particle. Taken from [71].

where Ω represents a solid angle. Figure 7.3 shows examples of the Cherenkov emission profile for electrons. $\Omega(R)$ is the correction factor of the PMT solid angle at a distance of R. The correction to a circle of radius $a = 25.4\,\mathrm{cm}$ (the radius of the PMT) from a location R away is assumed:

$$\Omega(R) = \frac{\pi a^2}{R^2}. \tag{7.5}$$

$T(R)$ is the attenuation factor of direct light due to absorption and scattering in water:

$$T(R) = \exp(-R/L), \tag{7.6}$$

where L is the wavelength averaged attenuation length 7496.46 cm obtained from the detector simulation with the absorption parameters determined by the calibration (Section 3.7). $\epsilon(\eta)$ is the PMT angular acceptance obtained from the detector simulation (Figure 7.4).

The indirect light includes the light scattered in water and the reflected light coming from detector components such as the black sheet and surface of PMTs. The prediction of the indirect light is similar to the one of the direct light:

$$\mu_i^{\mathrm{sct}} = \Phi(p) \int ds \frac{\rho(p,s)}{4\pi} \Omega(R) T(R) \epsilon(\eta) A(s), \tag{7.7}$$

where $\rho(p,s)$ is the integral of the Cherenkov emission profile to the solid angle:

$$\rho(p,s) = \int g(p,s,\cos\theta) d\Omega. \tag{7.8}$$

$A(s)$ is a correction table for the contribution of scattered light obtained from the detector simulation with the scattering and absorption parameters determined by the calibration (Section 3.7).

7.1.2 Vertex pre-fitter

As the first step of the event reconstruction algorithm, the generated position of the charged particles is roughly determined by the vertex pre-fitter. The vertex pre-fitter is performed to start optimizing

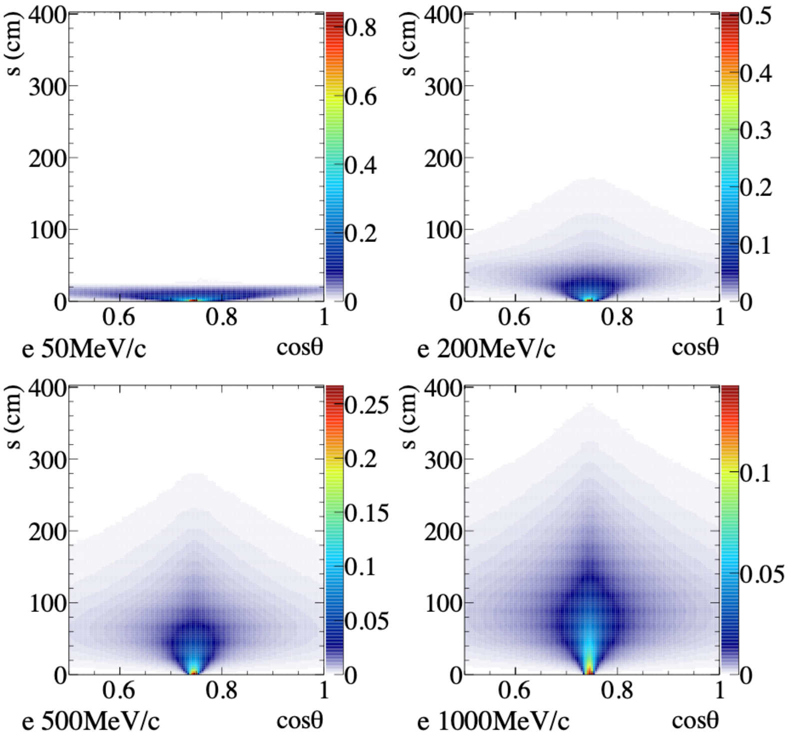

Figure 7.3: Cherenkov emission profile for electrons at different initial momentum. Horizontal axes represent the cosine of the angle from the particle direction, and vertical axes are the distance traveled from the initial position of the particle. Taken from [71].

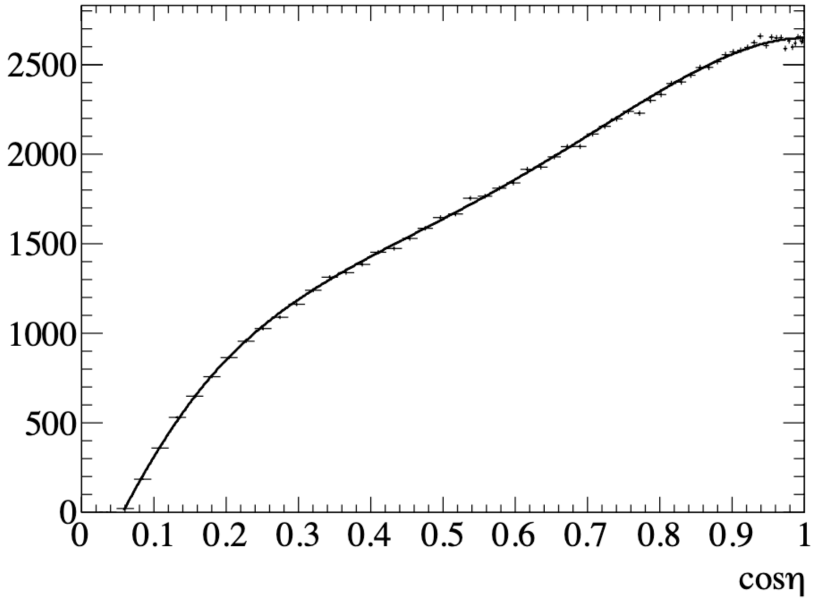

Figure 7.4: Angular acceptance of the PMT plotted as a function of $\cos \eta$ which is obtained from detector simulation with the reflection indices of water and PMT surface. A fitted curve is overlaid with a solid line. Taken from [71]. The vertical axis is shown in an arbitrary unit.

parameters from nearby the global minimum and avoid converging at a local minimum. Assuming a point light source, the following likelihood function is used for the estimation.

$$G(x,t) = \sum_{i}^{\text{hit PMTs}} \exp\left[-\left(\frac{T^i_{\text{res}}}{\sqrt{2}\sigma}\right)^2\right], \tag{7.9}$$

where

$$T^i_{\text{res}} = t_i - t - \frac{|R^i_{\text{PMT}} - x|}{c/n}. \tag{7.10}$$

Here, x and t are the position and time of the vertex to fit, σ is a hyperparameter of the fit, t_i is a hit timing of each PMT, and c/n is the light velocity in water. T^i_{res} indicates the residual hit time of the i-th PMT. T^i_{res} becomes smaller when x and t approach the true value, and $G(x,t)$ decreases with T^i_{res}. The pre-fitter is applied to the hits around the trigger (-100, $+400$ ns). The grid size and σ in the $G(x,t)$ are gradually shrunk, and the grid search in space and time is iteratively performed.

7.1.3 Hit clustering

If there are multiple hit clusters by the secondary reactions such as Michel electrons from muon decay in the same time window, they are counted as subevents and separated by the hit clustering algorithm.

First, the goodness, a return value of Equation 7.9, is evaluated for each 8 ns time window from -200 ns to 15,000 ns around the trigger with $\sigma = 6.3$ ns and fixed vertex given by the pre-fitter. After finding the subevent candidate, the time window is set around the peak [-180 ns, $+800$ ns]. Finally, the vertex pre-fitter and the peak search are conducted again for a precise peak finding. The final time windows are fixed for each peak, and the maximum likelihood is calculated for each of them. Figure 7.5 shows the goodness distribution as a function of time as an example of hit clustering.

7.1.4 Single-ring fitter

After the hit clustering, the single-ring fitter is applied to each subevent. The negative log-likelihood function (Equation 7.1) is minimized to obtain the optimal parameters such as vertex position and momentum for the assumed particles e, μ, and π^+ which reproduce the observed PMT signals in the detector. MINUIT [70] package is used to minimize the negative log-likelihood in the multiple parameter space.

7.1.5 Multi-ring fitter

More than one charged particle can be generated from proton decay and each makes a Cherenkov ring. Figure 7.6 shows an example of such an event. Multi-ring fitter is an algorithm to find such multiple Cherenkov rings. It is applied to only the first subevent because multiple Cherenkov rings are expected for the first subevent, while the secondary particles are generated one by one at

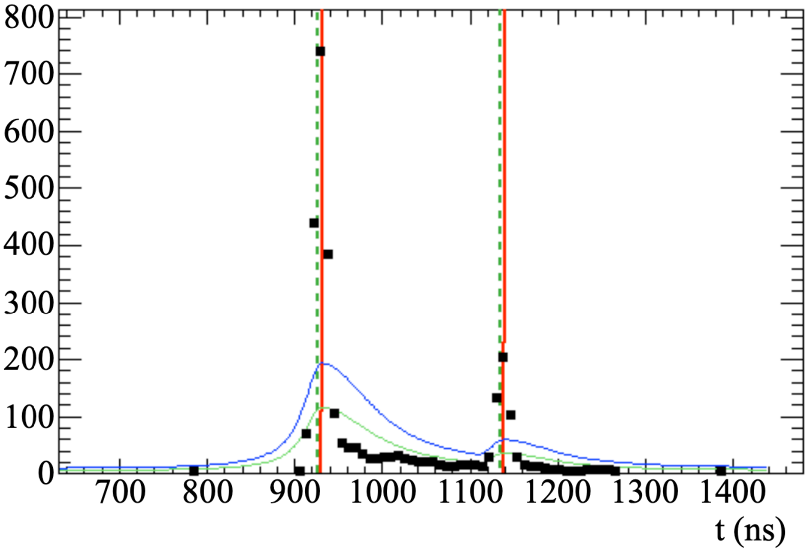

Figure 7.5: Distribution of the goodness as a function of time for an example event with a parent muon and a Michel electron. The vertical dashed lines indicate the true generation time of the particles in the simulation, the black points are the scanned goodness points, and the blue and green curves represent the threshold curves used for the subevent peak search. The red vertical lines show the time of the subevent peaks found by the algorithm. Taken from [71].

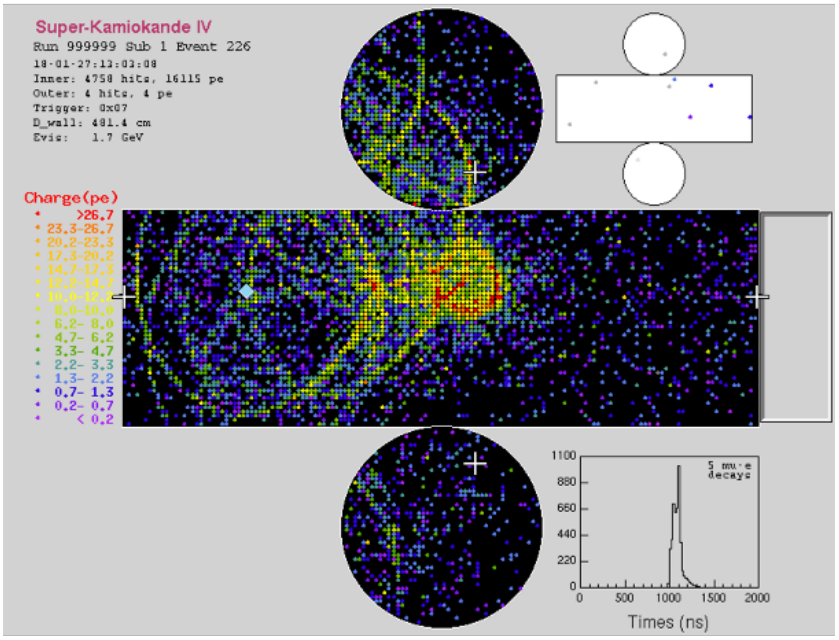

Figure 7.6: Typical event display of multi-ring events.

different timing and the subsequent subevents appear as single-ring events, such as Michel electron events. The algorithm searches the rings by sequentially increasing the number of rings as shown in Figure 7.7. The expected PMT hits of the single rings are added to the prediction and the negative log-likelihood is evaluated in comparison with the observed PMT signals.

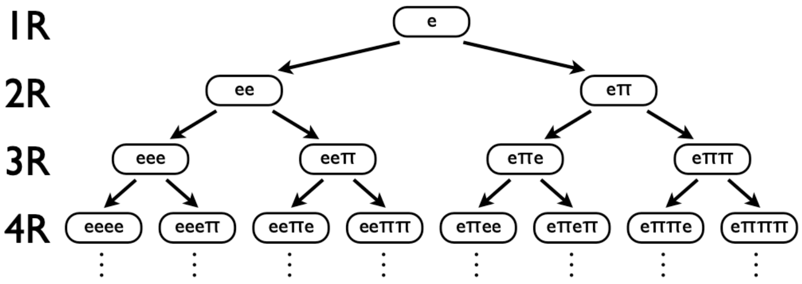

Figure 7.7: A tree diagram showing how the algorithm evolves the tree of the multi-ring hypotheses for the increased number of rings. The diagram is for the case assuming the first ring is an electron, and the equivalent procedure is developed for the case assuming π^+ (which is equivalent to the μ hypothesis) as the first ring. Taken from [71].

Additional rings are identified by the following procedure. First, the algorithm searches the direction of the additional ring assuming an electron with 50 MeV/c momentum from the same vertex as the first ring. Second, the momentum of the additional ring is adjusted to reproduce the observed PMT signals while all the other parameters are fixed. Third, the direction and the momentum of the additional ring are simultaneously optimized, while the vertex is fixed to be the same as the first ring, and the direction and the momentum of the original rings are fixed. Fourth, the momenta of all rings are fitted simultaneously while the vertex and their directions are fixed. Finally, the directions and momenta of all rings are simultaneously fitted to get the final best-fit result. This procedure is repeated until the sixth ring. To save the computation time, the simultaneous fit of all parameters (final step) is performed only for the two-ring case. The best fit hypothesis for the number of rings and the combination of particle types is determined by choosing the smallest negative log-likelihood.

After that, the best fit hypothesis with the optimized parameters is corrected because it often contains misidentified rings (fake rings). The angles between the directions of the most energetic ring and the other rings are calculated, and the lower energy ring is merged with the highest energy ring by adding the energy if the angle is below 20°. After that, all ring parameters are fitted again assuming three particle types: e, μ and π^+. In this step, all vertices of the rings are fitted independently.

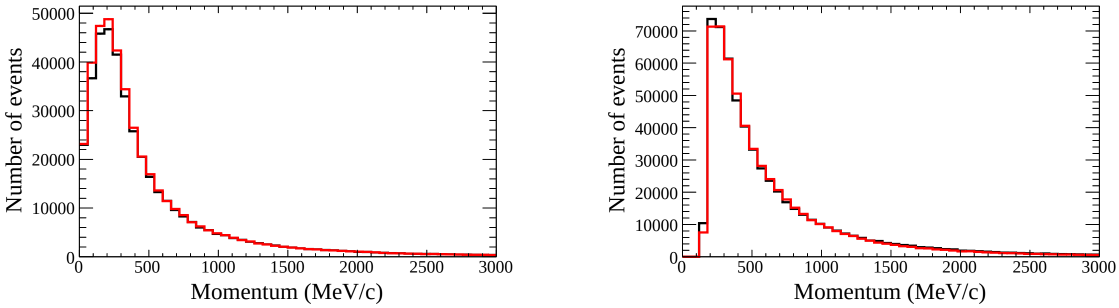

Figure 7.8: Reconstructed momentum distributions in APFit (black) and fiTQun (red) for FCFV single-ring events. The left (right) plot shows the e-like (μ-like) events for the $\nu_e, \bar{\nu}_e$ ($\nu_\mu, \bar{\nu}_\mu$) CCQE sample.

7.2 Performance of fiTQun

Figure 7.8 shows the reconstructed momentum distributions in APFit (the algorithm used in the previous search in SK) and fiTQun for FCFV (fully contained fiducial volume, as defined in Section 6.6) single-ring events of the atmospheric neutrino simulation. Only charged current quasi-elastic scattering (CCQE) sample is used for the distributions in which one charged lepton (e of μ) is generated and most of them are expected as single-ring events. For some true lepton momentum regions (200–400 MeV/c, 400–600 MeV/c and 600–1000 MeV/c), the momentum resolution (relative error between the true and reconstructed momentum) is evaluated as shown in Figure 7.9. Two-sided 68% intervals are calculated from them and summarized in Figure 7.10 as the momentum resolution for each true lepton momentum. For e-like rings, the momentum resolution is clearly improved with fiTQun in all momentum regions. For μ-like rings, the momentum resolutions of both algorithms are comparable but slightly improved with fiTQun in the 600–1000 MeV/c region.

Similarly, the vertex resolution (distance between true and reconstructed vertex) is evaluated as shown in Figure 7.9 and 7.10. For both e-like and μ-like rings, the vertex resolution is clearly improved with fiTQun in all momentum regions. As well as the momentum resolution, the improvement of the performance is clearer in the e-like rings compared to the μ-like rings.

π^0 meson decays into two γ's with short lifetime (8.5×10^{-2} fs). Therefore π^0 production events can be used to evaluate the performance of reconstruction for multi-ring events. The invariant mass of π^0 was also reconstructed in APFit and fiTQun as shown in Figure 7.13. The distributions consist of FCFV 2-ring e-like events for the neutral current single π^0 production (NC1π^0) sample in the atmospheric neutrino simulation. The means and width of the distributions are evaluated by Gaussian fits as $(137.2 \pm 0.1)\,\mathrm{MeV}/c^2$ and $(13.9 \pm 0.2)\,\mathrm{MeV}/c^2$ for APFit and $(135.9 \pm 0.1)\,\mathrm{MeV}/c^2$ and $(13.5 \pm 0.1)\,\mathrm{MeV}/c^2$ for fiTQun, respectively. The width of the invariant mass distribution is slightly improved in fiTQun.

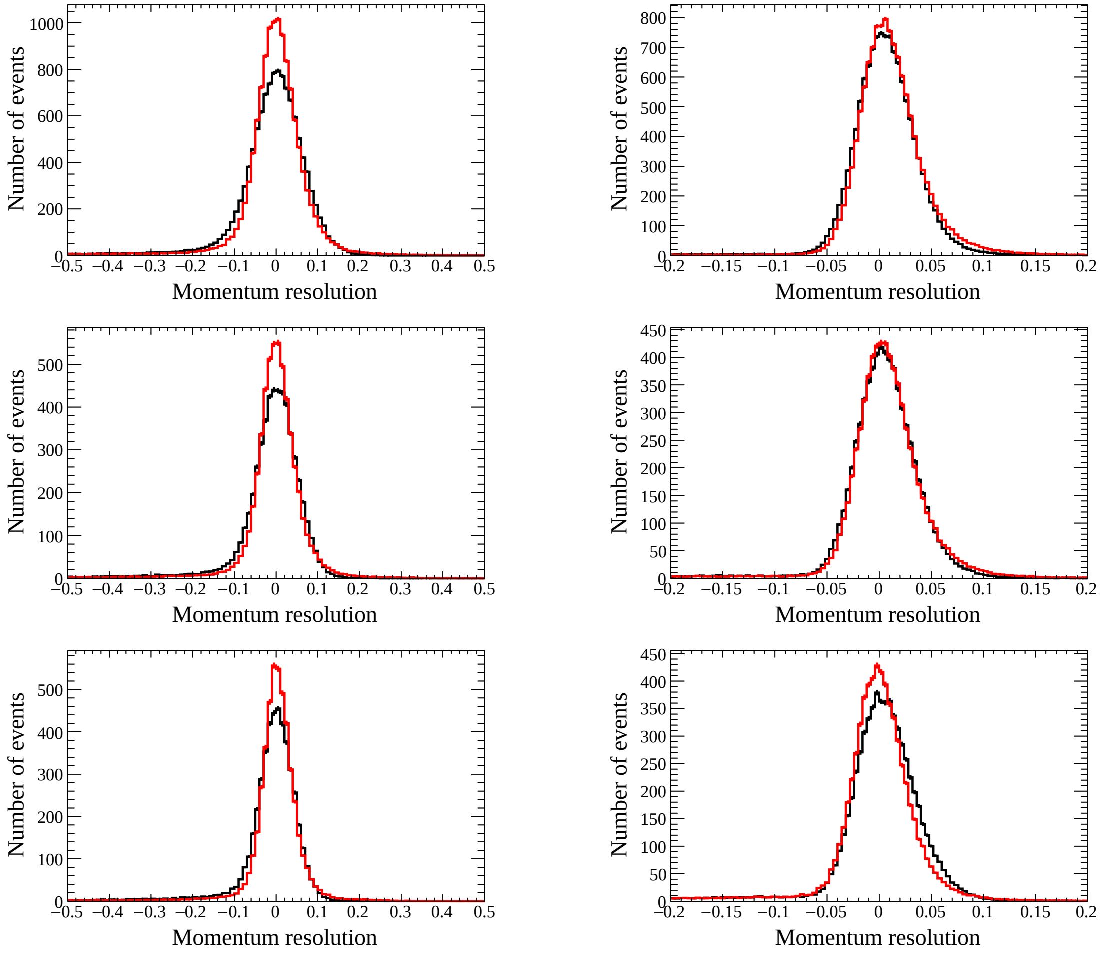

Figure 7.9: Relative error ((reconstructed − true)/true) of momentum in APFit (black) and fiTQun (red) for FCFV single-ring events. The left (right) plots show the e-like (μ-like) events for the $\nu_e, \bar{\nu}_e$ ($\nu_\mu, \bar{\nu}_\mu$) CCQE sample. The top, center and bottom plots are in the true $e^\pm$ or $\mu^\pm$ momentum regions of 200–400 MeV/c, 400–600 MeV/c and 600–1000 MeV/c, respectively.

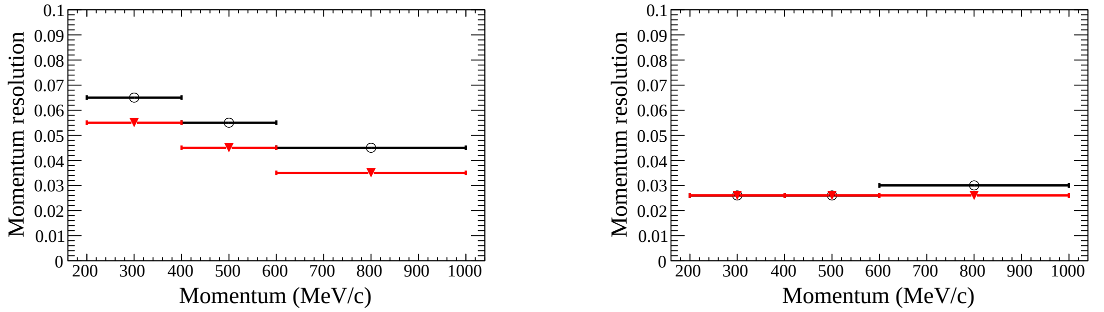

Figure 7.10: Summary of the momentum resolution in APFit (black) and fiTQun (red) for FCFV single-ring events. The left (right) plot shows the e-like (μ-like) events for the $\nu_e, \bar{\nu}_e$ ($\nu_\mu, \bar{\nu}_\mu$) CCQE sample.

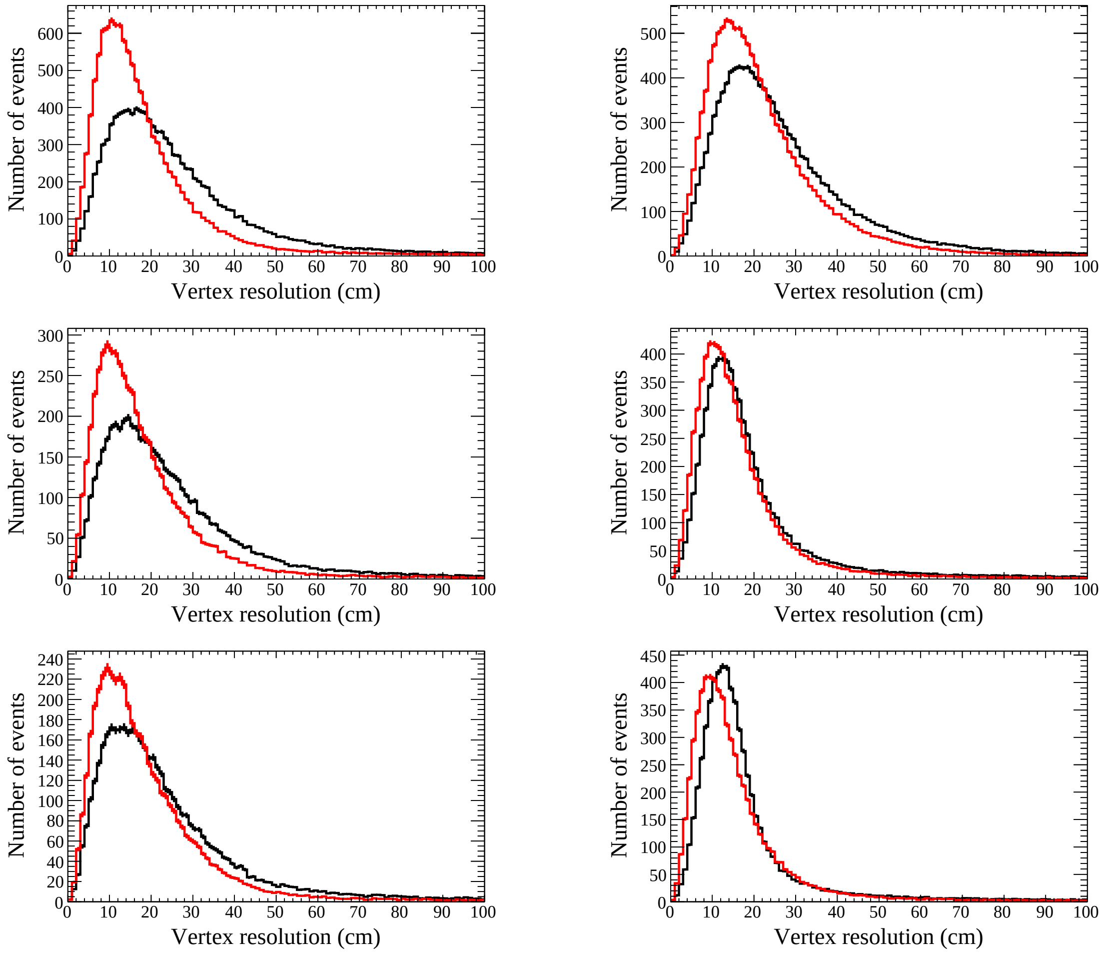

Figure 7.11: Distance between the true and reconstructed vertex in APFit (black) and fiTQun (red) for FCFV single-ring events. The left (right) plots show the e-like (μ-like) events for the $\nu_e, \bar{\nu}_e$ ($\nu_\mu, \bar{\nu}_\mu$) CCQE sample. The top, center and bottom plots are in the true $e^\pm$ or $\mu^\pm$ momentum regions of 200–400 MeV/c, 400–600 MeV/c and 600–1000 MeV/c, respectively.

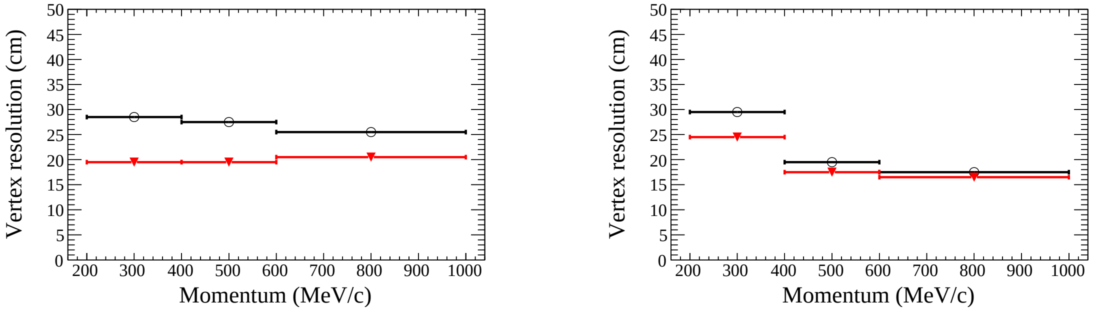

Figure 7.12: Summary of the vertex resolution in APFit (black) and fiTQun (red) for FCFV single-ring events. The left (right) plot shows the e-like (μ-like) events for the $\nu_e, \bar{\nu}_e$ ($\nu_\mu, \bar{\nu}_\mu$) CCQE sample.

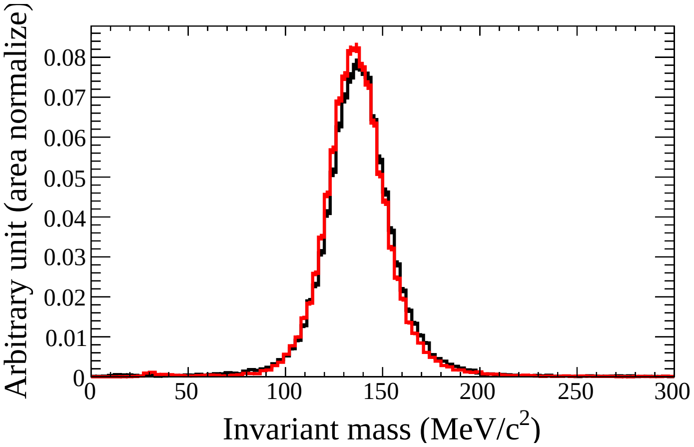

Figure 7.13: Reconstructed π^0 mass distributions of APFit (black) and fiTQun (red). Events are FCFV 2-ring e-like of the NC1π^0 sample in the atmospheric neutrino simulation.

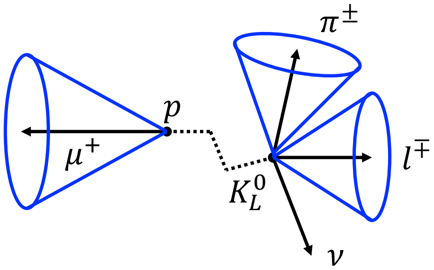

Figure 7.14: Schematic diagram of $p \to \mu^+ + K_L^0$, ($K_L^0 \to \pi^{\pm} + l^{\mp} + \nu$) channel.

7.3 Displaced vertex fiter

As explained in Section 4.1, a muon and a neutral kaon are produced at the same vertex from proton decay. Among these, the muon immediately emits Cherenkov light. Neutral kaon is a superposition of K_S^0 and K_L^0. K_S^0's decays at almost the same position as the proton decay. On the other hand, K_L^0's undergo hadronic interactions while propagating in the water, and decay about 1 m away with a lifetime of 51 ns. Figure 7.14 shows the schematic diagram of the process with K_L^0. In fiTQun, multiple rings are searched for assuming a single vertex in the initial step of the multi-ring fit. This leads to the degradation of the reconstruction performance for charged particles generated at the displaced vertex. For example, Figure 7.15 shows the comparison of the number of rings for $p \to \mu^+ + K_L^0$ events in the simulation with the nominal lifetime of 51 ns for K_L^0 decay (black) and the intentionally shortened lifetime of 90 ps for K_L^0 decay (red). Considering the fact that more than one particle is generated from $p \to \mu^+ + K_L^0$ and following K_L^0 decay, a fraction of single-ring events tells the misreconstruction of K_L^0 decay (as a muon creates clear ring which is reconstructed as the first ring for most events). A large fraction of single-ring events is reconstructed as multi-ring if the lifetime is shorter.

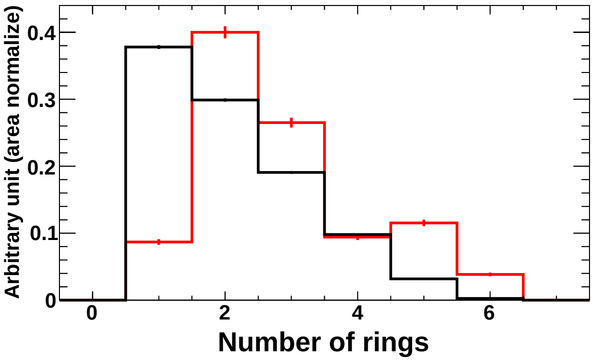

Figure 7.15: Number of rings reconstructed by fiTQun. $p \to \mu^+ + K_L^0$ simulation with nominal K_L lifetime (black) and K_L lifetime of 90 ps (red) are shown.

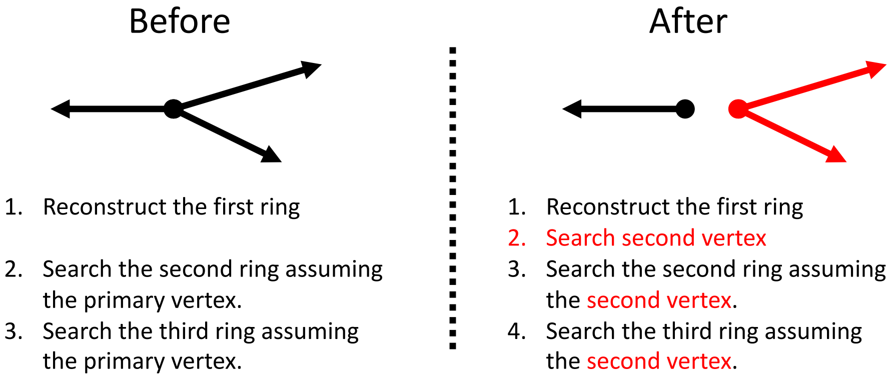

Before:

1. Reconstruct the first ring
2. Search the second ring assuming the primary vertex.
3. Search the third ring assuming the primary vertex.

After:

1. Reconstruct the first ring
2. Search second vertex
3. Search the second ring assuming the second vertex.
4. Search the third ring assuming the second vertex.

Figure 7.16: Schematic diagram of multi-ring reconstruction before and after the modification.

For this reason, the multi-ring reconstruction algorithm in fiTQun was modified for $p \to \mu^+ + K_L^0$ event selection to reconstruct a muon from proton decay and particles from K_L^0 decay. Hereafter, the modified algorithm is called "displaced vertex fitter".

Figure 7.16 shows the procedure of multi-ring reconstruction before and after the modification. After the first ring reconstruction, the hit PMTs which belong to the first ring are masked and the vertex pre-fit is performed again to search the secondary vertex using the remaining hits. Masked PMTs are not used for the calculation of the likelihood. Once the secondary vertex candidate is determined, PMTs are unmasked and the reconstruction is performed to find the third rings. The direction of the additional ring is searched in grid space assuming an electron with 50 MeV/c momentum generated at the second vertex determined in the previous step. After that, as well as the multi-ring fit, the parameters are fitted in steps with the independent second vertex. When fitting the subsequent rings, the search is performed assuming the same vertices as the second ring.

7.4 Performance of displaced vertex fitter

To check the performance of the displaced vertex fitter, it was applied to the simulation of $p \to \mu^+ + K_L^0(\to \pi^\pm + e^\mp + \nu)$ events with $\pi^\pm$ momentum below the Cherenkov threshold. These events should be identified as two rings for μ^+ and $e^\mp$ from the decay of K_L^0 because the $\pi^\pm$ does not emit the Cherenkov light. The number of ring distribution is shown in Figure 7.17. This plot shows higher efficiency to find the second ring by the displaced vertex fitter. Then, the performance of the vertex reconstruction is evaluated by the 2-ring sample as shown in Figure 7.18. It shows the distance between the true primary (secondary) vertex and the reconstructed primary (secondary) vertex. It was confirmed that the most of primary and secondary vertices are reconstructed within 50 cm of the true vertex with the displaced vertex fitter.

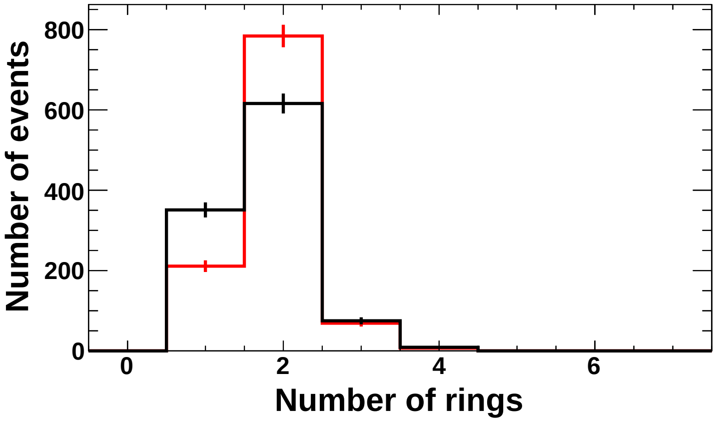

Figure 7.17: Number of rings reconstructed by original multi-ring fitter (black) and displaced vertex fitter (red) for $p \to \mu^+ K_L(\to \pi^\pm e^\mp \nu)$ simulation with the $\pi^\pm$ momentum below the Cherenkov threshold.

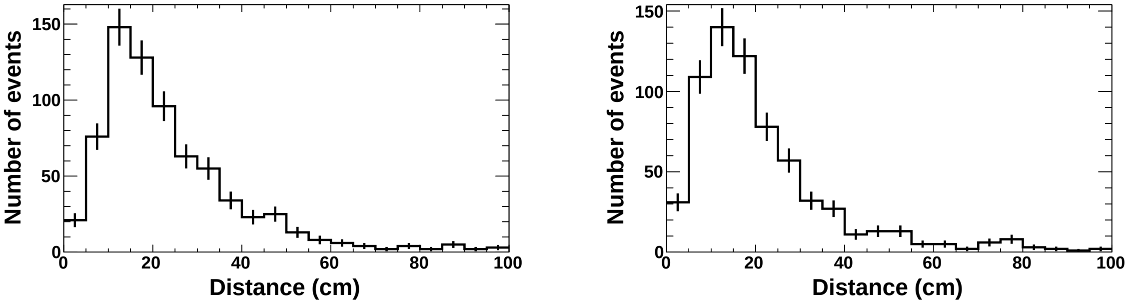

Figure 7.18: Left (right) shows the distance between the true primary (secondary) vertex and the reconstructed primary (secondary) vertex.

Decay electrons from muons are often reconstructed as the second vertex although these are not the target of the search for the kaon decay. To remove the contamination of decay electrons, rings belonging to the second vertex are discarded if the difference in the reconstructed times between the primary and secondary candidates is more than 100 ns.

7.5 Neutron tagging

Neutrons generated in water are captured by the surrounding hydrogen ($n+p \to d+\gamma$) after about 200 μs on average. Neutrons can be identified by detecting the 2.2 MeV γ emitted by this capture. Until SK-III running period, only the hits within 1.3 μs around the trigger were recorded, so the neutrons could not be identified. Since SK-IV running period, the electronics modules were updated to record all PMT hits from 35 μs to 535 μs after the primary trigger as described in Section 3.6. This enables the detection of neutron capture on hydrogen in that time window. The detection efficiency of neutrons is about 20% in the SK-IV period because the 2.2 MeV γ are easily buried by the dark hits of PMT and environmental radioactivity which mainly produces events below 4 MeV [30]. The signals from neutron captures by hydrogens are identified based on the algorithm of the neural network [72]. Despite the relatively low efficiency, the information on the number of detected (tagged) neutrons is useful to improve the sensitivity of proton decay searches.

Neutrons are often generated by atmospheric neutrino interactions and by the secondary interactions of the hadrons in water, especially at relatively high energy above the GeV scale, which are the main component of the background in the proton decay search. On the other hand, neutrons are generated with about 10% probability after proton decay in oxygen due to de-excitation of ^{15}N [73]. As a result, neutrino interactions tend to have tagged neutrons while it is not the case for proton decay. Therefore, the background events are suppressed by requiring no neutron in the proton decay search as written in the next section.

Chapter 8

Event selection

As proton decay is an extremely rare process, even if it happens, the signal events are overwhelmed by the atmospheric neutrino backgrounds. To further reduce atmospheric neutrino events after the data reduction as described in Chapter 6, selection criteria were determined based on the specifications. Selection criteria were fixed before they are applied to the data to avoid biases in the definition of the cuts and the threshold values. To suppress the statistical fluctuation of the remaining backgrounds, background events must be reduced to $\mathcal{O}(1)$ events or below with the tight cut. The detection efficiencies of proton decay events and the number of expected background events were estimated by applying the selection criteria to the proton decay simulation and atmospheric neutrino simulation.

8.1 Overview of selection

There are five selections to extract each K^0 decay mode in $p \rightarrow \mu^+ + K^0$ search.

A: $K_S^0 \rightarrow 2\pi^0$

B: $K_S^0 \rightarrow \pi^+ + \pi^-$

$$\text{C:} \begin{cases} K_L^0 \rightarrow \pi^{\pm} + l^{\mp} + \nu_l & \text{where } l \text{ is an electron or muon} \\ K_L^0 \rightarrow 3\pi^0 \\ K_L^0 \rightarrow \pi^+ + \pi^- + \pi^0 \end{cases}$$

Here, A, B and C are the labels of the selections. The three selections for K_L^0 are grouped as C and branch off in the middle of the selection criteria. The final samples of selection A (A and B) are excluded in selection B (C) to avoid double counting of events. Figure 8.1 shows the flow diagram of the event selection.

Figure 8.2 shows the event display of the proton decay simulation for $p \rightarrow \mu^+ + K^0$, $K_S^0 \rightarrow 2\pi^0$ (left) and $p \rightarrow \mu^+ + K^0$, $K_L^0 \rightarrow 3\pi^0$ (right). For both K_S^0 and K_L^0 decay modes, the existence of monoenergetic primary muon from proton decay is required in the selection. In the search for

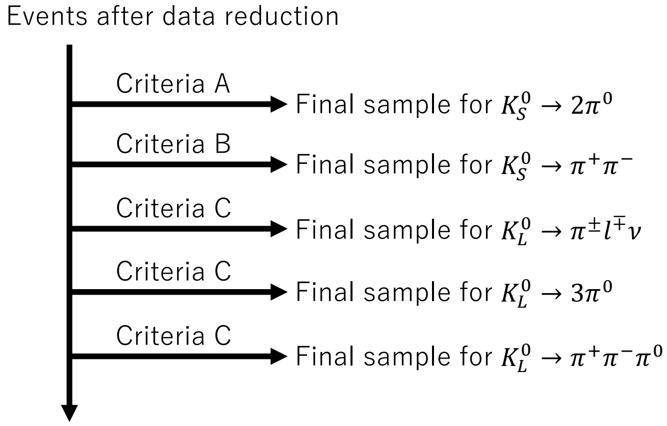

Figure 8.1: Flow diagram of the proton decay selection.

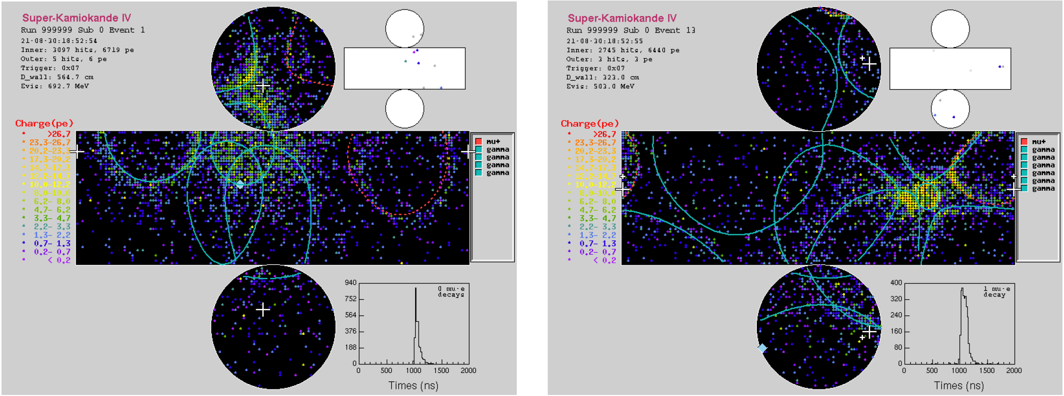

Figure 8.2: Event displays of the proton decay simulation for $p \to \mu^+ + K^0$, $K_S^0 \to 2\pi^0$ (left) and $p \to \mu^+ + K^0$, $K_L^0 \to 3\pi^0$ (right). The MC true rings of the muon (red) the γ's from π^0 decay (blue) and are also shown.

K_S^0 decay mode, background events are largely reduced by requiring the reconstructed invariant masses are consistent with kaon mass and proton mass. On the other hand, invariant mass is not reconstructed in the search of K_L^0 decay as some of the outgoing particles are invisible in the water Cherenkov detector. Therefore, instead of the invariant mass cut, the distance between the primary and secondary vertices is reconstructed by the displaced vertex fitter and used in the selection to suppress the background. Details of each selection are described in the following sections.

There are two major updates to the selection criteria from the previous $p \to \mu^+ + K^0$ search [1]. In the previous study, events with two and three Cherenkov rings were selected as candidates for the $K_S^0 \to \pi^+ + \pi^-$ decay mode, in which three charged particles (μ^+, π^+ and π^-) are generated. While only three-ring events are selected in this study, as the background rate in two-ring events is higher than the other selections and the sensitivity from the selection is not significant compared to the others. As the other update, three selection criteria are applied for each K_L^0 decay mode instead of a single selection for all K_L^0 decay used in the previous analysis.

8.2 Selection for $p \to \mu^+ + K_S^0$, $K_S^0 \to 2\pi^0$

The events which satisfy the following criteria (A-1 – A-9) are selected as candidates for $K_S^0 \to 2\pi^0$. Each π^0 decay into two γ's, so the primary muon and four γ's appear in this decay mode.

A-1: Events should pass FCFV and E_{vis} selection.

As explained in Section 6.6, we require that events are fully contained (FC) defined as there is no cluster of hit PMTs in the outer detector (OD), the vertex is in the fiducial volume (FV) defined as a region more than 2 m away from the inner detector (ID) wall, and the electron equivalent total energy deposit in the detector, E_{vis}, should be greater than 30 MeV. These cuts are applied to avoid the degradation of the event reconstruction performance and to reject remaining flasher events and radioactive backgrounds from the wall.

A-2: The number of rings should be three, four or five.

The top left plot in Figure 8.3 shows the number of rings after selection A-1 is applied. One muon from the primary proton decay and four γ's from the decay of two π^0's ($\pi^0 \to 2\pi^0$) appear in this decay channel. Two γ's from π^0 decay make overlapped showering rings, and they are often reconstructed as one ring with the energy close to the sum of two γ's. Or, if one of two γ's was small energy, it cannot be recognized as a ring but the effect on the reconstruction of the invariant mass is limited. For these reasons, events with three, four and five rings are kept as candidates for this decay channel.

A-3: There must be one non-showering ring.

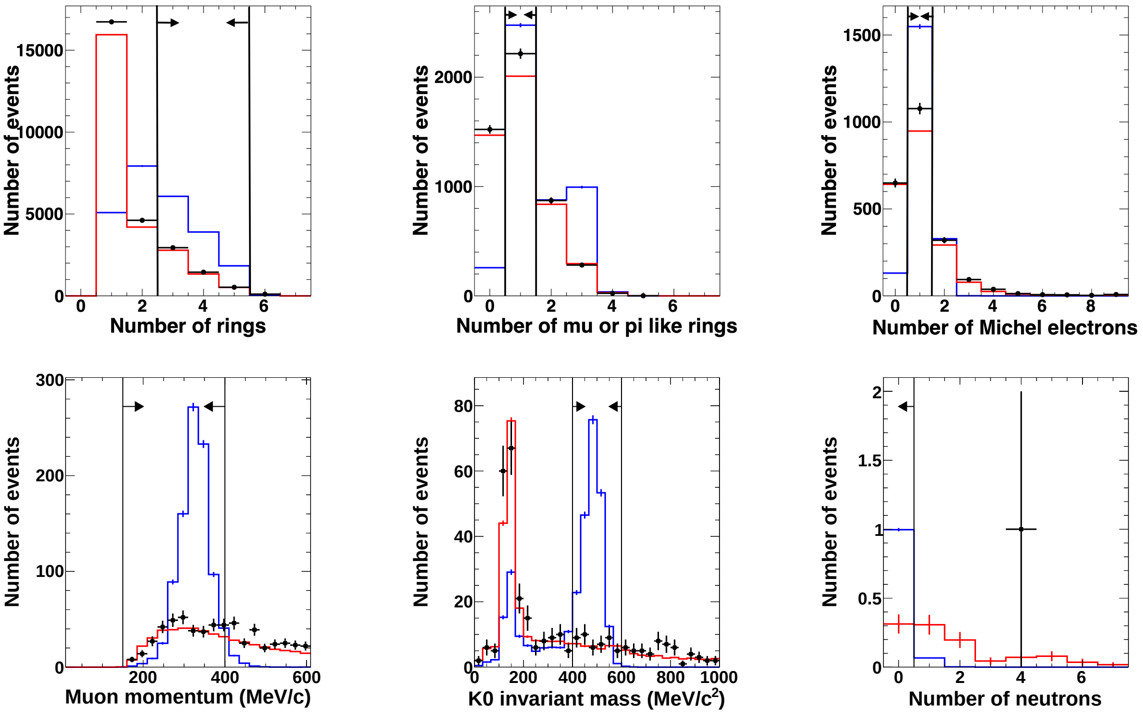

Figure 8.3: From top left to bottom right, reconstructed number of rings after selection A-1, number of non-showering rings after selection A-2, number of Michel electrons after selection A-3, muon momentum after selection A-4, kaon invariant mass after selection A-5, and number of tagged neutrons after selection A-8. The data (black dots) are compared with the atmospheric neutrino MC events (red) normalized by the live time, and the signal MC events (blue) normalized to the atmospheric neutrino MC events.

The non-showering ring is assumed to be due to the primary muon. The top center plot in Figure 8.3 shows the number of non-showering rings ($\mu^{\pm}$ or $\pi^{\pm}$ like) after selection A-2.

A-4: There must be one Michel electron.

The top right plot in Figure 8.3 shows the number of Michel electrons after selection A-3. This cut requires the existence of a Michel electron from the decay of the primary muon.

A-5: The reconstructed momentum of the non-showering ring should be $150 < P_{\mu} < 400\,\mathrm{MeV}/c$.

The bottom left plot in Figure 8.3 shows the momentum of the non-showering ring (muon) after selection A-4. Muon momentum from $p \to \mu^{+} + K^{0}$ decay is expected to peak at $326.5\,\mathrm{MeV}/c$ since it is two-body decay. It should be monochromatic momentum if proton decay occurs in hydrogen, while it slightly fluctuates if the proton decay occurs in oxygen nuclei due to the Fermi motion of protons.

A-6: The reconstructed invariant mass of the showering rings should be $400 < M_{K} < 600\,\mathrm{MeV}/c^{2}$.

The bottom center plot in Figure 8.3 shows the reconstructed invariant mass of the showering rings after selection A-5. γ's from π^{0} decay make showering rings, and the invariant mass of these rings is expected to be $497.6\,\mathrm{MeV}/c^{2}$, equivalent to K^{0} mass. This cut selects the events around the peak of K^{0} mass. A peak around $150\,\mathrm{MeV}/c^{2}$ in the invariant mass distribution is due to π^{0} either from atmospheric neutrino interactions (red) or from the decay of kaons from proton decay (blue).

A-7: The reconstructed total momentum should be $P_{\mathrm{tot}} < 300\,\mathrm{MeV}/c$.

A-8: The reconstructed total invariant mass should be $800 < M_{\mathrm{tot}} < 1050\,\mathrm{MeV}/c^{2}$.

Figure 8.4 shows scatter plots of the reconstructed total invariant mass and total momentum after applying all the cuts except those on the plotted variables (the neutron tagging cut, A-9, is also applied in this plot). The black box shows the region selected by both cuts A-7 and A-8. The total momentum and total invariant mass are reconstructed from all rings and therefore assumed to be the proton momentum and mass. In the proton decay simulation, the momentum of the proton in hydrogen is close to zero, and the invariant mass has a peak around $938\,\mathrm{MeV}/c^{2}$, equivalent to proton mass. In contrast, protons have Fermi momentum in oxygen nuclei, and the total momentum and invariant mass of the proton decay simulation have broad distribution. Free proton events in the signal MC simulation which appear around the top left corner of the box are due to secondary K_{S}^{0} decay generated by K_{L}^{0} scattering. As shown in the right-hand plot in Figure 8.4, no candidates remained in this sample.

A-9: There should be no tagged neutrons.

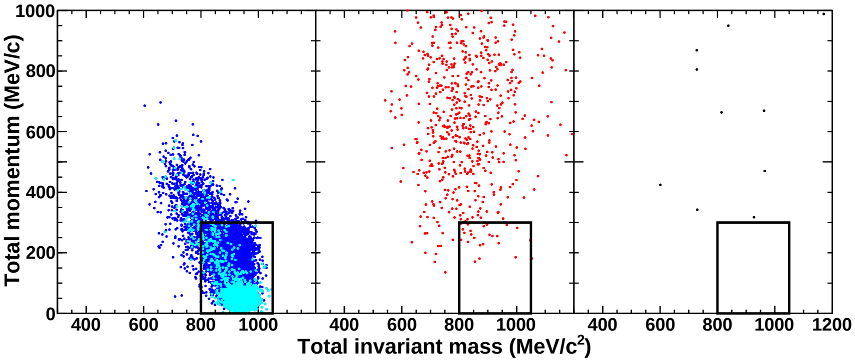

Figure 8.4: Scatter plot of the reconstructed total invariant mass and total momentum after applying all cuts in $K_S^0 \to 2\pi^0$ selection except those on the plotted variables. From left to right, signal MC events, atmospheric neutrino MC events (500 years-equivalent) and data (3244.39 live days) are shown. In the signal MC events, cyan shows free protons and blue shows bound protons.

The bottom right plot in Figure 8.3 shows the number of tagged neutrons after selection A-8. For this decay mode, 93% of the signal events have no neutrons, while background events tend to have tagged neutrons. A candidate event remaining after selection A-8 was rejected by requiring no tagged neutrons.

8.3 Selection for $p \to \mu^+ + K_S^0$, $K_S^0 \to \pi^+ + \pi^-$

Both π^+ and π^- make non-showering Cherenkov rings. As the momentum of these secondary muons from $\pi^\pm$ decay are below the Cherenkov threshold, they are not observed in the detector. In this selection, three non-showering rings are selected, and the most energetic ring is recognized as the muon from primary proton decay. The other rings are taken to be charged pions from K_S^0 decay. The events which satisfy the following criteria (B-1 – B-7) are selected as candidates for $K_S^0 \to \pi^+ + \pi^-$.

B-1: Events should pass FCFV and E_{vis} selection.

B-2: The number of rings should be three.

B-3: All rings should be non-showering.

The top left and top right plots in Figure 8.5 show the number of rings after selection B-1 and the number of non-showering rings after selection B-2, respectively. These rings are assumed to be due to a muon from proton decay and charged pions from K_S^0 decay.

B-4: The number of Michel electrons should be one or two.

The bottom left plot in Figure 8.5 shows the number of Michel electrons after selection B-3. π^+ generates a muon from the decay as $\pi^+ \to \mu^\nu_\mu$. On the other hand, π^- from K_S^0 decay

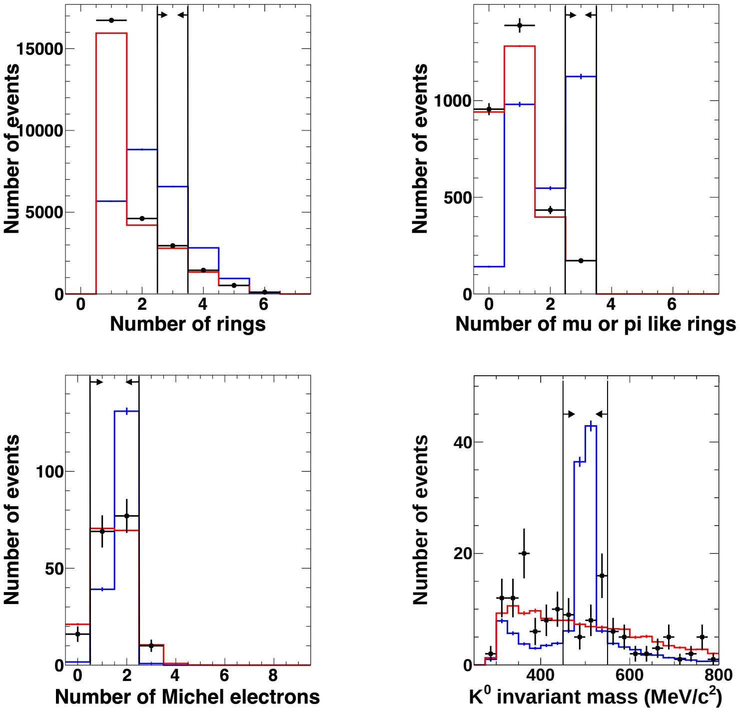

Figure 8.5: Reconstructed invariant mass distribution for kaons after selection B-4. Reconstructed number of rings after selection B-1, number of non-showering rings after selection B-2, number of Michel electrons after selection B-3, kaon invariant mass after selection B-4. The data (black dots) are compared with the atmospheric neutrino MC events (red) normalized by the live time, and the signal MC events (blue) normalized to the atmospheric neutrino MC events.

is often captured on a ^{16}O nucleus and does not generate a muon. Therefore, the number of tagged Michel electrons in the signal event is expected to be one or two, one from the primary muon and the other from π^+. Considering the inefficiency of Michel electrons, events with only one Michel electron are kept.

B-5: The reconstructed invariant mass of the second and third energetic non-showering rings should be $450 < M_K < 550\,\mathrm{MeV}/c^2$.

The bottom right plot in Figure 8.5 shows the reconstructed invariant mass of the second and third energetic non-showering rings after selection B-4. A peak at around $500\,\mathrm{MeV}/c^2$ corresponds to the K^0 mass ($497.6\,\mathrm{MeV}/c^2$). The lower edge of the kaon invariant mass distribution is due to the Cherenkov threshold of charged pions.

B-6: The reconstructed total momentum should be $P_{\mathrm{tot}} < 300\,\mathrm{MeV}/c$.

B-7: The reconstructed total invariant mass should be $800 < M_{\mathrm{tot}} < 1050\,\mathrm{MeV/c}^2$.

Figure 8.6 shows scatter plots of the reconstructed total invariant mass and total momentum after applying all cuts except those on the plotted variables. No candidates remained in this sample.

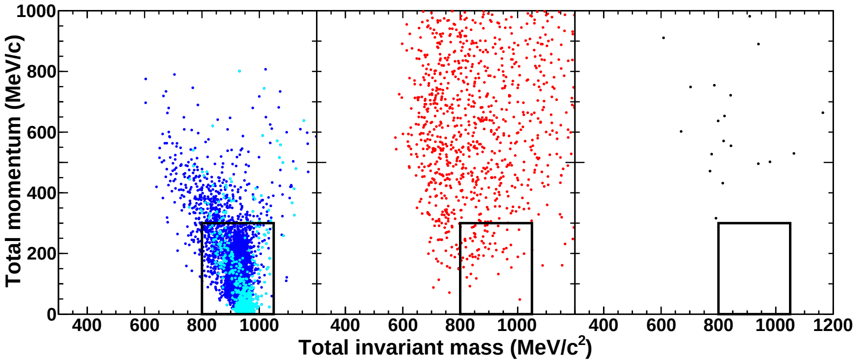

Figure 8.6: Scatter plot of the reconstructed total invariant mass and total momentum after applying all cuts in $K^0_S \to \pi^+\pi^-$ selection except those on the plotted variables. From left to right, signal MC events, atmospheric neutrino MC events (500 years-equivalent) and data (3244.39 live days) are shown. In signal MC events, cyan shows free protons and blue shows bound protons.

Criterion with the number of tagged neutrons is not applied because about 45% of signal events have tagged neutrons from pion capture.

8.4 Selections for $p \to \mu^+ + K^0_L$

There are three selection criteria for K^0_L decay, that is $K^0_L \to \pi^\pm + l^\mp + \nu$, $K^0_L \to 3\pi^0$ and $K^0_L \to \pi^+ + \pi^- + \pi^0$. l represents charged leptons either electron or muon. In the K^0_L decay selections (C), the primary non-showering ring is chosen as the primary muon from proton decay.

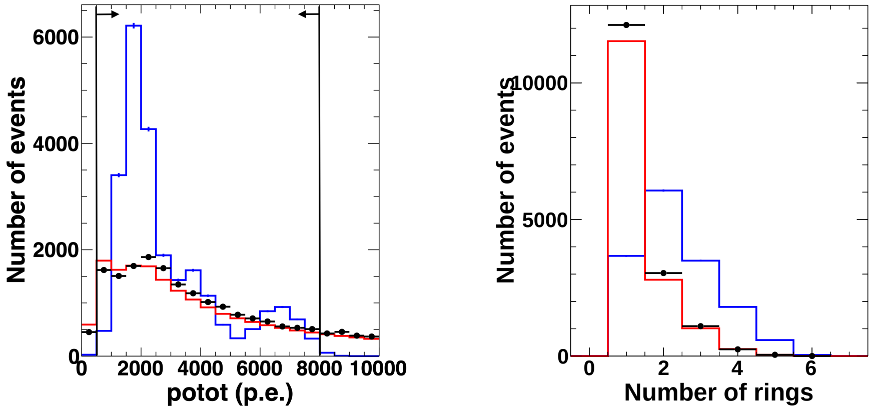

Figure 8.7: The number of p.e.'s after selection C-1 and the number of rings after selection C-2. The data (black dots) are compared with the atmospheric neutrino MC events (red) normalized by the live time, and the signal MC events (blue) normalized to the atmospheric neutrino MC events.

C-1: Events should pass FCFV and E_{vis} selection.

C-2: Total observed photoelectrons (p.e.'s) should be $500 < Q_{\mathrm{tot}} < 8000\,\mathrm{p.e.}$

Since K_L^0 decay is separated from the proton decay in time, and rings tend to overlap with smaller momentum in three-body decay, not all of the rings can be always reconstructed. Even if some rings are not reconstructed, the signal events can be roughly distinguished from the background events by the total observed p.e.'s. The left-hand plot in Figure 8.7 shows the number of p.e.'s after selection C-1.

C-3:

C-3-1: The number of rings should be two or three (for $K_L^0 \to \pi^{\pm} l^{\mp} \nu$).

C-3-2: The number of rings should be four, five or six (for $K_L^0 \to 3\pi^0$).

C-3-3: The number of rings should be three or four (for $K_L^0 \to \pi^+\pi^-\pi^0$).

The right-hand plot in Figure 8.7 shows the number of rings after selection C-2. As explained above, not all charged particles are reconstructed with the Cherenkov ring. Therefore, loose cuts are applied for each decay mode.

C-4:

C-4-1: The number of showering rings should be zero or one (for $K_L^0 \to \pi^{\pm} l^{\mp} \nu$).

The left plot in Figure 8.8 shows the number of showering rings after selection C-3-1. The rings are assumed to be the primary muon and charged pion and lepton from K_L^0 decay. If charged pions have momentum below the Cherenkov threshold, it cannot be observed and the number of rings becomes two. One (zero) showering ring is observed for $K_L^0 \to \pi^{\pm} e^{\mp}$ $(\mu^{\mp})$ ν channel.

C-4-2: The number of non-showering rings should be one (for $K_L^0 \to 3\pi^0$).

The center plot in Figure 8.8 shows the number of non-showering rings after selection C-3-2. The rings are assumed to be the primary muon and γ's from π^0 decay.

C-4-3: The number of showering rings should be two (for $K_L^0 \to \pi^+\pi^-\pi^0$).

The right plot in Figure 8.8 shows the number of showering rings after selection C-3-3. In this decay mode, five particles are generated as candidates of Cherenkov rings (primary muon, two charged pions and two γ's from π^0 decay). Among those, at least one of the pions is invisible due to momentum below the Cherenkov threshold. Four rings are assumed to be due to the primary muon, two γ's from π^0 decay and one of the charged pions from K_L^0 decay. If both charged pions are invisible, the number of rings becomes three.

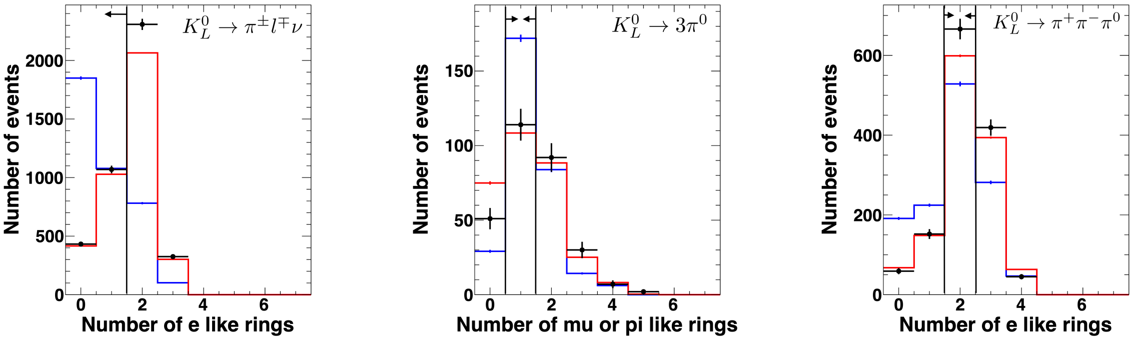

Figure 8.8: The number of showering rings or non-showering rings after C-3 in each selection labeled in the plots. The data (black dots) are compared with the atmospheric neutrino MC events (red) normalized by the live time, and the signal MC events (blue) normalized to the atmospheric neutrino MC events.

C-5:

C-5-1: The number of Michel electrons should be two or three (for $K_L^0 \to \pi^{\pm} l^{\mp} \nu$).

Three Michel electrons are generated as the secondary particles from the decay of the primary muon and the pion (and muon for $K_L^0 \to \pi^{\pm}\mu^{\mp}\nu$) from K_L^0 decay.

C-5-2: The number of Michel electrons should be one (for $K_L^0 \to 3\pi^0$).

Only one Michel electron is generated as the secondary particle from the decay of the primary muon.

C-5-3: The number of Michel electrons should be two or three (for $K_L^0 \to \pi^+\pi^-\pi^0$).

Three Michel electrons are generated as the secondary particles from the decay of the primary muon and two charged pions from K_L^0 decay. If π^- is captured, the number of Michel electrons becomes two.

The three plots in Figure 8.9 show the number of Michel electrons after selection C-4-1 (left), C-4-2 (center) and C-4-3 (right).

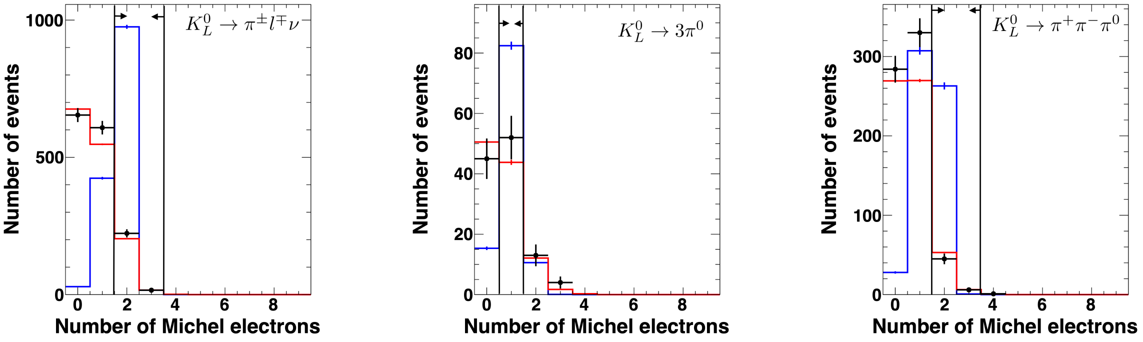

Figure 8.9: The number of Michel electrons after C-4 in each selection labeled in the plots. The data (black dots) are compared with the atmospheric neutrino MC events (red) normalized by the live time, and the signal MC events (blue) normalized to the atmospheric neutrino MC events.

C-6: The reconstructed muon momentum should be $260 < P_\mu < 410\,\mathrm{MeV}/c$

This cut selects the primary muon from $p \to \mu^+ + K^0$ decay with the momentum of $326.5\,\mathrm{MeV}/c^2$. Figure 8.10 shows the reconstructed muon momentum after C-5 selection. The combined muon momentum distribution for all K_L^0 decay selections is also shown in Figure 8.11.

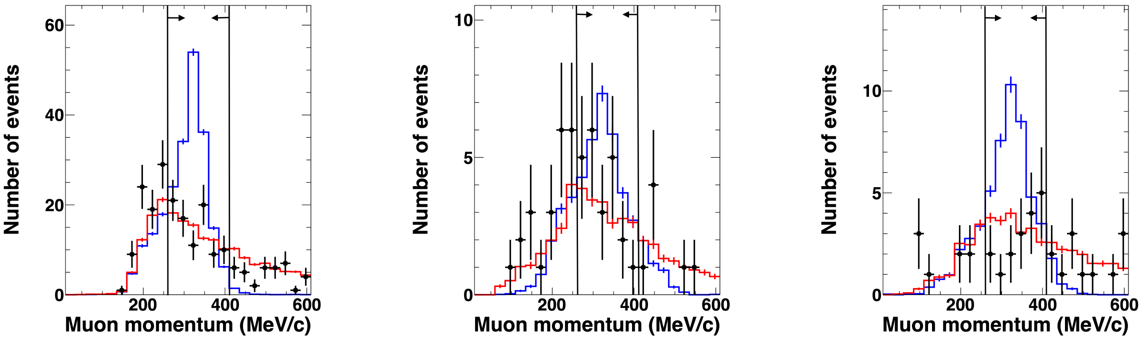

Figure 8.10: Reconstructed muon momentum after C-5 in $K_L^0 \to \pi^{\pm} l^{\mp} \nu$ (left), $K_L^0 \to 3\pi^0$ (center) and $K_L^0 \to \pi^+ \pi^- \pi^0$ (right) selections. The data (black dots) are compared with the atmospheric neutrino MC events (red) normalized by the live time, and the signal MC events (blue) normalized to the atmospheric neutrino MC events.

C-7: The reconstructed vertex separation should be $1.5\,\mathrm{m} < v_{\mathrm{sep}}$ (v_{sep} is defined in the text below).

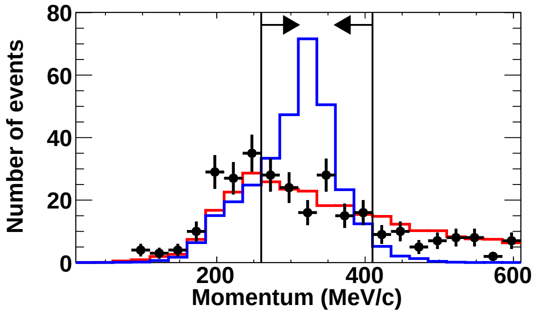

Figure 8.11: Reconstructed muon momentum of all events after C-5-1, C-5-2 and C-5-3 selections. The data (black dots) are compared with the atmospheric neutrino MC events (red) normalized by the live time, and the signal MC events(blue) normalized to the atmospheric neutrino MC events.

Since these K_L^0 decays are three-body decays with relatively long lifetimes, it is difficult to reconstruct all secondary particles. Therefore, strict cuts to the invariant mass are not applied in these selections. Instead, the vertex separation v_{sep} is defined as the distance between the primary (muon) and secondary (kaon) vertices along the opposite direction of the primary muon as illustrated in Figure 8.12, and a cut is applied on it to distinguish the signal events from the backgrounds. Typical $p \to \mu^+ + K_L^0$ events have positive vertex separation due to opposite directions of muon and kaon from proton decay, while the average vertex separation of atmospheric neutrino events is zero.

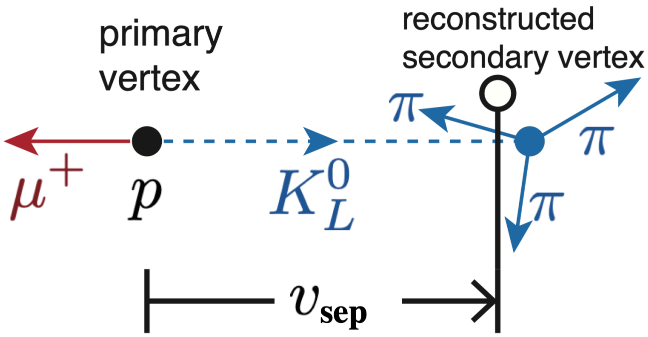

Figure 8.12: A schematic view of vertex separation.

Figure 8.13 shows vertex separation v_{sep} distributions after applying all cuts including C-8 but except for C-7. The combined vertex separation distribution for all K_L^0 decay selections is also shown in Figure 8.14. The right side region is the final sample of K_L^0 decay selection. The peak positions between the signal and atmospheric neutrino MC simulation differ by about 0.5 m. The distribution of the atmospheric neutrino MC simulation has a larger tail in the negative region. This is mainly due to Michel electrons from muons produced by ν_μ CC interaction and the scattering of charged pions in water which causes multiple Cherenkov rings. The value of the vertex separation cut was chosen to optimize for the sensitivity of the proton decay search. One candidate remained in $K_L^0 \to \pi^\pm l^\mp \nu$ selection.

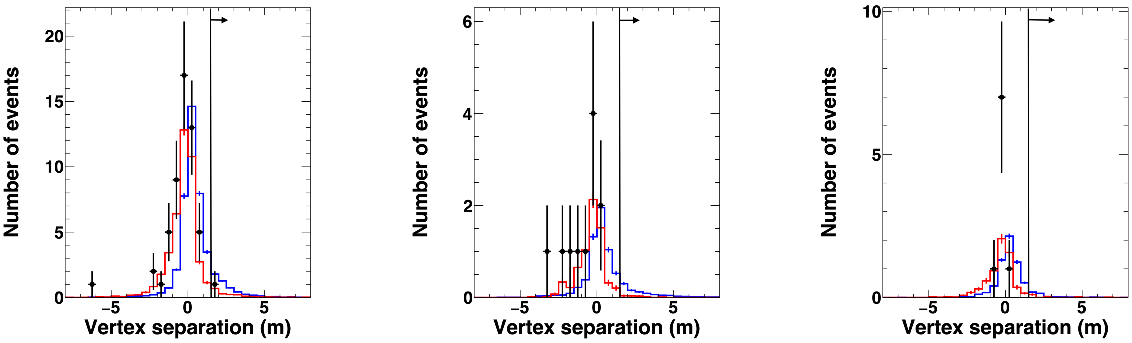

Figure 8.13: Reconstructed vertex separation in $K_L^0 \to \pi^\pm l^\mp \nu$ (left), $K_L^0 \to 3\pi^0$ (center) and $K_L^0 \to \pi^+\pi^-\pi^0$ (right) selections. All cuts except vertex separation are applied. The data (black dots) are compared with the atmospheric neutrino MC events (red) normalized by the live time, and the signal MC events (blue) normalized to the atmospheric neutrino MC events.

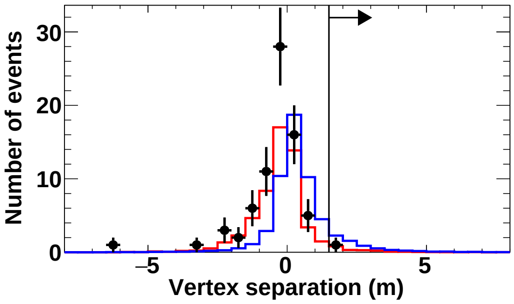

Figure 8.14: Reconstructed vertex separation distribution of all events in $K_L^0 \to \pi^\pm l^\mp \nu$, $K_L^0 \to 3\pi^0$ and $K_L^0 \to \pi^+\pi^-\pi^0$ selections. All cuts except vertex separation are applied. The data (black dots) are compared with the atmospheric neutrino MC events (red) normalized by the live time, and the signal MC events (blue) normalized to the atmospheric neutrino MC events.

C-8: There should be no tagged neutrons.

The three plots in Figure 8.15 show the number of tagged neutrons after selection C-7. About 51%, 73% and 71% of the remaining backgrounds are rejected by requiring no tagged neutrons while 38%, 26% and 42% of the signal events remain for $K_L^0 \to \pi^\pm l^\mp \nu$, $K_L^0 \to 3\pi^0$ and $K_L^0 \to \pi^+\pi^-\pi^0$ selections, respectively.

8.5 Selection summary

Table 8.1 shows a summary of the event selections. It shows the signal efficiency, the number of background events and the number of candidate events after all cuts. The efficiency of each selection is estimated from the proton decay simulation with a definition as a fraction of the number of signal events after selection to the number of generated events (including all decay modes of K^0) within the

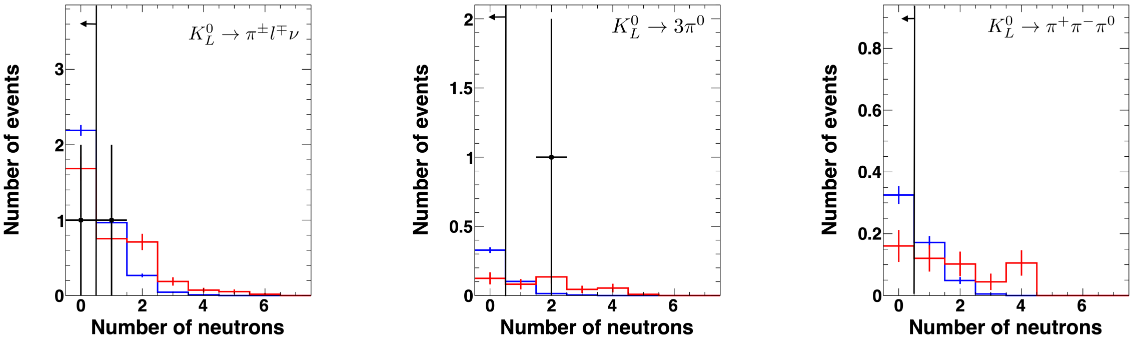

Figure 8.15: The number of tagged neutrons after C-7 in each selection labeled in the plots. The data (black dots) are compared with the atmospheric neutrino MC events (red) normalized by the live time, and the signal MC events (blue) normalized to the atmospheric neutrino MC events.

ID more than 2 m away from the ID wall. The total efficiency for $p \rightarrow \mu^+ + K^0$ decay is 17.0±1.2% and the total number of expected backgrounds is 15.5 ± 2.9 events/(Mton·year) where the unit of Mton·year means a statistics equivalent to one-year observation with one Mton mass. In the SK-IV period, 3.1 ± 0.6 background events are expected in total for 3244.39 live days (0.2 Mton·years exposure of the Super-Kamiokande detector with 22.5 kton fiducial mass). Efficiencies for K_L^0 decay are lower than those for K_S^0 decay due to the cut on the vertex separation, which is necessary to suppress the background. Systematic uncertainties are also shown for the signal efficiencies and the background rates. The details of the systematic uncertainties are explained in Chapter 10. As a result of the selections, one candidate remains in the final samples for $K_L^0 \rightarrow \pi^\pm l^\mp \nu$ selection, while no candidates remained in the final sample of the other selections. As the expected background events for $K_L^0 \rightarrow \pi^\pm l^\mp \nu$ and total channels are 1.7 ± 0.5 and 3.1 ± 0.6, respectively, these number of candidates are consistent with the background. As there are no significant excesses beyond the expected backgrounds, limits of the proton lifetime are set in Chapter 9.

Figure 8.16 shows the signal efficiency, the number of background events and the number of candidates for each step of the selections. For K_S^0 decay modes, about 95% of background events are rejected by the total (proton) momentum cut while keeping about 90% of the signal events. For

Table 8.1: Summary of the $p \rightarrow \mu^+ + K^0$ search in the SK-IV period. Uncertainties are quadratic sums of the MC statistical uncertainties and the systematic uncertainties.

Search mode (branching ratio)		Efficiency (%)	Background (events)	Candidates
$K_S^0 \rightarrow 2\pi^0$	(30.7% for K_S^0)	9.9 ± 1.0	0.3 ± 0.1	0
$K_S^0 \rightarrow \pi^+\pi^-$	(69.2% for K_S^0)	5.2 ± 0.6	0.8 ± 0.2	0
$K_L^0 \rightarrow \pi^\pm l^\mp \nu$	(67.6% for K_L^0)	1.4 ± 0.3	1.7 ± 0.5	1
$K_L^0 \rightarrow 3\pi^0$	(19.5% for K_L^0)	0.37 ± 0.05	0.12 ± 0.06	0
$K_L^0 \rightarrow \pi^+\pi^-\pi^0$	(12.5% for K_L^0)	0.18 ± 0.04	0.16 ± 0.07	0
Total		17.0 ± 1.2	3.1 ± 0.6	1

K_L^0 decay modes, more than 95% of the remaining background events are rejected by the vertex separation cut whereas the signal efficiencies are about 10%.

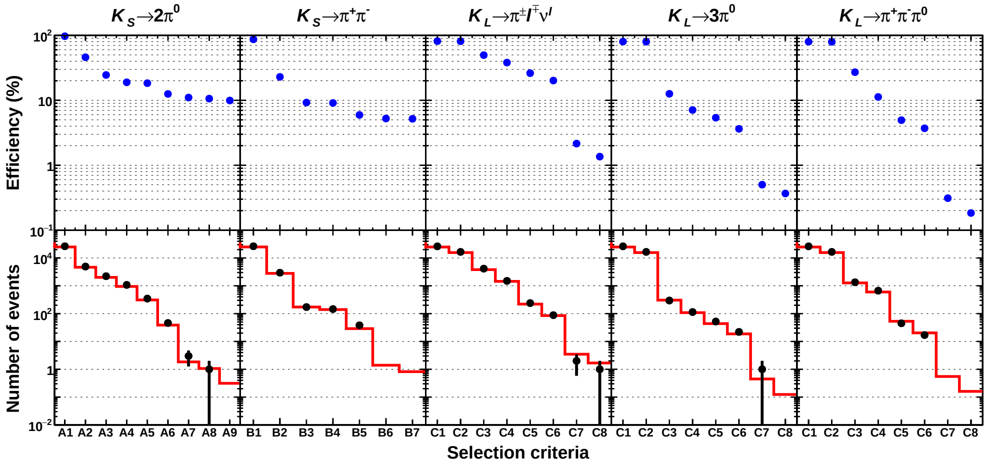

Figure 8.16: Signal efficiencies (blue), number of background events (red) and number of candidates (black) for each step of the selections for SK-IV. Error bars show statistical uncertainty. The number of atmospheric neutrino MC events is normalized by the live time (3244.39 live days).

Table 8.2 shows the breakdown of the remaining background events by the interaction mode of the atmospheric neutrinos (an explanation of neutrino interactions is written in Section 5.3). The major background source is not kaon production but single pion and eta production, and deep inelastic scattering DIS with multiple pions, due to much larger cross sections than the kaon production.

Table 8.2: Breakdown of remaining atmospheric neutrino backgrounds by the interaction mode (%). CC, NC, QE and DIS stand for charged-current, neutral-current, quasi-elastic and deep inelastic scattering, respectively. Uncertainties are statistical. "-" means no events remained in the simulation corresponding to the statistics of the 500 years.

Modes	$K_S^0 \to 2\pi^0$	$K_S^0 \to \pi^+\pi^-$	$K_L^0 \to \pi^\pm l^\mp \nu$	$K_L^0 \to 3\pi^0$	$K_L^0 \to \pi^+\pi^-\pi^0$
CCQE	1.9 ± 1.9	-	9.7 ± 2.8	8.2 ± 8.1	-
CC1π	23.4 ± 9.3	70.2 ± 6.3	82.9 ± 3.6	28.9 ± 15.4	57.3 ± 16.0
CC1K	-	3.4 ± 2.5	-	-	-
CC1η	37.3 ± 10.6	-	-	-	-
CCDIS	31.6 ± 11.5	11.3 ± 4.2	3.2 ± 1.6	48.6 ± 17.7	42.7 ± 16.0
NC	5.8 ± 5.6	15.0 ± 5.5	4.2 ± 2.0	14.2 ± 13.0	-

Chapter 9

Lifetime limit

Since no statistically significant excesses were observed as described in Section 8.5, a lower bound on the proton lifetime was calculated by using a Bayesian method [78][2]. The probability distribution function of the decay width of proton decay is expressed by a Poisson distribution convolved with the systematic uncertainties as follows:

$$P(\Gamma|n_i) = \iiint \frac{e^{-(\Gamma\lambda_i\epsilon_i+b_i)}(\Gamma\lambda_i\epsilon_i + b_i)^{n_i}}{n_i!} P(\Gamma)P(\lambda_i)P(\epsilon_i)P(b_i)d\epsilon_i d\lambda_i db_i, \tag{9.1}$$

where i is an index for each selection. Γ is the decay rate which is a reciprocal of the lifetime. n_i is the number of observed events, λ_i is the exposure (proportional to the live time of the observation), ϵ_i is the signal efficiency and b_i is the number of expected background events. The probability distribution function of decay rate $P(\Gamma)$ is assumed to be uniform as there is no indication of its value. $P(\lambda_i)$, $P(\epsilon_i)$ and $P(b_i)$ are the probability distribution functions for the exposure, efficiency and backgrounds, respectively:

$$P(\lambda_i) \propto \begin{cases} \exp\left(\frac{-(\lambda_i-\mu_{\lambda_i})^2}{2\sigma_{\lambda_i}^2}\right) & (\lambda_i > 0) \\ 0 & (\text{otherwise}) \end{cases} \tag{9.2}$$

$$P(\epsilon_i) \propto \begin{cases} \exp\left(\frac{-(\epsilon_i-\mu_{\epsilon_i})^2}{2\sigma_{\epsilon_i}^2}\right) & (\epsilon_i > 0) \\ 0 & (\text{otherwise}) \end{cases} \tag{9.3}$$

$$P(b_i) \propto \begin{cases} \int_0^\infty \frac{e^{-B}B^{n_{b_i}}}{n_{b_i}!} \exp\left(\frac{-(C_i b_i - B)^2}{2\sigma_{b_i}^2}\right) dB & (b_i > 0) \\ 0 & (\text{otherwise}) \end{cases} \tag{9.4}$$

where σ_{λ_i}, σ_{ϵ_i} and σ_{b_i} are the systematic uncertainties and μ_{λ_i} and μ_{ϵ_i} are the expected exposure and efficiency, respectively. n_{b_i} is the number of expected backgrounds without live time normalization and C_i is a factor to normalize the MC events to the live time of the data. The proton decay rate Γ_{limit} at a 90% C.L. satisfies the following equation using this probability distribution function,

$$0.9 = \int_0^{\Gamma_{\text{limit}}} d\Gamma \prod_i P(\Gamma|n_i). \tag{9.5}$$

The results of all selections are combined in this equation and the decay rate is evaluated. The lower limit of the proton lifetime is expressed as the inverse of the decay rate:

$$\tau_{\text{limit}}/Br = 1/\Gamma_{\text{limit}}, \tag{9.6}$$

where Br is the branching ratio of the proton decay mode.

The lifetime limits by this method are summarized in Table 9.1 with the efficiencies, expected number of backgrounds and number of candidates for each selection. The limit from SK-IV data is 4.5×10^{33} years at 90% C.L.

Table 9.1: Summary of the lifetime limits in $p \to \mu^+ K^0$ search. The signal efficiency, number of background events and number of candidate events for each selection are taken from Table 8.1.

Search mode	Efficiency (%)	Background (events)	Candidates	Lower limit (10^{33} years)
$K_S^0 \to 2\pi^0$	9.9 ± 1.0	0.3 ± 0.1	0	2.8
$K_S^0 \to \pi^+\pi^-$	5.2 ± 0.6	0.8 ± 0.2	0	1.5
$K_L^0 \to \pi^\pm l^\mp \nu$	1.4 ± 0.3	1.7 ± 0.5	1	0.3
$K_L^0 \to 3\pi^0$	0.37 ± 0.05	0.12 ± 0.06	0	0.1
$K_L^0 \to \pi^+\pi^-\pi^0$	0.18 ± 0.04	0.16 ± 0.07	0	0.05
SK-IV combined (199 kton·years)				4.5
SK-I+SK-II+SK-III+SK-IV combined (372 kton·years)				3.6

Then this result from SK-IV data (2008–2018) was combined with the previous result using the statistically independent data in SK-I to SK-III period (1996–2008) [1] and the limit from SK-I to SK-IV data was evaluated. For SK-I to SK-III, all channels in Table A.1 (Appendix) were used. The signal and background estimations for each period and decay mode were added as independent terms in Equation 9.1 to 9.4 and combined in Equation 9.5. Systematic uncertainties were assumed to be fully correlated for the entire period from SK-I to SK-IV assuming common sources. As a result, the limit of 3.6×10^{33} years at 90% C.L. was obtained from 0.37 Mton·years of data. This limit is more than twice as long as the previous result, 1.6×10^{33} years, which uses data for SK-I to SK-III. As explained in Chapter 10, the systematic uncertainties on the kaon scattering for SK-I to SK-III periods were re-evaluated to cover the update of the kaon interaction model when the combined lifetime limit was calculated. This affects mainly the signal efficiency of K_L^0 selection. The lifetime limit for SK-I to SK-III becomes 1.2×10^{33} years with this update. The lower limit given by the combination of SK-I to SK-IV turns out to be smaller than that from only SK-IV data. This can be explained due to two candidates in the final $K_S^0 \to 2\pi^0$ selection sample in SK-II data compared to a background expectation of 0.20 events, which corresponds to a local p-value of 1.8%. On the other hand, no candidate events were found in the $K_S^0 \to 2\pi^0$ selection in SK-IV.

Chapter 10

Systematic uncertainties

Tables 10.1 and 10.2 summarize the systematic uncertainties for the selection efficiencies and the expected background rates, respectively. As the systematic uncertainties in the signal efficiencies associated with the physics process, the correlated decay probability, Fermi momentum models, pion interaction and kaon interaction are considered. Since the flight length of K_L^0 mostly depends on the cross section as described in Section 4.1, the contribution of kaon interaction is larger than the other physics sources in K_L^0 selections. The contribution from pion interaction is negligible in $K_S^0 \to 2\pi^0$ selection as π^0 decay immediately.

Uncertainties in the neutrino flux, neutrino cross section and pion interaction were accounted for in the estimation of the atmospheric neutrino backgrounds. Since the major background events are not kaon production as described in Section 8, the contribution from the kaon interaction is negligible.

As the systematic uncertainties associated with the detector performance and reconstruction, uncertainties in the number of events in the fiducial volume, detector non-uniformity, energy scale, ring counting, particle type identification, decay electron tagging and neutron tagging are considered in the signal efficiencies and background rates. In addition, uncertainties in the vertex separation were evaluated for $K_L^0 \to \pi^\pm l^\mp \nu$, $K_L^0 \to 3\pi^0$ and $K_L^0 \to \pi^+\pi^-\pi^0$ selections. Uncertainties in the vertex separation are among the largest systematic uncertainties for the detector performance and reconstruction in K_L^0 selections. Details of these systematic uncertainties are described in this chapter.

10.1 Correlated decay

As explained in Section 4.1, some theoretical models predict the proton decay process as a pair of two nucleons in the oxygen nucleus (correlated decay). The probability of the correlated proton decay within oxygen is predicted as 10% [35]. Considering the limitation of the reliability of the model, the fraction of correlated decay events was changed to 0% and 20% by weighting events to

Table 10.1: Systematic uncertainties on the signal efficiencies (%)

Sources	$K_S^0 \to 2\pi^0$	$K_S^0 \to \pi^+\pi^-$	$K_L^0 \to \pi^\pm l^\mp \nu$	$K_L^0 \to 3\pi^0$	$K_L^0 \to \pi^+\pi^-\pi^0$
Physics					
Correlated decay	6.1	6.3	5.6	3.9	2.7
Fermi momentum	1.0	1.8	1.3	0.1	1.0
Pion interaction	-	4.5	2.7	1.8	6.3
Kaon interaction	3.1	3.1	11.6	5.3	10.3
Reconstruction					
Fiducial Volume	4.0	3.4	0.5	0.5	0.5
Energy scale	1.9	1.6	0.9	4.7	2.3
Non-uniformity	0.2	0.2	-	-	-
Ring counting	0.4	0.4	2.8	2.8	2.8
Particle identification	0.4	0.2	0.6	5.1	0.8
Michel electron tagging	5.4	5.4	5.4	5.4	5.4
Vertex separation	-	-	10.5	4.8	9.2
Neutron tagging	0.6	-	2.6	2.2	3.0
Total	9.9	10.8	18.2	12.6	17.0

Table 10.2: Systematic uncertainties on the number of the expected background events (%)

Sources	$K_S^0 \to 2\pi^0$	$K_S^0 \to \pi^+\pi^-$	$K_L^0 \to \pi^\pm l^\mp \nu$	$K_L^0 \to 3\pi^0$	$K_L^0 \to \pi^+\pi^-\pi^0$
Physics					
Neutrino flux	8.7	6.8	6.6	8.0	7.9
Neutrino interaction	20.0	21.5	22.6	20.0	24.0
Pion interaction	17.4	9.9	9.0	8.4	13.3
Reconstruction					
Fiducial Volume	4.0	3.4	0.5	0.5	0.5
Energy scale	19.9	2.7	5.4	14.6	0.1
Non-uniformity	5.8	1.1	-	-	-
Ring counting	0.4	0.4	2.8	2.8	2.8
Particle identification	<0.1	<0.1	<0.1	28.9	<0.1
Michel electron tagging	5.4	5.4	5.4	5.4	5.4
Vertex separation	-	-	13.9	10.7	16.6
Neutron tagging	2.7	-	2.7	2.9	2.6
Total	35.5	25.6	28.9	41.4	32.5

evaluate the systematic uncertainty.

$$\epsilon_{\text{sys}} = \frac{n_{\text{free}}}{N_{\text{tot}}} + \frac{N_S + N_P \mp \alpha N_{\text{corr}}}{N_S + N_P} \times \frac{n_S + n_P}{N_{\text{tot}}} + (1 \pm \alpha) \times \frac{n_{\text{corr}}}{N_{\text{tot}}} \tag{10.1}$$

where n is the number of signal MC events passing the selection criteria, N is the number of generated proton decay MC events in the fiducial volume, " free " stands for free proton decays, S (P) stands for proton decays in the S (P) state in ^{16}O, and " corr " stands for correlated decays. A factor $\alpha = 1, -1$ corresponds to correlated decay probability of 20% and 0%, respectively. The most discrepant ϵ_{sys} between the $\alpha = 1$ and $\alpha = -1$ from normal efficiency is taken for the uncertainty estimation.

10.2 Fermi momentum

As explained in Section 4.1, protons have Fermi momentum up to a few hundred MeV in the oxygen nucleus. The Fermi momentum distribution is implemented in the proton decay based on the experimental data [33]. On the other hand, the Fermi gas model [41] is employed in the atmospheric neutrino MC simulation (NEUT). This model uncertainty ϵ_{sys} is evaluated from the difference between the two models shown in Figure 10.1. The events in the final sample are weighted by the fraction of the Fermi momentum distributions with 11 bins (bin width is 25 MeV/c), and the uncertainty was estimated by the deviation from the number of events before the weighting.

$$\epsilon_{\text{sys}} = \frac{n_{\text{free}}}{N_{\text{tot}}} + \sum_{i=1}^{11} \frac{n_i}{N_{\text{tot}}} \times \frac{N_{\text{NEUT},i}}{N_{\text{PD},i}}, \tag{10.2}$$

where i is the index of each momentum bin, $N_{\text{PD},i}$ and $N_{\text{NEUT},i}$ are the fraction of events in the Fermi momentum distribution of the proton decay MC and atmospheric neutrino MC simulation, respectively.

10.3 Pion interaction

The pion interaction model is implemented in the simulation with six internal parameters based on the pion scattering experiments [74][75][76]: absorption probability f_{ABS}, quasi-elastic (QE) scattering probability f_{QEL}, charge exchange fraction of QE scattering f_{CXL}, elastic scattering probability f_{ELH}, charge exchange probability f_{CXH} and inelastic scattering probability f_{HAD}. The applicable momentum region is below 500 MeV/c for the first three parameters and above 500 MeV/c for the other parameters. The nominal values of these parameters are

$$(f_{\text{QEL}}, f_{\text{ELH}}, f_{\text{HAD}}, f_{\text{ABS}}, f_{\text{CXL}}, f_{\text{CXH}}) = (1.069, 1.824, 1.002, 1.404, 0.697, 1.800).$$

To cover the possible parameter space from measurements, 24 patterns of the parameters are prepared (Table 10.3) in addition to the nominal one. For each case, events in the final sample are

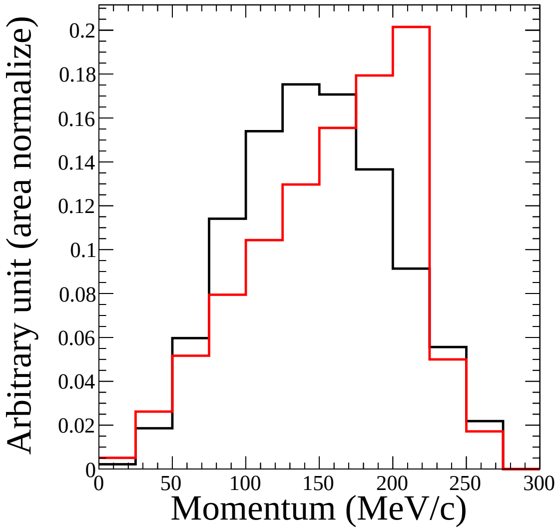

Figure 10.1: Fermi momentum distributions of the proton decay MC (black) and atmospheric neutrino MC simulation (red).

weighted by the fraction of the interaction probability to the nominal one, and the variations of the signal efficiencies and background rates are calculated. The standard deviations of 24 biased efficiencies and background rates over the nominal values are assigned as systematic uncertainties.

10.4 Kaon interaction

The simulation of the kaon interaction consists of two steps: interaction inside the oxygen nucleus in which proton decay or atmospheric neutrino interaction occurs and in water with the other nuclei. For short distance ($\mathcal{O}(10^{-14})$ m) in the nucleus, the kaon interaction is simulated as an eigenstate of K^0. Although there are no experimental data for the kaon-oxygen cross sections, the kaon-oxygen cross section in NEUT was compared with the estimation by extrapolation from the kaon-deuteron cross section measurement scaled by the atomic number to oxygen as shown in Figure 10.2. This discrepancy is due to the interaction of kaons in the oxygen nucleus as described in Section 4.1. The deviation was estimated as ±25% to cover the discrepancy between the extrapolation from the measurements and the simulation around the 300 MeV/c momentum, and it was used for the evaluation of the uncertainty. By the same method as the evaluation of the systematic uncertainty for the Fermi momentum, events in the final sample were weighted and the uncertainty was estimated by the deviation from the number of events before the weighting. The weights were determined by the fraction of the type of interaction (elastic or charge-exchange), kaon momentum and direction between distributions with normal and biased cross sections. The maximum deviation of the efficiency from the nominal value was investigated with ±25% variation of the kaon interaction

Table 10.3: Parameter sets for the estimation of pion interaction uncertainty.

f_{QEL}	f_{ELH}	f_{HAD}	f_{ABS}	f_{CXL}	f_{CXH}
0.6	1.8	1.0	0.7	0.5	1.8
0.6	1.8	1.0	0.7	1.6	1.8
0.7	1.8	1.0	1.6	0.4	1.8
0.7	1.8	1.0	1.6	1.6	1.8
1.4	1.8	1.0	0.6	0.6	1.8
1.3	1.8	1.0	0.7	1.6	1.8
1.5	1.8	1.0	1.5	0.4	1.8
1.6	1.8	1.0	1.6	1.6	1.8
0.6	1.1	1.5	0.7	0.5	2.3
0.6	1.1	1.5	0.7	1.6	2.3
0.7	1.1	1.5	1.6	0.4	2.3
0.7	1.1	1.5	1.6	1.6	2.3
1.4	1.1	1.5	0.6	0.6	2.3
1.3	1.1	1.5	0.7	1.6	2.3
1.5	1.1	1.5	1.5	0.4	2.3
1.6	1.1	1.5	1.6	1.6	2.3
0.6	2.3	0.5	0.7	0.5	1.3
0.6	2.3	0.5	0.7	1.6	1.3
0.7	2.3	0.5	1.6	0.4	1.3
0.7	2.3	0.5	1.6	1.6	1.3
1.4	2.3	0.5	0.6	0.6	1.3
1.3	2.3	0.5	0.7	1.6	1.3
1.5	2.3	0.5	1.5	0.4	1.3
1.6	2.3	0.5	1.6	1.6	1.3

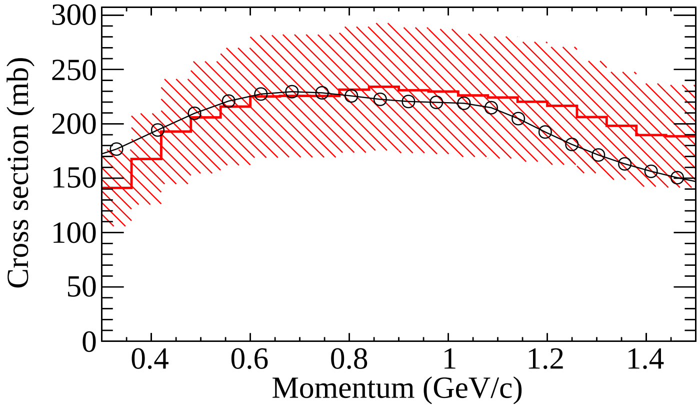

Figure 10.2: $K^0, {}^{16}$O cross section (elastic+charge exchange). Extrapolation from the experimental data (black) and simulation in NEUT (Red) are shown. The shaded region is a ±25% area of the cross section in NEUT.

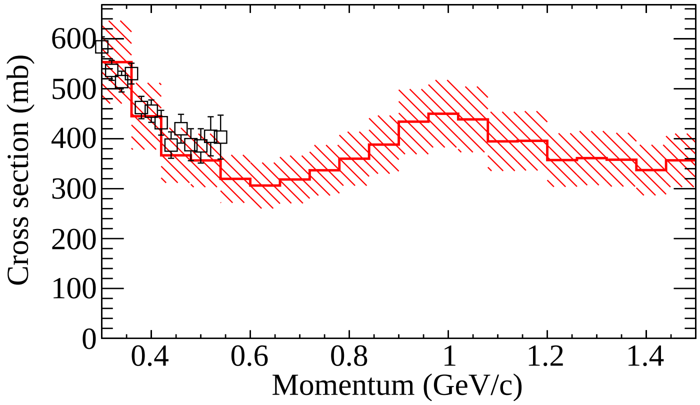

Figure 10.3: Total $K_L^0, {}^{16}$O cross section. Extrapolation from the experimental data (black) and simulation in water (Red) are shown. The shaded region is a ±15% area of the cross section in water.

cross section and taken as the uncertainty.

For longer distances in water, the kaon interaction is simulated as eigenstates of K_S^0 and K_L^0. The uncertainty of the K_L^0 cross section in water was evaluated from the comparison of the simulation model and the independent measurement of K_L^0-nucleon scattering [77] as well as K^0 cross section (Figure 10.3). The deviation was estimated to be ±15% from this comparison. The systematic uncertainties were estimated by the weights determined by the fraction of the type of interaction (hadronic inelastic scattering, K_S^0 decay or K_L^0 decay), kaon momentum before interaction, and vertex separation between distributions from the variation with nominal and biased cross sections.

A quadratic sum of the uncertainties in nuclei and water is assigned as a systematic uncertainty of the kaon interaction in Table 10.1. As the kaon interaction model is updated from the previous analysis [1], systematic uncertainties for efficiencies of the SK-I to SK-III search in the previous analysis were re-evaluated to cover the difference between the old and new models. They are summarized in Table A.1 (Appendix).

10.5 Neutrino flux and cross section

The uncertainties of the neutrino flux and cross section are based on the atmospheric neutrino oscillation analysis in SK [64]. Events in the final sample are weighted with the ratio of two models or the estimated range of the variations, and the uncertainties are evaluated as the difference between the number of events with and without the weighting. Tables 10.4 and 10.5 summarize the systematic uncertainties in the background rates associated with the neutrino flux and cross section models, respectively.

Table 10.4: Systematic uncertainties on the background rates associated with the neutrino flux model. E_ν is neutrino energy.

Source	$K_S^0 \to 2\pi^0$	$K_S^0 \to \pi^+\pi^-$	$K_L^0 \to \pi^\pm l^\mp \nu$	$K_L^0 \to 3\pi^0$	$K_L^0 \to \pi^+\pi^-\pi^0$
Absolute normalization					
($E_\nu < 1\,\mathrm{GeV}$)	<0.1%	3.2%	3.6%	1.2%	<0.1%
($1 < E_\nu\,\mathrm{GeV}$)	7.0%	4.3%	4.0%	6.4%	7.0%
ν_μ/ν_e ratio					
($E_\nu < 1\,\mathrm{GeV}$)	<0.1%	0.4%	0.4%	<0.1%	<0.1%
($1 < E_\nu < 10\,\mathrm{GeV}$)	0.6%	0.8%	0.7%	0.5%	1.2%
($10 < E_\nu\,\mathrm{GeV}$)	<0.1%	<0.1%	<0.1%	<0.1%	<0.1%
$\bar{\nu}_e/\nu_e$ ratio					
($E_\nu < 1\,\mathrm{GeV}$)	<0.1%	<0.1%	<0.1%	<0.1%	<0.1%
($1 < E_\nu < 10\,\mathrm{GeV}$)	0.7%	<0.1%	<0.1%	0.7%	0.3%
($10 < E_\nu\,\mathrm{GeV}$)	<0.1%	<0.1%	<0.1%	<0.1%	<0.1%
$\bar{\nu}_\mu/\nu_\mu$ ratio					
($E_\nu < 1\,\mathrm{GeV}$)	<0.1%	0.4%	0.4%	<0.1%	<0.1%
($1 < E_\nu < 10\,\mathrm{GeV}$)	1.8%	1.5%	1.5%	1.9%	2.7%
($10 < E_\nu\,\mathrm{GeV}$)	<0.1%	<0.1%	<0.1%	<0.1%	<0.1%
Asymmetry					
Up/down	<0.1%	<0.1%	<0.1%	<0.1%	<0.1%
Horizontal/vertical	0.1%	<0.1%	0.2%	0.3%	<0.1%
K/π ratio	4.7%	3.7%	3.5%	4.2%	2.3%
Neutrino flight length	<0.1%	<0.1%	<0.1%	<0.1%	<0.1%
Total	8.7%	6.8%	6.6%	8.0%	7.9%

10.6 Fiducial volume

A systematic uncertainty for the FV is estimated for the possible difference in the number of events in the FV between data and the MC simulation. Sub-GeV ($E_{\mathrm{vis}} < 1330\,\mathrm{MeV}$) multi-ring samples of the data and the atmospheric neutrino MC simulation were used for this estimation. To determine a stable region where the vertex reconstruction accuracy does not affect the number of events, reconstructed D_{wall} (distance between the interaction point and the nearest ID wall)

Table 10.5: Systematic uncertainties on the background rates associated with the neutrino cross section model.

Source	$K_S^0 \to 2\pi^0$	$K_S^0 \to \pi^+\pi^-$	$K_L^0 \to \pi^\pm l^\mp \nu$	$K_L^0 \to 3\pi^0$	$K_L^0 \to \pi^+\pi^-\pi^0$
Axial vector mass	10.7%	11.1%	13.7%	5.2%	11.2%
NCEL and CCQE ratio	0.2%	<0.1%	1.1%	1.2%	<0.1%
$\bar{\nu}/\nu$ ratio of CCQE	<0.1%	<0.1%	0.3%	0.2%	<0.1%
μ/e ratio of CCQE	<0.1%	<0.1%	<0.1%	<0.1%	<0.1%
Single meson production	12.1%	16.4%	17.2%	5.8%	11.5%
$\bar{\nu}/\nu$ ratio of single π	2.8%	4.2%	4.6%	8.0%	4.5%
DIS (model dependence)	11.2%	6.4%	0.8%	16.0%	17.2%
DIS (total cross section)	1.9%	0.9%	0.2%	3.1%	2.1%
Coherent pion production	<0.1%	<0.1%	<0.1%	<0.1%	<0.1%
NC/CC ratio	1.2%	3.0%	0.8%	2.8%	<0.1%
Total	20.0%	21.5%	22.6%	20.0%	24.0%

distribution was compared with the true values in the MC simulation, MC true values were smeared by Gaussian with $\sigma = 40\,\text{cm}$ (green) and $\sigma = 100\,\text{cm}$ (blue) to account for the resolution of the vertex reconstruction as shown in Figure 10.4. As a result, the ratio was stable in $600 < D_{\text{wall}} < 1000\,\text{cm}$ region. Therefore, the MC simulation was normalized to data in this region, and the number of events in the FV ($D_{\text{wall}} > 200\,\text{cm}$) was compared between the data and MC simulation (Figure 10.5). Since the definition of the reconstructed primary vertex is different for selections, uncertainties were evaluated for three cases: $K_S^0 \to 2\pi^0$, $K_S^0 \to \pi^+\pi^-$ and K_L^0 decay selections.

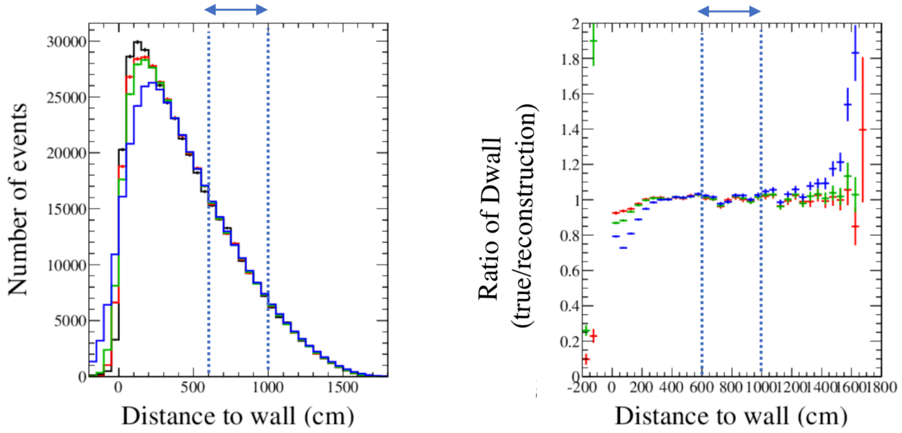

Figure 10.4: Left: distance from the wall of the ID. Reconstructed distribution (black) is compared with MC true (red), MC true smeared by Gaussian with $\sigma = 40\,\text{cm}$ (green) and $\sigma = 100\,\text{cm}$ (blue). Right: ratio of MC true distributions to the reconstructed one.

10.7 Energy scale

As described in Section 3.8, the energy calibration is performed using independent control samples with known energies. The energy scale uncertainty was evaluated as 2.17% from the difference

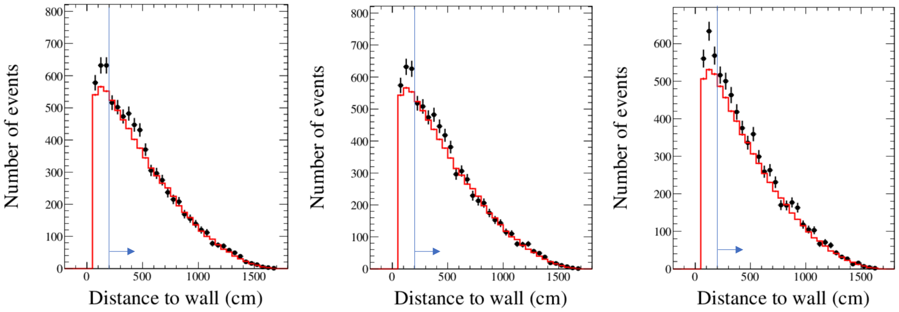

Figure 10.5: Reconstructed distance between the wall of the ID and the position of the particle generation in the sub-GeV multi-ring sample. The simulation (red) are normalized to the data (black) in $600 < D_{\mathrm{wall}} < 1000\,\mathrm{cm}$ region. From left to right, the distribution with the definition of the reconstructed primary vertex for $K_S^0 \rightarrow 2\pi^0$, $K_S^0 \rightarrow \pi^+\pi^-$ and K_L^0 decay selections.

between the data and MC simulation[69]. It affects the muon momentum, total momentum and invariant mass of kaon and proton. The uncertainties were evaluated from the variation of the number of events in the final samples with a bias in the energy scale to these variables.

10.8 Detector non-uniformity

Non-uniformity of the detector response, such as due to PMT and water transparency, is one of the sources of uncertainty in the measurement. Such non-uniformity causes bias in the energy scale depending on the direction of the particles (corresponds to the location of PMTs where Cherenkov light is detected). The uncertainty was evaluated to be 0.58% in the energy scale [69]. This affects the total momentum since the directions of μ^+ and K^0 from proton decay are back-to-back. The impact on the signal efficiency and the expected background rates were evaluated by the MC simulation as shown in Table 10.1 and 10.2.

10.9 Ring counting

The number of rings is used in all selections in the $p \rightarrow \mu^+ + K^0$ search. In the reconstruction, likelihood values are compared for two hypotheses with n rings and $n+1$ rings and the additional ring is adopted if the likelihood with $n+1$ rings exceeds the threshold (see Chapter 7). In this analysis, systematic uncertainty in the number of rings was evaluated from the likelihood distributions.

Figure 10.6 shows the ring counting likelihood of data and simulation in the sub-GeV FCFV sample. The scale and shift parameters for the simulation were determined to reproduce data. The best scale and shift parameters in multi-ring (displaced) fitter are 0.998 ± 0.006 and 0.17 ± 0.02 (1.026 ± 0.005 and 0.38 ± 0.02), respectively. The uncertainties are evaluated as the variation of the multi-ring events fraction of the sub-GeV FCFV sample in this bias.

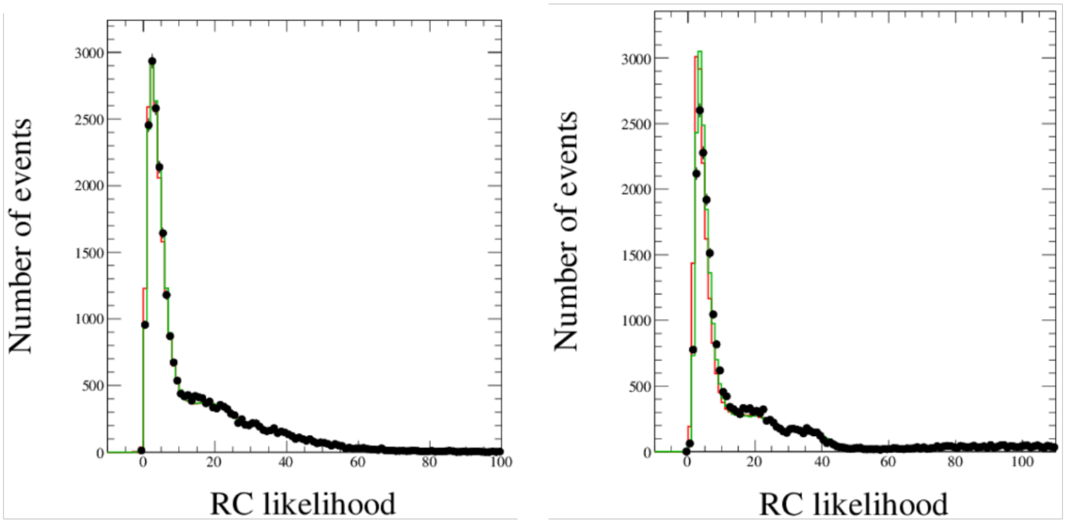

Figure 10.6: Ring counting likelihood of data (black), simulation (red) and simulation with the best-fit parameters for the correction (green) in sub-GeV FCFV sample. The likelihood by multi-ring fitter (left) and displaced vertex fitter (right) are shown.

10.10 Particle type identification

Systematic uncertainty in the particle type identification was also estimated by a similar approach as that for the number of rings (Section 10.9) from the likelihood distributions calculated by the event reconstruction algorithm. Figure 10.7 shows the particle type likelihood for the first ring of the data and simulation in sub-GeV ($E_{\mathrm{vis}} < 1330\,\mathrm{MeV}$) FCFV multi-ring sample. The scale and shift parameters for the simulation were determined to reproduce the data for each ring as well as the first ring. Table 10.6 shows the best-fit parameters for each ring. Fifth and sixth ring distributions are merged to accumulate statistics. These biases were applied to the simulation and uncertainties are evaluated from the variation of the number of events in the final sample of the proton decay event selections.

Table 10.6: The best-fit parameters of the particle type likelihood for each ring.

	Multi-ring fitter		Displaced vertex fitter	
Ring	Scale	Shift	Scale	Shift
First	0.96 ± 0.01	2.7 ± 2.4	1.01 ± 0.01	1.8 ± 3.0
Second	0.97 ± 0.01	0.6 ± 1.2	1.00 ± 0.01	-1.9 ± 1.3
Third	0.97 ± 0.01	-2.2 ± 1.3	0.99 ± 0.02	-2.0 ± 1.6
Fourth	0.97 ± 0.02	-0.6 ± 1.8	1.06 ± 0.04	-3.9 ± 3.5
Fifth and Sixth	0.95 ± 0.03	-2.5 ± 2.3	1.14 ± 0.10	-23.2 ± 7.0

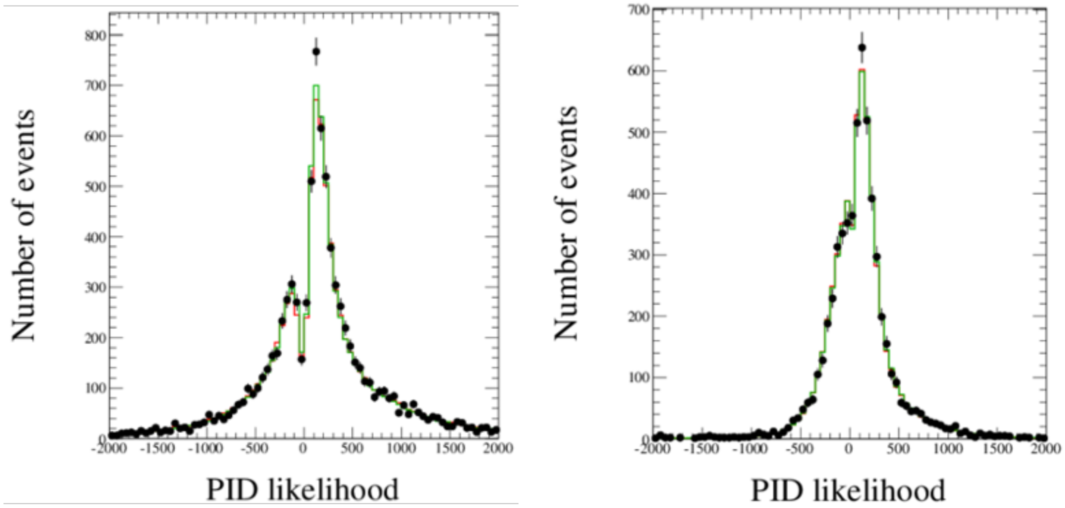

Figure 10.7: Particle type likelihood for the first ring of data (black), simulation (red) and simulation with the best-fit parameters for the correction (green) in sub-GeV FCFV multi-ring sample. The likelihood by multi-ring fitter (left) and displaced vertex fitter (right) are shown.

10.11 Michel electron tagging

The number of Michel electrons after the primary event is related to the number of muons and also charged pions as the parent particle of muons. Therefore, the information is used in the selections of the $p \to \mu^+ + K^0$ search. Figure 10.8 shows the number of Michel electrons of the data and the atmospheric neutrino simulation in the sub-GeV FCFV multi-ring sample. Both distributions are normalized by their areas. Systematic uncertainty is evaluated to account for the relative error between the data and MC simulation in the number of events with zero, one and two Michel electrons.

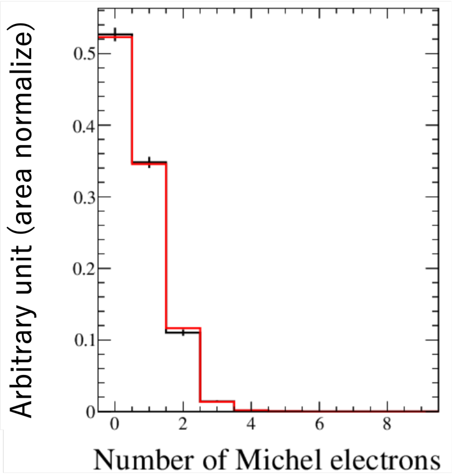

Figure 10.8: The number of Michel electrons of data (black) and atmospheric neutrino simulation (red) in sub-GeV FCFV multi-ring sample.

10.12 Vertex separation

A systematic uncertainty of vertex separation reconstruction is evaluated by comparison between true and reconstructed vertex separation in the proton decay simulation. All cuts before the vertex separation cut were applied. Figure 10.9 shows the difference between true and reconstructed vertex separation. Table 10.7 shows the results of the Gaussian fitting to these distributions. The mean values from the fits are applied to the simulation as bias, and the variations of the number of events in the final sample were taken as the systematic uncertainties.

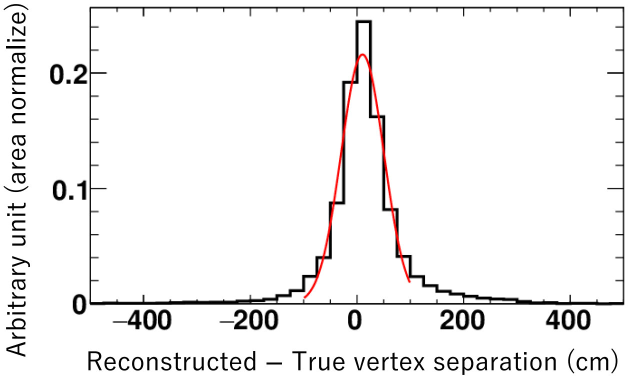

Figure 10.9: Distribution of reconstructed − true vertex separation in the proton decay simulation to which all cuts before the vertex separation cut were applied. The red line shows the Gaussian fit result.

Table 10.7: The results of the Gaussian fittings to the reconstructed − true vertex separation distributions. μ is a mean and σ is a standard deviation.

Selection	μ (cm)	σ (cm)
$K_L^0 \to \pi^\pm l^\mp \nu$	10.3 ± 0.4	40.0 ± 0.4
$K_L^0 \to 3\pi^0$	5.9 ± 1.0	42.4 ± 1.0
$K_L^0 \to \pi^\pm l^\mp \nu$	6.8 ± 0.9	39.1 ± 0.8

It was also checked if the deviation between the data and the simulation is consistent with these uncertainties. The agreement of the data and simulation was evaluated using muons and their Michel electrons. The displaced vertex fitter was applied to atmospheric neutrino events with the following criteria to select ν_μ CCQE events around the lifetime of K_L^0 (50 ns).

- Events should pass FCFV selection and are sub-GeV.
- The number of rings should be two with one non-showering (μ) and one showering (e) rings.
- The number of Michel electrons is one or zero.
- The momentum of the non-showering ring is $450 < p_\mu < 550\,\mathrm{MeV}/c$.
- The momentum of the showering ring is $10 < p_e < 80\,\mathrm{MeV}/c$.

- Time difference between two rings is less than 100 ns.

Figure 10.10 shows the vertex separations of the events after the selection. It was found from the comparison that the distribution of the simulation best reproduces the data with a shift of (7.0 ± 3.9) cm. This is a comparable size to the systematic uncertainties in Table 10.7.

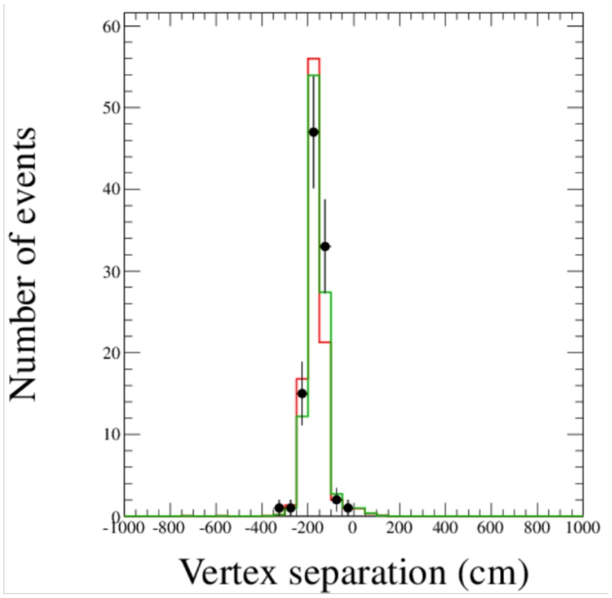

Figure 10.10: The vertex separations of the data (black), the simulation (red) and the simulation with the correction (green) after ν_μ CCQE event selection. The simulation is normalized by the live time.

10.13 Neutron tagging efficiency

Uncertainty in the neutron tagging efficiency is evaluated as ±9% [72]. Systematic uncertainty on the proton decay efficiencies and the expected backgrounds are evaluated from the variation of the number of events in the final sample with different neutron tagging efficiency by ±9%. The neutron tagging efficiencies in the final sample are determined by applying binominal probabilities to the true neutron distributions to reproduce the tagged neutron distributions in the sample before the neutron cut. For example, Figure 10.11 shows the number of neutron distributions in the $K_L^0 \rightarrow \pi^\pm l^\mp \nu$ sample. Several binominal probabilities are applied to the true number of neutrons, and the variation of the event fraction between before and after the neutron cut in ±9% around the best tagging efficiency (about 28.7%) is evaluated as the systematic uncertainty (Figure 10.12).

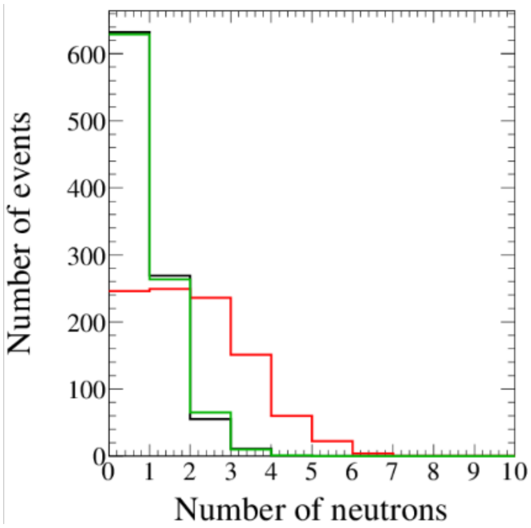

Figure 10.11: The number of tagged neutrons (black), true neutrons (red) and true neutrons with 28.7% tagging efficiency (green) in the $K_L^0 \to \pi^{\pm} l^{\mp} \nu$ sample before the neutron cut.

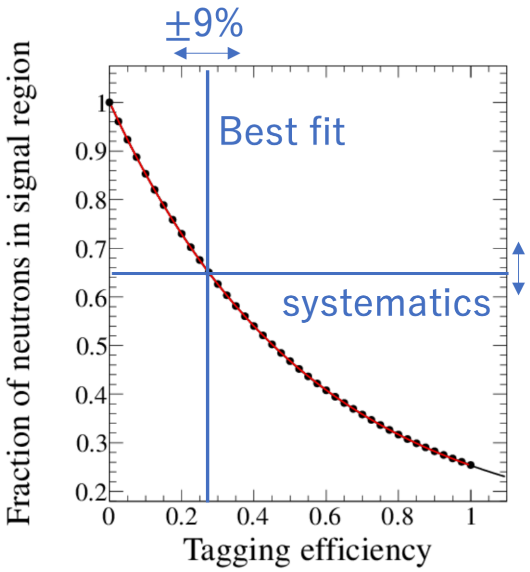

Figure 10.12: The fraction of events with no tagged neutron in the $K_L^0 \to \pi^{\pm} l^{\mp} \nu$ sample before the neutron cut as a function of the several tagging efficiencies.

Chapter 11

Conclusion

Proton decay into a muon and a neutral kaon ($p \to \mu^+ + K^0$) was searched for using the data from the Super-Kamiokande water Cherenkov detector. The sensitivity was improved from the previous search [1] with a new event reconstruction algorithm, neutron tagging and optimized selection criteria for each K_S^0 and K_L^0 decay mode. In addition, the simulation of the kaon interaction was updated based on the external measurement of the kaon scattering.

K^0 is a superposition of K_S^0 with a lifetime of 90 ps and K_L^0 with a lifetime of 51 ns. Therefore, $p \to \mu^+ + K^0$ was searched by different approaches for K_S^0 and K_L^0 decay modes. K_S^0 decays at almost the same position as proton decay and most of the particles from K_S^0 decay can be measured in the Super-Kamiokande detector. Therefore, signal events from $p \to \mu^+ + K^0$ are selected by requiring an invariant mass of K_S^0 and proton. On the other hand, K_L^0 decays at a distance of $\mathcal{O}(1)$ m away from the position of the proton decay after scattering in water and the secondary particles from K_L^0 decay create Cherenkov rings at the secondary vertex. Since the primary muon of $p \to \mu^+ + K^0$ creates a clear Cherenkov ring at the primary vertex of the proton decay, two vertices from the muon and the secondary particles from K_L^0 decay exist in $p \to \mu^+ + K_L^0$ channel. For this reason, the multi-ring reconstruction algorithm was modified for $p \to \mu^+ + K_L^0$ event selection to reconstruct a muon from proton decay and particles generated from K_L^0 decay at the displaced vertex. To effectively distinguish the $p \to \mu^+ + K_S^0$ and $p \to \mu^+ + K_L^0$ events from the backgrounds, five selection criteria are developed for each K_S^0 and K_L^0 decay channel.

As a result, no significant signal has been observed in the final sample of 0.2 Mton·years of data in the SK-IV period (2008–2018). From this result, a lower limit of 4.5×10^{33} years on the lifetime of $p \to \mu^+ + K^0$ was obtained at 90% C.L. By combining this with the previous results using the data in SK-I to SK-III period (1996–2008), a lower limit of 3.6×10^{33} years was obtained from 0.37 Mton·years data. This limit is more than twice as long as the previous result of 1.6×10^{33} years [1] and is the most stringent for this channel. The result of this study provides knowledge in elementary particle physics by the constraints on the grand unified theories.

Acknowledgments

I am deeply grateful to my supervisor Masaki Ishitsuka. He spent a great deal of time and effort giving me many comments and advice which were always thoughtful and suggestive and helped me grow. This thesis would never completed without his support.

I would like to thank all members of the SK group. In particular, Makoto Miura and Shunichi Mine made many specific and important comments on the technical details in the analysis of proton decay. I received many useful suggestions not only for analysis but also for writing the paper. I also thank Edward Kearns and Jost Migenda. They gave me many very essential suggestions for the analysis and writing the paper. I would like to thank Yoshinari Hayato and Roger Wendell for giving me many suggestions, especially for the simulation of proton decay and atmospheric neutrino. I express my gratitude to Akira Takenaka for advice on the analysis of proton decay and FC reduction.

This work was supported by Grant-in-Aid for JSPS Research Fellow Grant Number JP22J14531. I thank the financial support.

Finally, I am very grateful to my family for supporting my life as a student for a long period.

Appendix A

$p \to \mu^+ + K^0$ search in SK-I to SK-III

Table A.1 shows the summary of $p \to \mu^+ + K^0$ search in SK-I to SK-III. These systematic uncertainties are re-evaluated due to the updated kaon interaction model. The selection criteria of SK-I, SK-II and SK-III are different from those of SK-IV.

Table A.1: Summary of the $p \to \mu^+ K^0$ search in SK-I to SK-III [1].

Search mode	Efficiency (%)	Background (events)	Candidates
SK-I (91.7 kton·years)			
$K_S^0 \to 2\pi^0$	7.0 ± 0.7	0.37 ± 0.05	0
$K_S^0 \to \pi^+\pi^-$ (2 ring sample)	10.6 ± 1.1	3.0 ± 0.5	6
$K_S^0 \to \pi^+\pi^-$ (3 ring sample)	2.5 ± 0.3	0.12 ± 0.08	0
K_L^0	3.8 ± 1.8	3.5 ± 1.1	2
SK-II (49.2 kton·years)			
$K_S^0 \to 2\pi^0$	6.2 ± 0.8	0.20 ± 0.05	2
$K_S^0 \to \pi^+\pi^-$ (2 ring sample)	10.3 ± 1.3	1.6 ± 0.4	0
$K_S^0 \to \pi^+\pi^-$ (3 ring sample)	2.4 ± 0.3	0.23 ± 0.08	1
K_L^0	3.3 ± 1.6	1.4 ± 0.5	0
SK-III (31.9 kton·years)			
$K_S^0 \to 2\pi^0$	6.7 ± 0.9	0.19 ± 0.04	0
$K_S^0 \to \pi^+\pi^-$ (2 ring sample)	10.3 ± 1.9	1.2 ± 0.2	1
$K_S^0 \to \pi^+\pi^-$ (3 ring sample)	3.0 ± 0.3	0.09 ± 0.02	0
K_L^0	3.8 ± 1.8	1.3 ± 0.6	1

Bibliography

[1] C. Regis *et al.*, "Search for Proton Decay via $p \to \mu + K^0$ in Super-Kamiokande I, II, and III", Phys. Rev. D **86**, 012006 (2012).

[2] R. L. Workman *et al.* (Particle Data Group), Prog. Theor. Exp. Phys. **2022**, 083C01 (2022).

[3] H. Georgi and S. L. Glashow, "Unity of All Elementary Particle Forces", Phys. Rev. Lett. **32**, 438–441 (1974).

[4] A. D. Sakharov, "Violation of CP-invariance, C-asymmetry, and baryon asymmetry of the Universe", In The Intermissions$\cdots$ Collected Works on Research into the Essentials of Theoretical Physics in Russian Federal Nuclear Center, Arzamas-16, 84–87 (1998).

[5] P. Langacker, Grand unified theories and proton decay, Phys. Rep. **72**, 185–385 (1981).

[6] C. McGrew *et al.* (IMB Collaboration), Search for nucleon decay using the IMB-3 detector, Phys. Rev. D **59**, 052004 (1999).

[7] K. S. Hirata *et al.* (Kamiokande Collaboration), Experimental limits on nucleon lifetime for lepton + meson decay modes, Phys. Lett. B **220**, 308–316 (1989).

[8] A. Takenaka *et al.* (The Super-Kamiokande Collaboration), Search for proton decay via $p \to e + \pi^0$ and $p \to \mu + \pi^0$ with an enlarged fiducial volume in Super-Kamiokande I-IV, Phys. Rev. D **102**, 112011 (2020).

[9] K. S. Babu, Ilia Gogoladze and Cem Salih Ün, "Proton lifetime in minimal SUSY SU (5) in light of LHC results", J. High Energ. Phys. **2022**, 164 (2022).

[10] S. M. Barr, "A new symmetry breaking pattern for SO(10) and proton decay", Phys. Lett. B **112**, 219–222 (1982).

[11] K. S. Babu and S. Khan, "Minimal nonsupersymmetric SO(10) model: Gauge coupling unification, proton decay, and fermion masses", Phys. Rev. D **92**, 075018 (2015).

[12] K. S. Babu, J.C.Pati and F.Wilczek, Suggested new modes in supersymmetric proton decay, Phys. Lett. B **423**, 337–347 (1998); K. S. Babu, J. C. Pati, and F. Wilczek, Fermion masses,

neutrino oscillations, and proton decay in the light of SuperKamiokande, Nucl. Phys. B **566**, 33–91 (2000); J. C. Pati, Confronting the conventional ideas of grand unification with fermion masses, neutrino oscillations and proton decay, arXiv preprint hep-ph/0204240 (2002).

[13] K. Hamaguchi, S. Hor and N. Nagata, "R-Symmetric Flipped SU(5)", J. High Energ. Phys. **2020**, 140 (2020).

[14] K. Abe *et al.* (The Super-Kamiokande Collaboration), Search for proton decay via $p \to \nu K^+$ using 260 kiloton·year data of Super-Kamiokande, Phys. Rev. D **90**, 072005 (2014).

[15] M. Tanaka *et al.* (The Super-Kamiokande Collaboration), Search for proton decay into three charged leptons in 0.37 megaton-years exposure of the Super-Kamiokande, Phys. Rev. D **101**, 052011 (2020).

[16] K. Abe *et al.* (The Super-Kamiokande Collaboration), Search for Nucleon Decay via $n \to \bar{\nu}\pi^0$ and $p \to \bar{\nu}\pi^+$ in Super-Kamiokande, Phys. Rev. Lett. **113**, 121802 (2014).

[17] K. Abe *et al.* (The Super-Kamiokande Collaboration), Search for nucleon decay into charged antilepton plus meson in 0.316 megaton·years exposure of the Super-Kamiokande water Cherenkov detector, Phys. Rev. D **96**, 012003 (2017).

[18] V. Takhistov *et al.* (The Super-Kamiokande Collaboration), Search for Nucleon and Dinucleon Decays with an Invisible Particle and a Charged Lepton in the Final State at the Super-Kamiokande Experiment, Phys. Rev. Lett. **115**, 121803 (2015).

[19] V. Takhistov *et al.* (The Super-Kamiokande Collaboration), Search for Trilepton Nucleon Decay via $p \to e^+\nu\nu$ and $p \to \mu^+\nu\nu$ in the Super-Kamiokande Experiment, Phys. Rev. Lett. **113**, 101801 (2014).

[20] K. Kobayashi *et al.*, "Search for nucleon decay via modes favored by supersymmetric grand unification models in Super-Kamiokande-I", Phys. Rev. D **72**, 052007 (2005).

[21] R. Matsumoto *et al.*, "Search for proton decay via $p \to \mu^+ K^0$ in 0.37 megaton-years exposure of Super-Kamiokande", Phys. Rev. D **106**, 072003 (2022).

[22] R. Matsumoto and M. Ishitsuka for the Super-Kamiokande Collaboration, "Classification of Super-Kamiokande atmospheric neutrino events by using neural network", J. Phys.: Conf. Ser. **1468**, 012161 (2020).

[23] S. Fukuda, *et al.* (Super-Kamiokande Collaboration), "The Super-Kamiokande Detector", Nucl. Instr. Meth. A **501** 418–462 (2003).

[24] S. Yamada *et al.*, "Commissioning of the New Electronics and Online System for the Super-Kamiokande Experiment", IEEE Trans. Nucl. Sci. **57**, 428–432 (2010).

[25] Kamioka Observatory, ICRR, The University of Tokyo, "Super-Kamiokande", http://www-sk.icrr.u-tokyo.ac.jp/sk/

[26] Kamioka Observatory, ICRR, The University of Tokyo, "Hyper-Kamiokande", http://www-sk.icrr.u-tokyo.ac.jp/hk

[27] H. Kume *et al.*, "20 INCH DIAMETER PHOTOMULTIPLIER", Nucl. Instrum. Meth. **205** (1983) 443–449.

[28] A. Suzuki *et al.*, "Improvement of 20-inch diameter photomultiplier tubes", Nucl. Instrum. Meth. A**329** (1993) 299–313.

[29] K. Abe *et al.*, "Calibration of the Super-Kamiokande detector", Nucl. Instrum. Meth. A **737** 253–272 (2014).

[30] Y. Nakano *et al.*, Measurement of the radon concentration in purified water in the Super-Kamiokande IV detector, Nucl. Instrum. Meth. A **977**, 164297 (2020).

[31] T. Yokozawa, "Precision solar neutrino measurements with Super-Kamiokande-IV", Ph.D. thesis, University of Tokyo, (2012).

[32] M. Jiang, "Study of the neutrino mass hierarchy with the atmospheric neutrino data collected in Super-Kamiokande IV", Ph.D. thesis, Kyoto University, (2019).

[33] K. Nakamura *et al.*, "The reaction ^{12}C(e,e'p) at 700 MeV and DWIA analysis", Nucl. Phys. A **268**, 381–407 (1976).

[34] M. G. Mayer and J. H. D. Jensen, "Elementary Theory of Nuclear shell structure", Wiley, New York (1955).

[35] T. Yamazaki and Y. Akaishi, "Nuclear medium effects on invariant mass spectra of hadrons decaying in nuclei", Phys. Lett. B **453**, 1–6 (1999).

[36] C. W. de Jager, H. de Vries and C. de Vries, "Nuclear charge- and magnetization-density-distribution parameters from elastic electron scattering", Atomic Data and Nuclear Data Tables **14**, 479–508 (1974).

[37] L. L. Salcedo, E. Oset, M. J. Vicente-Vacas and C. Garcia-Recio, "Computer simulation of inclusive pion nuclear reactions" Nucl. Phys. A **484**, 557–592 (1988).

[38] J. S. Hyslop, *et al.*, "Partial-wave analysis of K^+-nucleon scattering", Phys. Rev. D **46**, 961–969 (1992).

[39] R. Weiss *et al.*, "Measurement of low energy K^+ total cross sections on $N = Z$ nuclei", Phys. Rev. C **49**, 2569–2577 (1994).

[40] R. Brun, F. Bruyant, F. Carminati, S. Giani, M. Maire, A. McPherson, G. Patrick, and L. Urban, "GEANT Detector Description and Simulation Tool", CERN Report No. CERN-W5013 (1994).

[41] Y. Hayato, "NEUT", Nucl. Phys. Proc. Suppl. **112** (2002) 171-176; Y. Hayato, L. Pickering, "The NEUT neutrino interaction simulation program library", Eur. Phys. J. Spec. Top. **230**, 4469–4481 (2021).

[42] B. R. Martin and M. K. Pidcock, "$\bar{K}N$ interactions in the resonance region (I) Analysis of data", Nuc. Phys. B **126**, 266–284 (1977); B. R. Martin and M. K. Pidcock, "$\bar{K}N$ interactions in the resonance region (II) Amplitudes", Nuc. Phys. B **126** 285–297 (1977).

[43] P. H. Eberhard and F. Uchiyama, "Neutral-kaon regeneration probabilities at asymmetric ϕ-factory energies", Nucl. Instrum. Meth. A **350**, 144–149 (1994).

[44] T. Kajita, "Atmospheric Neutrinos And Discovery Of Neutrino Oscillations", Proc. Japan Acad. B **86**, 303–321 (2010).

[45] M. Honda, T. Kajita, K. Kasahara and S. Midorikawa, "Calculation of flux of atmospheric neutrinos", Phys. Rev. D **52**, 4985–5005 (1995).

[46] M. Honda, T. Kajita, K. Kasahara and S. Midorikawa, "New calculation of the atmospheric neutrino flux in a 3-dimensional scheme", Phys. Rev. D **70**, 043008 (2004).

[47] M. Honda, T. Kajita, K. Kasahara, S. Midorikawa, and T. Sanuki, "Calculation of atmospheric neutrino flux using the interaction model calibrated with atmospheric muon data", Phys. Rev. D **75**, 043006 (2007).

[48] M. Honda, T. Kajita, K. Kasahara, and S. Midorikawa, "Improvement of low energy atmospheric neutrino flux calculation using the JAM nuclear interaction model", Phys. Rev. D **83** 123001 (2011).

[49] G. Battistoni, A. Ferrari, T. Montaruli, and P. R. Sala., "The FLUKA atmospheric neutrino flux calculation", Astropart. Phys. **19**, 269–290 (2003).

[50] G. D. Barr, T. K. Gaisser, P. Lipari, Simon Robbins, and T. Stanev. "A Three-dimensional calculation of atmospheric neutrinos", Phys. Rev. D **70**, 023006 (2004).

[51] Y. Ashie, J. Hosaka, K. Ishihara, Y. Itow, J. Kameda, Y. Koshio *et al.*, "Measurement of atmospheric neutrino oscillation parameters by Super-Kamiokande I", Phys. Rev. D **71**, 112005 (2005).

[52] C.H.Llewellyn Smith, "Neutrino reactions at accelerator energies", Phys. Rep. **3C**, 261–379 (1972).

[53] R. Gran, J. Nieves, F. Sanchez and M. J. Vincente Vacas, "Neutrino-nucleus quasi-elastic and 2p2h interactions up to 10 GeV", Phys. Rev. D **88**, 113007 (2013).

[54] B. Bourguille, and J. Nieves, and F. Sanchez, "Inclusive and exclusive neutrino-nucleus cross sections and the reconstruction of the interaction kinematics", J. High Energ. Phys. **2021**, 4 (2021).

[55] R. Gran *et al.* (K2K Collaboration), "Measurement of the quasielastic axial vector mass in neutrino interactions on oxygen", Phys. Rev. D **74**, 052002 (2006).

[56] A. A. Aguilar-Arevalo *et al.* (MiniBooNE Collaboration), "First measurement of the muon antineutrino double-differential charged-current quasielastic cross section", Phys. Rev. D **88**, 032001 (2013).

[57] P. Adamson *et al.* (MINOS Collaboration), "Study of quasielastic scattering using charged-current ν_μ-iron interactions in the MINOS near detector", Phys. Rev. D **91**, 012005 (2015).

[58] C. Berger and L. M. Sehgal, "Lepton mass effects in single pion production by neutrinos", Phys. Rev. D **76**, 113004 (2007).

[59] C. Berger and L. M. Sehgal, "Partially conserved axial vector current and coherent pion production by low energy neutrinos", Phys. Rev. D **79**, 053003 (2009).

[60] D. Rein, "Diffractive pion production in neutrino reactions", Nucl. Phys. B **278**, 61–77 (1986).

[61] M. Derrick *et al.*, "Properties of the hadronic system resulting from $\bar{\nu}_\mu p$ interactions", Phys. Rev. D **17**, 1–15 (1978).

[62] B. JongeJans *et al.*, "Multiplicity distributions of charged hadrons produced in (anti)neutrino-deuterium charged- and neutral-current interactions", Nuovo Cim. A **101**, 435–453 (1989).

[63] T. Sjostrand, "High-energy-physics event generation with PYTHIA 5.7 and JETSET 7.4", Comput. Phys. Commun. **82**, 74–89 (1994).

[64] K.Abe *et al.*, "Atmospheric neutrino oscillation analysis with external constraints in Super-Kamiokande I-IV", Phys. Rev. D **97** 072001 (2018).

[65] S. Ioffe and C. Szegedy, ”Batch Normalization: Accelerating Deep Network Training by Reducing Internal Covariate Shift”, Proc. ICML **37** 448-456 (2015).

[66] C. Ishihara, ”Full three flavor oscillation analysis of atmospheric neutrino data observed in Super-Kamiokande”, Ph.D. thesis, University of Tokyo (2010).

[67] A. Takenaka, ”Search for Proton Decay via $p \to e + \pi^0$ and $p \to \mu + \pi^0$ with an Enlarged Fiducial Mass of the Super-Kamiokande Detector”, Ph.D. thesis, University of Tokyo (2020).

[68] R. B. Patterson, E. M. Laird, Y. Liu, P. D. Meyers, I. Stancu, and H. A. Tanaka, The extended-track reconstruction for MiniBooNE, Nucl. Instrum. Meth. A **608**, 206–224 (2009).

[69] M. Jiang *et al.* (Super-Kamiokande Collaboration), Atmospheric neutrino oscillation analysis with improved event reconstruction in Super-Kamiokande IV, Prog. Theor. Exp. Phys. **2019**, 053F01 (2019).

[70] F. James, “ MINUIT - Function Minimization and Error Analysis - Reference Manual Version 94.1 ” , CERN-D-506 (1994).

[71] S. Tobayama, ”An Analysis of the Oscillation of Atmospheric Neutrinos”, Ph.D. thesis, The University of British Columbia, (2016).

[72] K. Abe *et al.*, ”Neutron Tagging following Atmospheric Neutrino Events in a Water Cherenkov Detector”, JINST **17** P10029 (2022).

[73] H. Ejiri, ”Nuclear deexcitations of nucleon holes associated with nucleon decays in nuclei”, Phys. Rev. C **48**, 1442–1444 (1993).

[74] L. L. Salcedo, E. OsetM, J. Vicente-Vacas and C. Garcia-Recio, ”Computer simulation of inclusive pion nuclear reactions”, Nucl. Phys. A **484**, 557–592 (1988).

[75] P. de Perio, ”NEUT pion FSI”, AIP Conf. Proc. **1405**, 223–228 (2011).

[76] P. de Perio, ”Joint Three-Flavour Oscillation Analysis of ν_μ Disappearance and ν_e Appearance in the T2K Neutrino Beam”, Ph. D. thesis, University of Toronto (2014).

[77] W. E. Cleland *et al.*, Measurement of the K^0_L-p and K^0_L-d total cross sections, Phys. Rev. D **12**, 1247–1259 (1975).

[78] B. P. Roe and M. B. Woodroofe, Setting confidence belts, Phys. Rev. D **63**, 013009 (2000).